INTERACTIONS BETWEEN CONVECTION AND THE BACKGROUND ATMOSPHERE
DURING HIGH RAIN EVENTS: OBSERVATIONS AND COMPARISONS WITH MODELS

by

Toni Mitovski

Submitted in partial fulfilment of the requirements
for the degree of Doctor of Philosophy

at

Dalhousie University
Halifax, Nova Scotia
April 2014

TABLE OF CONTENTS

LIST OF FIGURES

ABSTRACT

The thesis consists of three projects. Each of these projects is a diagnostic study of the interaction between strong convective events and the background atmosphere. In all projects, we use a satellite rainfall dataset to identify strong rain events. We then use radiosonde soundings to generate composite anomaly patterns of meteorological variables about the strong rain events.

In Project 1, we examine temperature, relative humidity, and divergence anomalies about strong convective events in the Western Tropical Pacific. A low-level convergence coupled to a midlevel divergence develops prior to peak rainfall. A midlevel convergence coupled to a low-level divergence develops after peak rainfall. Strong surface cold pools develop in response to high rainfall. Observations were compared to models and reanalyses. In general, models and reanalyses do not fully represent the timing, strength, and altitude of the mid-level convergence and divergence features. The surface cold anomaly is also underestimated in models. These discrepancies suggest that the mesoscale downward transport of mid-level air into the boundary layer in models may be too weak.

In Project 2, we investigate the impact of convection on the background distribution of a chemical tracer (ozone). Negative ozone anomalies and higher frequency of midlevel cloud tops occur in a layer between 3 and 8 km prior to peak rainfall. Negative ozone anomalies in the upper troposphere develop in response to high rainfall. Chemistry transport model simulations also exhibit negative ozone anomalies at upper and midlevels. However, the ozone anomalies in the model are symmetric about peak rainfall and are more persistent than observations.

In Project 3, we identify regional variations in the interaction between convection and the background atmosphere. In all four regions, deep convection imposes cooling in the lower and warming in the upper troposphere. In mid-latitudes, convection is associated with stronger anomalies in surface pressure, geopotential height, and CAPE. Over land, a low-level warm anomaly develops prior to peak rainfall and the surface cold pool that develops during peak rainfall is more persistent. The PV generated prior to peak rainfall, is advected towards the surface after peak rainfall and may play a role in hurricane genesis.

LIST OF ABBREVIATIONS AND SYMBOLS USED

Symbol	Unit	Description
A	m^2	Surface area
ACTIVE		Aerosol and Chemical Transport in Deep Convection
AGCM3		Atmospheric General Circulation Model Version3
AGCM4		Atmospheric General Circulation Model Version4
CALIPSO		Cloud-Aerosol Lidar and Infrared Pathfinder Satellite Observations
CAPE	J/kg	Convective Available Potential Energy
CCCma		Canadian Centre for Climate Modelling and Analysis
CDAAC		COSMIC Data Analysis and Archive Center
CIN	J/kg	Convective Inhibition
COSMIC		Constellation Observing System for Meteorology, Ionosphere, and Climate
ECHAM5		European Center Hamburg Model Version 5
ECMWF		European Center for Medium-Range Weather Forecast
ENSO		El Nino Southern Oscillation
ERA-40		ECMWF Reanalysis 40
ERA-Interim		ECMWF Interim Reanalysis
f	s^{-1}	Coriolis parameter
g	ms^{-2}	Standard gravity = 9.806
GCM		General Circulation Model
GEOS		Goddard Earth Observing System
GFDL CM2.1		Geophysical Fluid Dynamics Laboratory Climate Model Version 2.1
GMAO		Global Modeling and Assimilation Office
GPHT	m	Geopotential Height
GPS		Global Positioning System
IGRA		Integrated Global Radiosonde Archive
ISH		Integrated Surface Hourly
LCL	m	Lifted Condensation Level
LFC	m	Level of Free Convection
LNB	m	Level of Neutral Buoyancy
LT	h	Local Time
MCS		Mesoscale Convective System
MJO		Madden-Julian Oscillation
NCAR		National Center for Atmospheric Research
NCEP		National Centers for Atmospheric Prediction
NCDC		National Climatic Data Center
NOAA		National Oceanic and Atmospheric Administration
p		Statistical significance threshold
PV	$m^2s^{-1}Kkg^{-1}$	Potential vorticity

PVU	$m^2s^{-1}Kkg^{-1}$	Potential vorticity unit
Q	Jkg^{-1}	Heating
R_d	$Jkg^{-1}K^{-1}$	Specific gas constant of dry air = 287.04
RAS		Relaxed Arakawa-Schubert
S	$KhPa^{-1}$	Stability
SCOUT-O3		Stratospheric Climate Links with Emphasis on the Upper Troposphere and Lower Stratosphere
SHADOZ		Southern Hemisphere Additional Ozonesondes
T	K	Temperature
T_{dp}	K	Density temperature of an air parcel
T_{test}		T-test
T_{ve}	K	Virtual temperature of the environment
t	s	Time
TOGA COARE		Tropical Ocean Global Atmosphere Coupled Ocean Atmosphere Response Experiment
TRMM 3B42		Tropical Rainfall Measuring Mission Precipitation Product
u	ms^{-1}	Zonal wind component
v	ms^{-1}	Meridional wind component
UTC	h	Coordinated Universal Time
V_n	ms^{-1}	Normal wind component
V_p	ms^{-1}	Parallel wind component
WWB		Westerly Wind Burst
YOTC		Year of Tropical Convection
ZM		Zhang-McFarlane

Greek Symbols

Symbol	Unit	Description
σ		Standard deviation
σ	$KhPa^{-1}$	Static stability
ϕ	m	Geopotential height
ω	Pas^{-1}	Vertical velocity
$\nabla \cdot \dot{V}$	s^{-1}	Mass divergence
θ	K	Potential temperature
ζ	s^{-1}	Relative vorticity

ACKNOWLEDGEMENTS

CHAPTER 1. INTRODUCTION

1.1 PARCEL METHOD

In the tropics, air parcels near the surface are often conditionally unstable with respect to vertical displacement. For instance, an unsaturated air parcel lifted up from the surface by some process, will expand and cool dry adiabatically until it reaches a height at which it becomes saturated, i.e. the relative humidity of the air parcel is 100 %. This height is referred to as the Lifted Condensation Level (LCL), Figure 1.1. Once above the LCL, the air parcel will cool moist-adiabatically. The moist adiabatic lapse rate is less than the dry adiabatic lapse rate due to condensation and the latent heat released in the rising air parcel. The temperature of the rising air parcel at and below the LCL is lower than the temperature of the environment and the parcel is negatively buoyant. If the parcel is further lifted above the LCL it will eventually reach a level at which the temperature of the air parcel will equal the temperature of the ambient air. This level is referred to as the Level of Free Convection (LFC). Above the LFC the parcel will be positively buoyant until reaches a level referred to as the Level of Neutral Buoyancy (LNB). Above the LNB the air parcel becomes negatively buoyant and detrains. The LCL, LFC, and LNB can be determined from the temperature and relative humidity of the parcel at the initial level, and the temperature profile of the environment. The work required to lift an air parcel from the surface to the LFC is referred to as Convective Inhibition (CIN). The available energy between the LFC and the LNB is referred to as Convective Available Potential Energy (CAPE). For convection to start, besides CAPE, there must be some kind of a triggering mechanism, which will force the air parcel to its

1

LFC. Large-scale vertical advection and an approaching cold pool of air are some of the mechanisms that can trigger convection.

Some of the air parcels triggered near the surface will not reach the LNB. During its ascent, an air parcel will mix with the unsaturated ambient air. The unsaturated air entrained in a rising air parcel will reduce the parcel relative humidity, which will result in evaporation of some of the parcel condensate. Therefore, the mixing with the unsaturated air will reduce the parcel buoyancy and consequently will lower the theoretical parcel LNB. Air parcels detrained in the upper troposphere will force subsidence in the large-scale environment, which will warm and dry the troposphere.
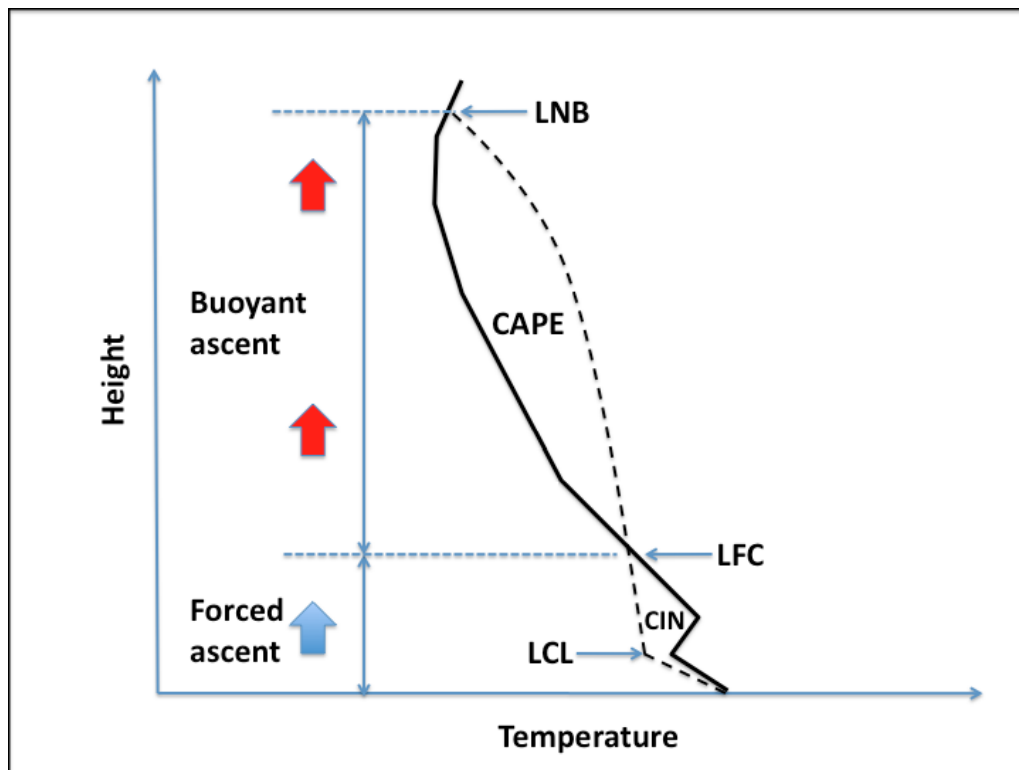
Figure 1.1: The solid black curve represents temperature measurements as function of height. The temperature of an air parcel lifted from the surface to the upper troposphere is represented with the dashed curve. Between the surface and the Level of Free Convection (LFC) the parcel is negatively buoyant with respect to the environment. Between the LFC and the Level of Neutral Buoyancy (LNB) the parcel is positively buoyant.

1.2 TROPICAL CONVECTION

Most of the rainfall in the tropics is produced by Mesoscale Convective Systems (MCS) [*Mohr et al.*, 1999]. MCSs account for 30%-70% of the April-September rainfall in the central United States [*Fritsch et al.*, 1986]. MCSs are organized convective systems that generate contiguous precipitation over an area 100 km or more in at least one direction [*Houze*, 2004]. MSCs have regions of both convective and stratiform precipitation.

Observations from field campaigns have shown that tropical convective clouds often organize themselves in a characteristic pattern called the building block model [*Mapes*, 2006]. In the building block model (Figure 1.2), convective clouds are organized in such way that congestus clouds often precede deep (cumulonimbus) convective clouds. Congestus clouds, with tops between 4.5 and 9.5 km, contribute 28% of total convective rainfall in the Western Tropical Pacific [*Johnson et al.*, 1999]. More important is that congestus clouds pre-moisten the lower and middle troposphere, which has been shown to promote further vertical growth of convective clouds [*Warner et al.*, 1980; *Sherwood*, 1999; *Sobel at al.*, 2004; *DeMott el al.*, 2007]. According to the building block model, low-level convergence, mid-level divergence, and vertical tilt, upward to the right, in positive specific humidity anomalies develop prior to peak rainfall. These features suggest preferred population of cumulus congestus clouds. A middle-level convergence low-level divergence, and positive humidity anomalies in the upper troposphere develop after peak rainfall and were associated with stratiform anvil clouds.

Congestus and deep convective clouds contribute 60% of the total tropical precipitation [*Schumacher and Houze*, 2003]. Convective precipitation is intense and

concentrated over small areas whereas stratiform precipitation has lower intensity but is spread over larger areas. Deep convection warms the troposphere, thus acts to stabilize the environment. In addition, deep convection transports large amount of condensate into the upper troposphere where it detrains. This condensate contributes to the development of stratiform anvil clouds with cloud base usually at about 5 km [*Zipser*, 1977].
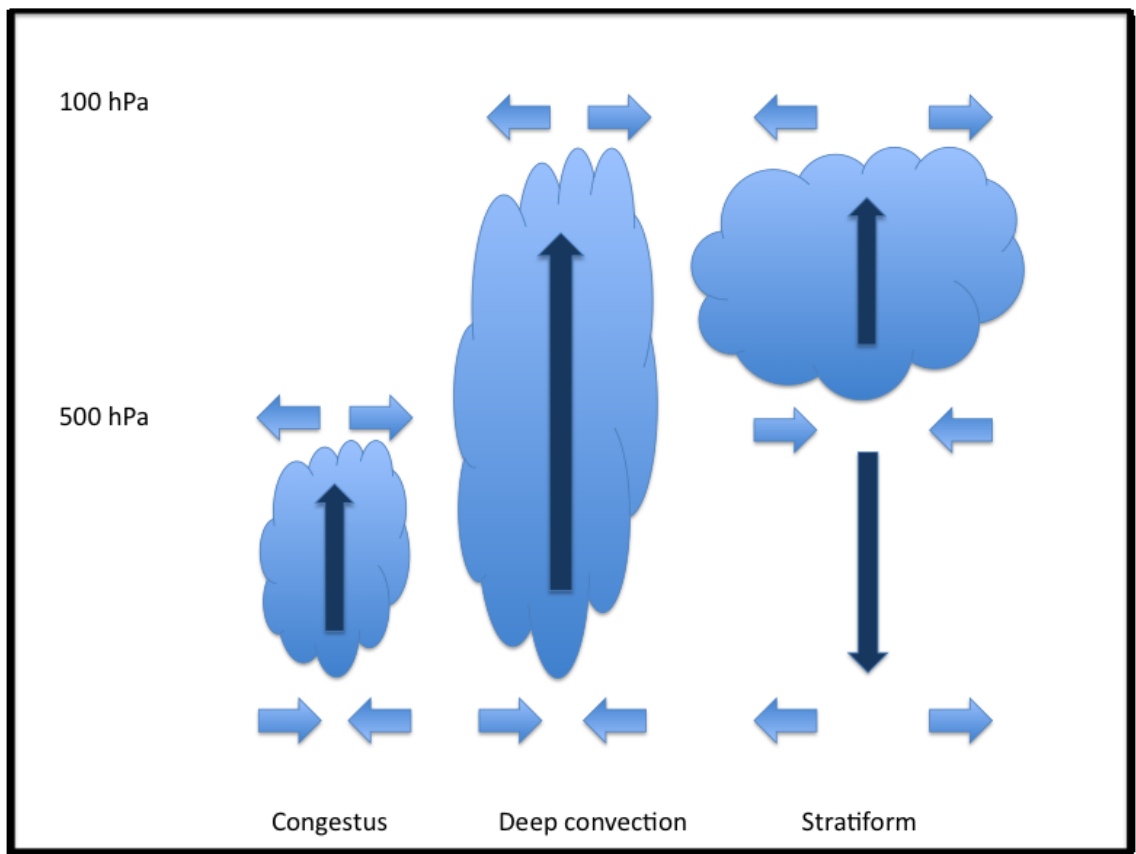
Figure 1.2: In the building block conceptual model congestus clouds are followed by deep cumulonimbus clouds, which are then followed by precipitating stratiform anvil clouds. The horizontal (vertical) arrows show horizontal (vertical) advection.

Although less intense than convective precipitation, stratiform precipitation accounts for about 40% of the total rainfall in the tropics [*Schumacher and Houze*, 2003]. Some fraction of the stratiform precipitation evaporates as it falls through the unsaturated

air below the cloud base. The evaporation cools the ambient air and generates negatively buoyant mesoscale downdrafts. The negatively buoyant downdrafts are stronger in a drier environment and can often penetrate to the surface [*Zipser*, 1969; 1977], where they can spread laterally as a cold pool of air and generate gust fronts. The downdrafts force large-scale upward motion in the background atmosphere. This forced upward motion will moisten and cool the lower troposphere, thus increase the low-level instability. In addition, the cold pool of air that propagates outward from the stratiform region, may also force uplift and trigger new convection in the vicinity of the storm. The temperature profile of stratiform regions is dominated by warm temperature anomalies in the upper troposphere and cold temperature anomalies in the lower troposphere.

1.3   MID-LATITUDE CONTINENTAL CONVECTION

Over the tropical ocean, convective rainfall generally peaks in the early morning. Over the mid-latitude land convective rainfall shows stronger diurnal variation with minimum in the midmorning and maximum in the late afternoon hours [*Nesbitt and Zipser*, 2003]. A diurnal cycle in convective rainfall will imply a diurnal cycle in cloud amount [*May et al*., 2012] and humidity, and thus may induce a diurnal variation in the radiation budget at the surface. Convection over land is also associated with frequent lightning, hail, and tornadoes, which together with heavy rainfall may cause substantial material damage in urban areas or extensive crop damage in rural areas.

The main difference between the tropical and midlatitude regions is that towards the higher latitudes the Coriolis force increases and the Rossby radius of deformation decreases. The Rossby radius of deformation represents the horizontal scale at which the

balance between the Coriolis force and the horizontal pressure gradient becomes important. At the equator, the Rossby radius of deformation tends to infinity and a pressure gradient will force a motion with direction straight down towards the low-pressure anomaly. In midlatitudes, on the other hand, the Rossby radius of deformation is about 2000 km [*Houry et al.*, 1987] and a pressure gradient will force a motion, which will be deflected by the Coriolis force. For instance, a convective system will perturb the background atmosphere and these perturbations will be confined within a distance equal to the Rossby radius of deformation for particular latitude.

Another difference between the regions is that the lower and middle troposphere over the mid-latitude land is drier than the troposphere over the tropical ocean. A drier lower troposphere may affect convection in two ways. A rising air plume may experience stronger evaporation in drier troposphere, reduced buoyancy, and may detrain at lower altitudes. The moisture content of the lower troposphere may control the evaporation rate in the rising plumes and affect the pre-moistening and transition time from shallow to deep convection. Also in a drier lower troposphere, precipitation from mid-latitude convective clouds may experience stronger evaporation than tropical precipitation. Stronger evaporation means stronger cooling, which may have an influence on the strength of downdrafts. Another difference between convection over ocean and convection over land is that, soil moisture and evapotranspiration from vegetation regulate the amount of latent and sensible heat flux and thus may control convection over land.

There are some similarities in the effect of convection on the background atmosphere in the midlatitudes and the tropics. Although over land most of the

precipitation is produced in deep convective clouds [*Schumacher and Houze*, 2003], convection over midlatitude land also generates stratiform temperature response in the environment, i.e. warm temperature anomalies in the upper troposphere and cold temperature anomalies in the lower troposphere.

1.4 GLOBAL CLIMATE MODELS

The horizontal resolution of a global climate model is much larger than the spatial scale of an individual convective cloud. Therefore, climate models employ convective schemes to parameterize the effect of convection on the temperature and water vapor budget of the background atmosphere as a function of grid-scale variables. Convective parameterizations of climate models are adjusted to produce realistic climatological distribution of rainfall and temperature in the tropics.

1.4.1 ZHANG-MCFARLANE SCHEME

The latest version of the Canadian climate model employs the mass flux scheme of Zhang and McFarlane (ZM) to parameterize the effect of convection on the large-scale environment [*Zhang and McFarlane*, 1995; *McFarlane et al*., 2005]. The ZM convective scheme is based on the plume ensemble theory developed in 1970s [*Arakawa and Schubert*, 1974]. Convection in the ZM scheme is activated when the lower troposphere is locally conditionally unstable, i.e. CAPE is above some threshold value. Once activated, convective plumes, which are assumed to have same initial mass flux, detrain in the stable portion of the troposphere, typically above 500 hPa. The stability is defined as a positive vertical gradient of the moist static energy. The moist static energy of an air

parcel is a combination of a parcels internal energy, gravitational potential energy, and latent energy. The ZM scheme assumes that a balance exists between CAPE production by the large-scale processes and CAPE consumption by convection. In the ZM scheme, convective plumes remove column instability over some prescribed time.

1.5   SIMPLE DYNAMICAL MODEL

In the thesis, we generate and examine composite anomaly patterns associated with high rainfall events. The temperature and divergence anomaly patterns shown in the thesis are similar with the temperature and divergence anomaly patterns generated by a simple dynamical model. In this model, the temperature and wind perturbations associated with 2-day westward propagating equatorial waves can be reproduced as a combination of convective and dynamical forcings [*Haertel and Kiladis,* 2004].

Two-day waves are part of a broad spectrum of convectively coupled equatorial waves [*Matsuno*, 1966]. These waves have zonal wavelengths of 2000-4000 km and propagation speed of 10 - 30 ms^{-1} [*Takayabu*, 1994; *Takayabu et al.*, 1996; *Haertel and Johnson*, 1998]. During the Tropical Ocean Global Atmosphere Coupled Ocean Atmosphere Response Experiment (TOGA COARE) campaign (November 1992 to February 1993), most of the rainfall variability was dominated by westward propagating 2-day waves.

The model of Haertel and Kiladis solves the inviscid (frictionless) primitive equations on a β-plane linearized about a basic state of rest to describe the dynamical evolution within 2-day disturbances. The horizontal momentum equations are,

$$\frac{\partial u}{\partial t} - \beta y v + \frac{\partial \phi}{\partial x} = 0 \qquad (1.1)$$

8

$$\frac{\partial v}{\partial t} + \beta y u + \frac{\partial \phi}{\partial y} = 0$$

(1.2)

where u is perturbation zonal velocity, v is perturbation meridional velocity, t is the time, x and y represent the zonal and the meridional displacement, β is the meridional change of the Coriolis parameter, and ϕ is perturbation geopotential.

Assuming the atmosphere is in hydrostatic balance (no vertical acceleration) the hydrostatic equation is,

$$\frac{\partial \phi}{\partial p} = -\frac{RT}{p}$$

(1.3)

where p stands for pressure, T is perturbation temperature, and R is the gas constant for dry air.

Assuming no horizontal temperature advection, which is a good approximation over the tropical ocean, the thermodynamic energy equation is,

$$\frac{\partial T}{\partial t} - S\omega = Q$$

(1.4)

where S represents stability (change of potential temperature with height), ω is perturbation vertical velocity (omega), and Q is perturbation heating (condensational heating or evaporative cooling).

The continuity equation is,

$$\frac{\partial u}{\partial x} + \frac{\partial v}{\partial y} + \frac{\partial \omega}{\partial p} = 0$$

(1.5)

The thermodynamic energy equation (1.4) states that the temperature tendency ($\partial T/\partial t$) is a sum of convective heating (Q) and adiabatic temperature change due to the dynamical response to convective heating ($S\omega$). Therefore, if the heating in equation 1.4

9

is given, the system of five equations can be used to determine the five remaining unknowns.

The authors (Haertel and Kiladis) used radiosonde data from the TOGA COARE campaign, surface data from buoys, and measurements of infrared satellite brightness temperature to first isolate oscillations with periods of about 2 days, and then construct time-pressure composites of temperature, divergence, and Q.

The heating Q was then used to run the model. The Q is,

$$Q(x,y,p,t) = Q_v(p)Q_t(t)Q_h(x,y)Q_w(x,t) \qquad (1.6)$$

Where Q_v denotes the vertical structure. The amplitude and phase of Q_v come directly from the observed composite heating analysis. Q_t represents the temporal structure and is defined to be a half sine wave (from 0 to π). Q_t mimics the temporal dependence of the composite wave's heating (Q). Q_h represents the horizontal structure. It is Gaussian in both x and y, with maximum at x=0, y=0. The Gaussian is consistent with the observed brightness temperature analysis. Q_w represents the propagating wave velocity. The velocity is -16 m/s (westward propagation) and is consistent with the observed brightness temperature analysis.

The simulated time-pressure composites of temperature and zonal wind capture most of the structure that appears in the composite temperature and zonal wind analyses [*Haertel and Kiladis*, 2004].

The heating Q(x,y,p,t) can be further simplified. Haertel and Kiladis assumed that Q could be expressed using just 2 vertical modes. The first mode is associated with deep convective heating throughout the troposphere peaking at mid levels. The second mode is associated with convective heating (cooling) in the lower troposphere and convective

10

cooling (heating) in the upper troposphere prior (after) peak rainfall. Figure 1.3 shows the temperature and divergence perturbations associated with the two mode heating function.

In Figure 1.3, the ovals represent convective heating (red) or cooling (blue). The vertical arrows represent adiabatic cooling due to ascent and adiabatic warming due to descent. The dark gray horizontal arrows represent the wind field. Again, the simulated time-pressure composites of temperature and zonal wind show similarity with the observed composites of temperature and zonal wind [*Haertel and Kiladis, 2004*].
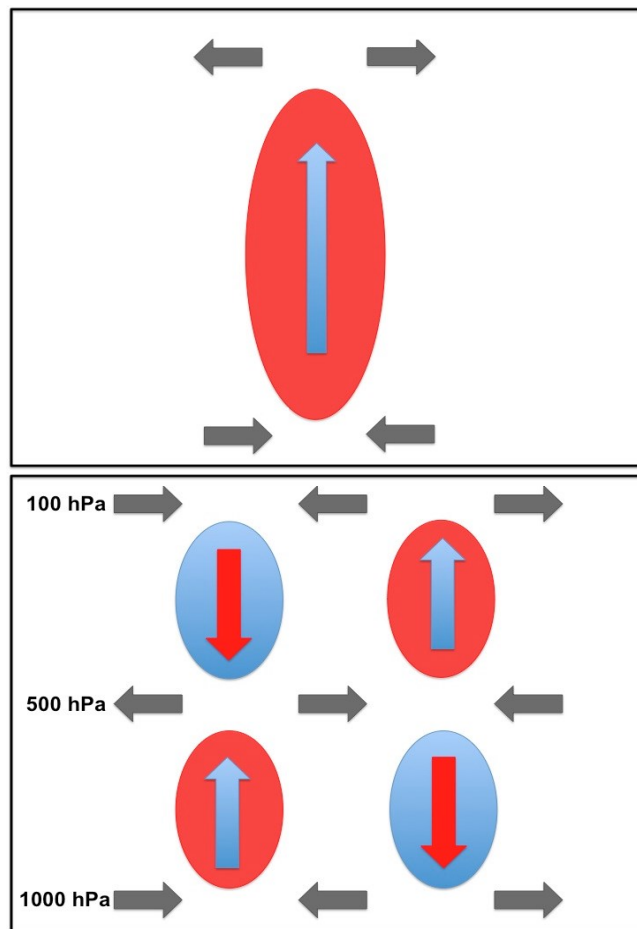
Figure 1.3: Two-mode conceptual model. Mode 1 (upper panel) is associated with convective heating (red) and dynamical cooling (blue) that extend throughout the troposphere. Mode 2 (lower panel) is associated with convective heating and dynamical cooling in the lower (upper) troposphere and convective cooling and dynamical heating in the upper (lower) troposphere prior (after) to peak rainfall.

1.6 GOALS OF THE PRESENT WORK

Convection is an important process due to its impact on the water and energy budgets and due to the control of aerosol and greenhouse gas concentrations in the upper troposphere. By cooling the lower and warming the upper troposphere, convection acts to destabilize the lower and stabilize the upper troposphere. Global climate models use convective parameterizations to simulate the effect of convection on the background atmosphere. Models are useful tools for investigating the future evolution of climate. However, these models have some limitations. Models have weakness in the simulation of the diurnal cycle in convective rainfall over land [*Dai*, 2006]. The weakness can be attributed to methods used in convective parameterization to calculate the cloud base mass flux [*Folkins et al., 2013* submitted to JGR]. Although there was a great progress in the study of the Madden-Julian Oscillation (MJO) during the past years, models still have difficulties accurately simulating rainfall variability associated with the MJO [*Lin et al.*, 2006]. Models also have difficulty simulating rainfall variability associated with monsoons [*Rajeevan and Nanjundiah*, 2009] and extreme rain events [*Wilcox and Donner*, 2007]. This is because the small-scale processes driving monsoons and extreme rain events are not resolved in the models. Models also tend to produce light precipitation (<10 mm day^{-1}) more often than observed [*Dai*, 2006]. Since the short-time scale rainfall variability in models is unrealistic, the short-time scale temperature and water vapor budgets in models are unrealistic as well. Unrealistic representation of convection-environment interaction is a major source of uncertainty in providing confident predictions of future climate [*Randall et al.*, 2003; *Arakawa*, 2004].

The latent heat released in mesoscale convective systems is the main energy source that drives large-scale circulations including the Hadley circulation. It is therefore very important to understand the lifecycle of a mesoscale convective system as well as the short-time scale interaction between convection and the large-scale background atmosphere. Studies using measurements from field campaigns [*Houze*, 1977; *Zipser and Gautier*, 1978; *Frank*, 1978; *Murakami*, 1979; *Warner et al.*, 1980; *Sobel et al.*, 2004, *Mapes et al.*, 2006, *DeMott et al.*, 2007, *Mapes et al.*, 2009], satellite data [*Masunaga*, 2012], re-analysis data [*Benedict and Randall*, 2007; *Rapp et al.*, 2011], and routine radiosonde profiles [*Sherwood and Wahrlich*, 1999; *Mitovski et al.*, 2010] have examined the short-time scale interaction between tropical convection and the large-scale environment. Most of these studies were based on short-term campaigns or were case studies.

In this thesis, data from satellites, radiosondes, and ozonesondes are used to investigate the interaction between deep convection and the background atmosphere on short-time scales. The results are then compared to several climate models and reanalysis products. These comparisons are intended to test how well convection is represented in climate models. We also show that a simple dynamical model [*Haertel and Kiladis, 2004*], originally developed to explain the anomaly patterns of the 2-day wave, is an appropriate conceptual model for interpreting the mean anomaly patterns of high rain events over the tropical oceans. The results in the thesis provide observational targets for future development of convective parameterizations in climate models.

CHAPTER 2. TEMPERATURE, RELATIVE HUMIDITY, AND DIVERGENCE RESPONSE TO HIGH RAINFALL EVENTS IN THE TROPICS: OBSERVATIONS AND MODELS

Authors: Toni Mitovski[1], Ian Folkins[1], Knut von Salzen[2], and Michael Sigmond[3].

[1] Department of Physics and Atmospheric Science, Dalhousie University, Halifax, Canada

[2] Canadian Centre for Climate Modelling and Analysis, University of Victoria, Victoria, Canada

[3] Department of Physics, University of Toronto, Toronto, Canada

2.1 ABSTRACT

Radiosonde measurements and TRMM 3B42 rainfall are used to construct composite anomaly patterns of temperature, relative humidity, and divergence about high rainfall events in the western Pacific. The observed anomaly patterns are compared with anomaly patterns from four general circulation models (AGCM3, AGCM4, GFDL CM2.1, and ECHAM5) and two reanalysis products (ERA-40 and ERA-Interim). In general, the models and reanalyses do not fully represent the timing, strength, or altitude of the mid-level congestus divergence that precedes peak rainfall, or the mid-level stratiform convergence that occurs after peak rainfall. The surface cold pools that develop in response to high rainfall events are also either not present, or somewhat weaker than observations. When stratiform precipitation falls through unsaturated air below the melting level, it can generate negatively buoyant downdrafts, which may penetrate to the surface and spread-out as cold pool of air. Differences between the modeled and observed response to high rainfall events suggest that the convective parameterizations used by the

models and reanalyses discussed here may under-represent the strength of the mesoscale downdraft circulation.

2.2 INTRODUCTION

The convective parameterizations of climate models are typically adjusted to give reasonable climatological distributions of temperature, water vapor, convective mass transport, and rainfall in the tropics. However, these climatological distributions arise from the cumulative impact of individual moist convective events that occur on much shorter timescales. Realistic convective parameterizations should be able to simulate the short timescale interactions between moist convection and the background atmosphere.

Observations from field campaigns and satellites over the past forty years, as well as simulations from cloud resolving models, have shown that tropical convective clouds often organize themselves in a characteristic manner that has recently been dubbed the "building block" pattern [*Mapes et al*., 2006]. Congestus clouds often precede deep convection, and give rise to a mid-level divergence prior to deep convective rainfall [Th*ompson et al*., 1979; *Mapes and Lin*, 2005; *Mapes et al*., 2006]. Cumulus congestus development is aided and partially controlled by a mid-level cooling that both precedes and follows maximum rainfall [*Sherwood and Wahrlich*, 1999; *Mapes et al*., 2006; *DeMott et al*., 2007; *Mapes et al*., 2009]. Mid-level moistening from cumulus congestus clouds appears to promote the subsequent development of deep convection [*Johnson et al*., 1999; *Sherwood*, 1999; *Sobel et al*., 2004; *DeMott et al*., 2007].

Deep convective clouds inject large amounts of condensate into the upper troposphere. This condensate contributes to the development of precipitating stratiform

anvil clouds that can persist for several hours or more following deep convection. It has been estimated that 40% of tropical rainfall originates from stratiform clouds [*Schumacher and Houze*, 2003]. The base of precipitating stratiform anvil clouds is usually near the 0ºC melting level, or about 5 km [*Zipser*, 1977]. When stratiform precipitation falls through unsaturated air below the melting level, it can generate negatively buoyant mesoscale downdrafts that penetrate to the surface [*Zipser*, 1969; 1977; *Barnes and Garstang*, 1982]. Precipitating stratiform anvil clouds are typically convergent at mid-levels [*Reed and Recker*, 1971; *Mapes and Houze*, 1995; *Mapes and Lin* 2005]. This convergence is probably at least partially attributable to a rapid increase in downdraft mass flux near the melting level [*Johnson*, 1976; *Folkins* 2009].

By mass continuity, the downdrafts associated with stratiform precipitation must induce compensatory uplift in their environment. On shorter spatial scales, this uplift is mediated by density currents and pressure gradient accelerations that can generate squall lines [*Tepper*, 1950]. On larger spatial scales, this uplift is generated by waves. The cooling and moistening of the background atmosphere associated with this wave induced compensatory uplift can also trigger further downstream convection [*Mapes*, 1993; *Mapes and Houze*, 1995; *Fovell et al.*, 2006].

Many of the previous studies examining the short timescale interactions between tropical convection and the background atmosphere have generated composite analyses using output from cloud resolving models, data from field programs of several months in duration, ERA-40 reanalysis [*Benedict and Randall*, 2007], or NCEP–NCAR reanalysis [*Maloney and Hartmann*, 1998]. Here, we develop composite anomaly patterns from 11 years of radiosonde data (1998 – 2008) at 10 locations in the western tropical Pacific.

High rainfall events at these radiosonde locations were identified using the 3-hour gridded rainfall product 3B42 from the Tropical Rainfall Measuring Mission (TRMM) [*Kummerow et al.*, 1998]. The radiosonde measurements were used to construct temperature, relative humidity, and mass divergence anomaly patterns about TRMM high rainfall events. These anomaly patterns extend from 24 hours prior to peak rainfall to 24 hours after peak rainfall.

In the building block model, the interactions between the three basic cloud building blocks – cumulus congestus, deep, and stratiform – promote the organization of tropical moist convection into coherent propagating systems across a wide range of spatiotemporal scales. Parameterizations of tropical convection that exhibit these types of interactions should be better able to reproduce the observed spatial and temporal variability of deep convection. We therefore examine the interaction of high rainfall events with the background atmosphere in four climate models, and in two reanalysis data sets.

The paper is divided into five sections. In Section 2, we discuss the radiosonde dataset, the TRMM 3B42 gridded rainfall product, the general circulation models, and the reanalysis products used in the study. In section 3, we discuss the methods used to construct the observed anomaly patterns. These patterns are discussed in Section 4. In Section 5, we discuss the construction of anomaly patterns in the models, and compare the anomaly patterns from the models with observations. Section 6 is a summary of our results.

2.3 DATASETS

2.3.1 IGRA

The Integrated Global Radiosonde Archive (IGRA) is produced by the National Climatic Data Center (NCDC). This radiosonde archive is derived from eleven different sources, and contains records from more than 1500 stations [*Durre et al*., 2006]. Most of the stations have twice daily records for the past 20 years. We used temperature, relative humidity, and wind data for 11 years (1998 – 2008) on standard pressure levels (1000, 925, 850, 700, 500, 400, 300, 250, 200, 150, 100 hPa). The locations of the radiosonde stations used in this study are shown in Figure 2.1.
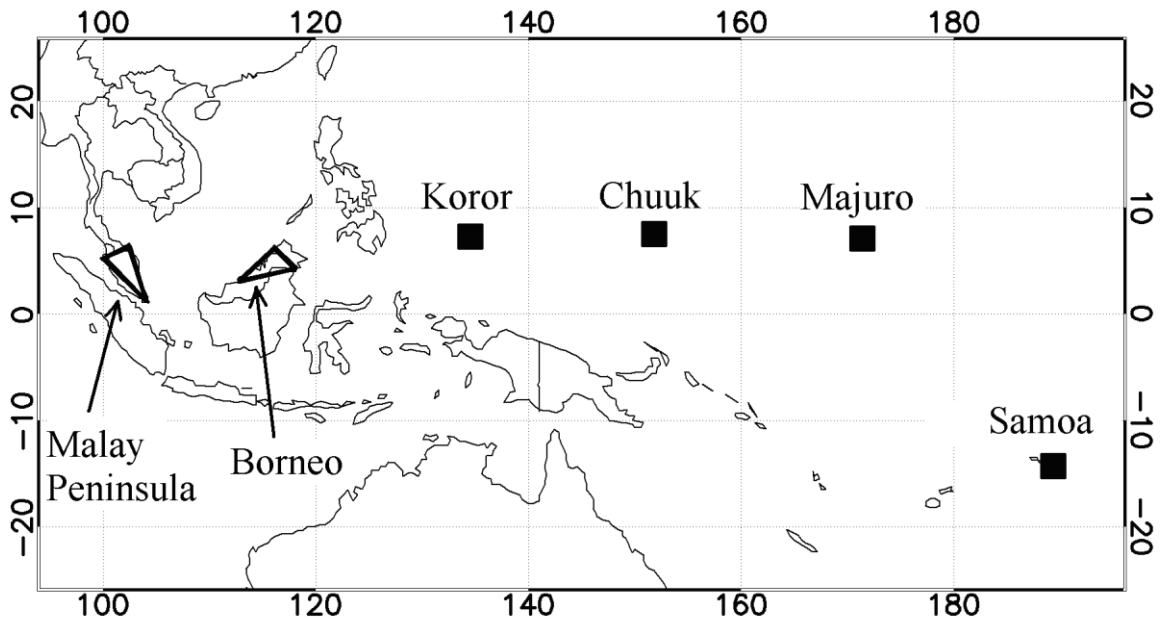
Figure 2.1: Solid squares indicate the locations of the radiosonde stations used to calculate temperature and relative humidity anomaly patterns at remote marine locations. The two triangular radiosonde arrays were used mainly to calculate mass divergence patterns about high rainfall events. The array on the Malay Peninsula consisted of stations Singapore (Changi), Kota Bharu, and Penang (Bayan Lepas). The array on the island of Borneo consisted of Tawau, Bintulu, and Kota Kinabalu.

The stations at Koror, Chuuk, Majuro, and Samoa were used to construct temperature and relative humidity anomaly patterns that should be representative of the western tropical Pacific Ocean. Figure 2.1 also shows a triangular radiosonde array on the island of Borneo, and another on the Malay Peninsula. These arrays were used to construct divergence anomaly patterns about high rainfall events. The wind measurements from these triangles can be expected to be strongly influenced by the diurnal cycle in moist convection over land, and by local sea breeze circulations.

2.3.2 TRMM

The TRMM 3B42 gridded rainfall product has a temporal resolution of 3 hours centered at the standard synoptic times (00, 03, 06, 09, 12, 15, 18, and 21 UTC), and a spatial resolution of 0.25º. We used data from 1998 to 2008. The TRMM data come from several satellite-borne sensors including a precipitation radar, multi-channel microwave radiometer, and visible and infrared sensors [*Kummerow et al.*, 1998]. The TRMM 3B42 algorithm uses a combination of high-quality microwave and IR precipitation estimates to derive calibration coefficients and adjust the IR estimates from other satellite observations. The high-quality estimates are used where available. The remaining grid boxes are filled with the adjusted IR estimates [*Huffman et al.*, 2007]. The TRMM 3B42 rainfall estimates are then scaled to match monthly measurements from rain gauges.

2.3.3 AGCM3

The Third Generation Atmospheric General Circulation Model (AGCM3) is maintained by the Canadian Centre for Climate Modelling and Analysis (CCCma). The

model output is archived on a 2.8º x 2.8º grid every 3 hours. The results in this paper are based on 10 years of AGCM3 output. Deep convection is parameterized using the Zhang and McFarlane (ZM) mass flux scheme [*Zhang and McFarlane*, 1995, *McFarlane et al.*, 2005]. The ZM scheme represents deep convection using plumes with various entrainment rates. In AGCM3, as well as in the other models discussed here, the temperature, humidity, and wind (or divergence) fields refer to model variables at one timestep, while precipitation is accumulated over a 3 hour period (or for some models, a 6 hour period).

2.3.4   AGCM4

AGCM4 is a revised version of AGCM3. The output was stored at a spatial resolution of 2.8º x 2.8º every 6 hours. AGCM4 has a new radiation code, prognostic cloud microphysics, and a shallow cumulus scheme [*von Salzen et al.*, 2005]. It continues to use the ZM scheme for deep convection. This study uses 5 years of AGCM4 output.

2.3.5   GFDL CM2.1

The Geophysical Fluid Dynamics Laboratory Climate Model Version 2.1 (GFDL CM2.1) is a coupled ocean-atmosphere model. The output was stored at a resolution of 2.0º latitude x 2.5º longitude, every 6 hours. The model uses the Relaxed Arakawa Schubert (RAS) parameterization for deep convection [*Delworth et al.*, 2006]. This study used 5 years of data (1996-2000) from a 20th century climate run.

2.3.6 ECHAM5

The output from the European Center Hamburg Model Version 5 (ECHAM5) [*Roeckner et al.*, 2003] was stored at a resolution of 1.9º x 1.9º, every 6 hours. ECHAM5 employs a mass flux scheme for shallow, mid-level, and deep convection [*Tiedtke*, 1989], with modifications for penetrative convection [*Nordeng*, 1994]. The stratiform scheme consists of prognostic equations representing liquid water and ice, a cloud microphysical scheme [*Lohmann and Roeckner*, 1996], and a statistical cloud cover scheme [*Tompkins*, 2002]. We used 5 years of data (2001-2006) from a 2001-2050 scenario run.

2.3.7 ECMWF ERA-40 AND ERA-INTERIM

In addition to output from four general circulation models, we also examined the ERA-40 and ERA-Interim reanalysis products from the European Center for Medium-Range Weather Forecast (ECMWF) [*Uppala et al.*, 2005]. ERA-40 output is archived at a resolution of 2.5º x 2.5º, every 6 hours. ERA-Interim output has a slightly finer spatial resolution of 1.5º x 1.5º, but is also stored every 6 hours. We used five years of data from both ERA-40 (1997-2001) and ERA-Interim (2003-2007). The instantaneous temperature, relative humidity, and wind fields are stored at the standard synoptic times of 00, 06, 12, and 18 UTC. A cumulative precipitation forecast is issued at 00 UTC for the 00 – 06 UTC six hour time interval. This was used to obtain an average rain rate at 03 UTC. A second precipitation forecast is issued at 00 UTC for the 00 – 12 UTC twelve hour time interval. This was used to obtain a forecast average rain rate at 09 UTC (after first subtracting the first 00 – 06 UTC cumulative precipitation forecast). Cumulative 6

hour rain rate forecasts centered at 15 UTC and 21 UTC, based on precipitation forecasts at 12 UTC, were obtained in a similar manner.

2.4 PROCEDURE FOR CALCULATING OBSERVED ANOMALY PATTERNS

2.4.1 TEMPERATURE ANOMALY PATTERNS

Composite temperature anomaly patterns about high rainfall events were constructed for the four remote island radiosonde stations indicated in Figure 2.1 by solid squares. TRMM 3B42 rainfall was first averaged over a 2º by 2º region centered at each island. This was done to facilitate comparisons with the anomaly patterns of the models. High rainfall events were defined as events at which the 3 hour TRMM rainfall rate within each 2º by 2º region centered at a radiosonde location was in the highest one percent for that month, averaged over the 11 years of the TRMM record. After determining the times of these high rainfall events, we searched for radiosonde profiles, at each location, that had occurred 24 hours before, or 24 hours after, one of these events. A time difference was assigned to each radiosonde profile based on the difference between the launch time of each radiosonde, and the time of the TRMM rainfall event. We then calculated the anomaly of the radiosonde temperature profile with respect to an 11-year climatology. This climatology was constructed from all radiosonde profiles at that location which had occurred during the same month, and also had the same launch time, as the radiosonde profile close to a high rainfall event. This was done to remove the influence of the seasonal and diurnal cycles on the temperature anomalies. The various radiosonde temperature anomaly profiles were then grouped together in 3 hours time

bins, ranging over the 48 hour time interval, and then combined to create a composite anomaly pattern as a function of pressure and time.

Despite their differing geographic locations, the temperature anomaly patterns of the four remote island stations were quite similar. The four patterns were therefore averaged together to create an overall anomaly pattern. This is shown in Figure 2.2(a). There were roughly 1300 high rainfall events over the 11 year period from all four locations. Within the 48 hour time window about these 1300 events, there were approximately 4000 temperature available soundings.

One would expect temperature anomaly patterns about high rainfall events to be sensitive to the intensity threshold used to define the events, and to the size of the area over which events are spatially averaged. Figure 2.2(b) shows the temperature anomaly pattern generated by retaining the original 0.25º resolution of the TRMM 3B42 dataset, but again using the top 1% events with a 0.25º x 0.25º box. This pattern is very similar to the pattern obtained by degrading the original resolution to 2.0º. Figure 2.2(c) shows the temperature anomaly pattern generated using the highest 5 percent TRMM 3B42 rainfall events, but again using the 2.0º resolution. The relaxation of the event definition decreases the magnitude of the temperature anomalies by roughly one third. However the shape of the overall pattern is similar to the pattern obtained by using the higher rainfall event threshold. The near invariance of the temperature anomaly pattern with respect to changes in event definition, with respect to both spatial size and intensity, supports previous arguments that the building block pattern recurs within organized tropical convection across a broad range of spatiotemporal scales [*Mapes et al.*, 2006].
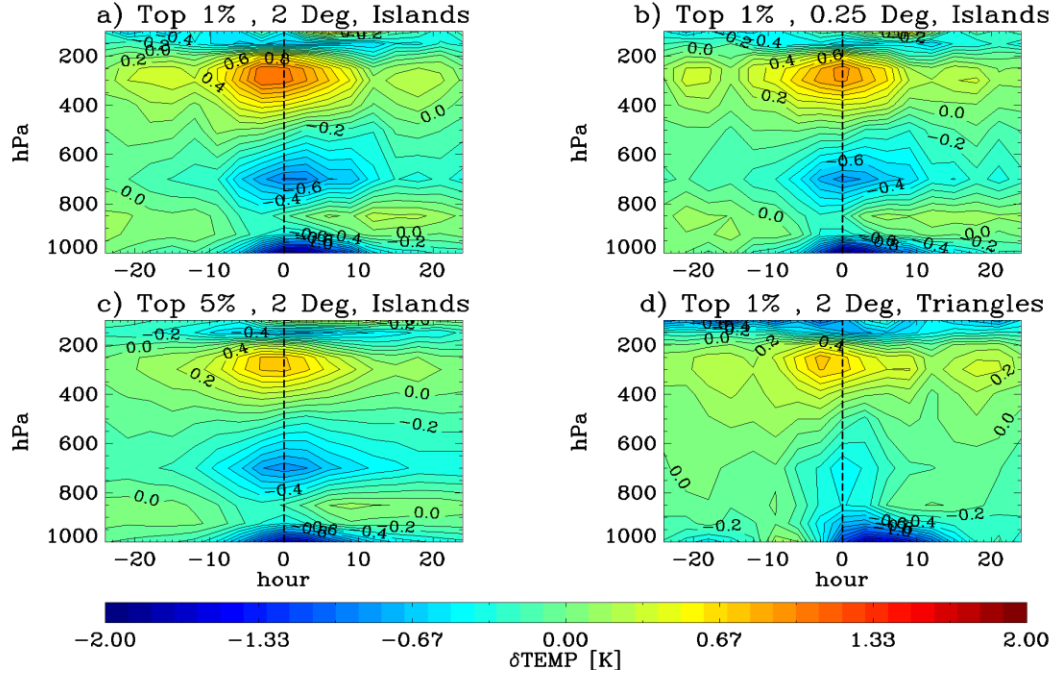
Figure 2.2: Time-height plots of the observed temperature anomaly pattern about high rainfall events (t = 0 on the horizontal axis). Values at negative lags refer to temperature anomalies prior to peak rainfall. Values at positive lags refer to temperature anomalies after peak rainfall. The anomalies were calculated using radiosonde temperature soundings and 3-hour TRMM 3B42 rainfall. Figures (a), (b), and (c) are anomaly patterns averaged over the four remote radiosonde locations shown in Figure 2.1, but with differing rain event thresholds and averaging regions: (a) the top 1 percent of 2 x 2 degree rain events (centered at the radiosonde locations), (b) the top 1 percent of 0.25 x 0.25 degree rain events, and (c) the top 5 percent of 2 x 2 degree rain events. Figure (d) shows the temperature anomalies calculated using the soundings from the six land stations (vertices of the triangles shown in Figure 2.1).

Moist convection over land differs from moist convection over the ocean. For consistency with the temperature and relative humidity anomaly patterns, and to facilitate comparisons with the models, it would have been desirable to also calculate the divergence anomaly pattern using horizontal wind measurements from remote ocean stations. However, a sufficiently close set of routine measurements from tropical islands was not available. We instead used the two triangular radiosonde arrays shown in Figure

24

2.1. There is no guarantee that the divergence patterns from these land stations will resemble those over the ocean.

Figure 2.2(d) shows the temperature anomaly patterns of the top 1% rainfall events at the arrays, defined using 2º x 2º boxes centered at the two arrays. The shapes of the temperature anomaly patterns of the two arrays are similar to the anomaly patterns of the remote oceanic islands. However, the temperature response of the two arrays is about 50% weaker than over the islands. This difference probably arises from the smaller spatial scale of the rainfall events over the arrays. For every top 1 percent 2º x 2º rainfall event over the arrays, the average 6º x 6º rainfall rate centered on the array is 0.28 times the 2º x 2º rainfall rate. For each top 1 percent 2º x 2º rainfall event over the remote ocean islands, the average 6º x 6º rainfall rate centered on the island is 0.37 times the 2º x 2º rainfall rate.

2.4.2 RELATIVE HUMIDITY ANOMALY PATTERN

Relative humidity anomaly patterns about high rainfall events were constructed using the same procedure used for the temperature anomaly patterns. Figure 2.3(a) shows an average relative humidity anomaly pattern for the four remote island radiosonde locations. Radiosonde humidity measurements tend to be less accurate at the cold temperatures of the upper troposphere. Relative humidity anomalies are therefore not shown above 250 hPa. Figure 2.3(b) shows a relative humidity anomaly pattern calculated in the same manner as for 2.3(a), but with the size of the rainfall area decreased from 2º to 0.25º. Figure 2.3(c) shows a relative humidity anomaly pattern in which the rainfall event intensity threshold is relaxed from 1 % to 5 %. As with the

25

temperature anomaly pattern, the shape of the relative humidity anomaly pattern is nearly

insensitive to changes in rainfall event definition.

Figure 2.3(d) shows the relative humidity anomaly of the two arrays is weaker than

that over the remote ocean islands. This is also likely due to the shorter spatial scale of

the rain events over the two arrays. However, the shape of the relative anomaly patterns

of the two arrays is again very similar to the anomaly patterns over the oceanic islands.
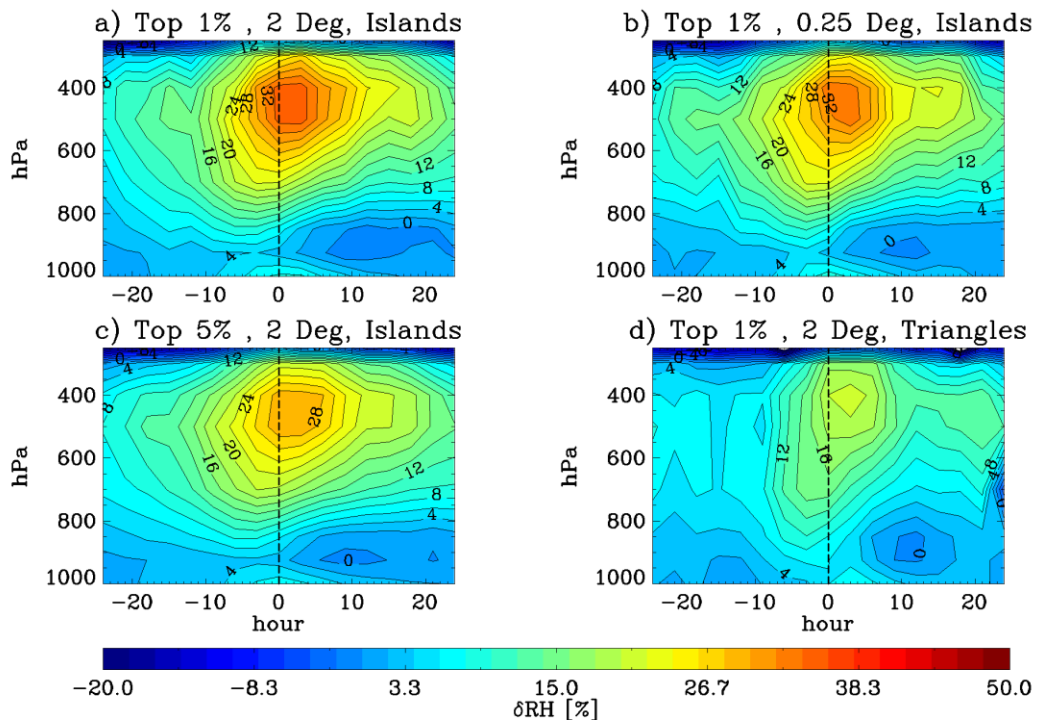
Figure 2.3: Time-height plots of observed relative humidity anomaly patterns about high rainfall events (t = 0). Figures (a), (b), and (c) are averages using data from the four remote tropical islands shown in Figure 2.1. Figure (d) is based on radiosonde profiles from the two triangular radiosonde arrays shown in Figure 2.1.

In general, changes in relative humidity are due to some combination of changes in

temperature and specific humidity. It can be shown, however, that the observed specific

humidity anomaly pattern is similar to the observed relative humidity anomaly pattern, so

that the relative humidity anomalies shown in Figure 2.3 are mainly due to changes in specific humidity.

2.4.3 DIVERGENCE ANOMALY PATTERN

The two radiosonde arrays used here to calculate the divergence patterns are shown in Figure 2.1. The area of each array is approximately 65,000 km^2, comparable with the area of a GCM grid box. The calculation of the divergence of an array, at any pressure level, requires simultaneous knowledge of the winds at each of the three radiosonde locations. Due to missing wind measurements from one or more stations, complete divergence profiles were not available at all radiosonde launch times. We therefore defined high rainfall events as those that were in the top five percent of monthly TRMM 3B42 rainfall, averaged over each array. Figure 2.4 shows the divergence anomaly pattern of the two arrays, as well as the divergence pattern itself. Other than averaging over a different spatial area, the divergence and divergence anomaly patterns were calculated using a procedure identical to that used for the temperature and relative humidity anomaly patterns.

The dominant error in the calculation of the divergence at any level is probably the error associated with the interpolation of the horizontal winds at any two vertices of an array to the midpoint of the line connecting them. This error is difficult to quantify. However, the high rainfall event divergence patterns of the two arrays are similar, so that the divergence features shown in Figure 2.4 are likely to be characteristic of the two arrays.
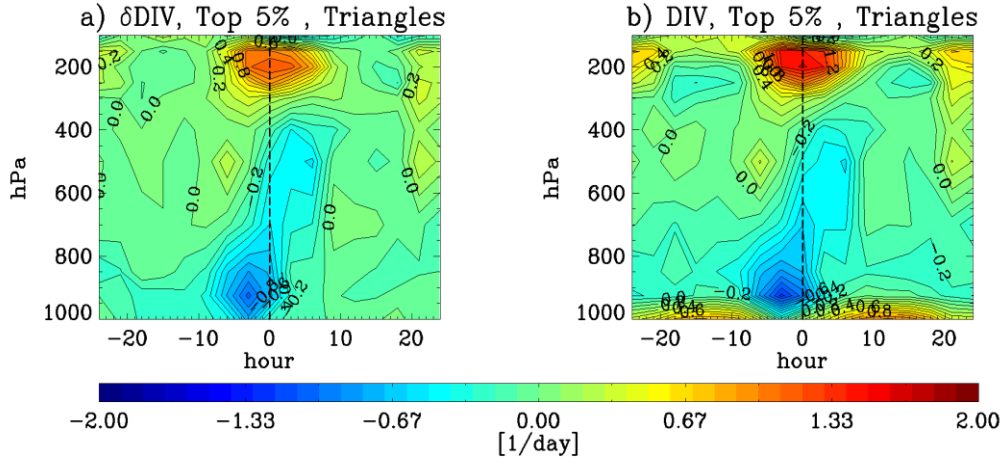
Figure 2.4: Time-height plots of the observed anomaly divergence and divergence patterns about high rainfall events (t = 0). Figures (a) and (b) were calculated using the top 5% rainfall events averaged over the two radiosonde arrays shown in Figure 2.1.

The statistical representativeness of the divergence patterns is not as high as for the temperature and relative humidity anomaly patterns. The number of divergence measurements for each array within each time bin is 300 – 350 per level in the lower troposphere, but decreasing to 70 – 80 per level in the upper troposphere.

2.5 DISCUSSION OF OBSERVED ANOMALY PATTERNS

2.5.1 DISCUSSION OF THE OBSERVED TEMPERATURE ANOMALY PATTERN

The solid black curve in Figure 2.5(g) shows the variation in TRMM 3B42 rainfall with time, averaged over the roughly 1300 high rainfall events at the four radiosonde locations. Rainfall during high rainfall events (i.e. zero time lag) exceeds 5 mm/hour, corresponding to a roughly twenty-fold increase from the climatological rain rate at these locations.

Figure 2.5(a) shows that the dominant features in the observed temperature response to high rainfall events are an upper level warming of roughly 1 K, a 0.8 K mid-

28

level cooling centered at 500 hPa, and a boundary layer cooling below 900 hPa of up to 2 K. All three features are nearly symmetric about zero lag, and extend from roughly 10 hours prior to peak rainfall, until 10 hours after peak rainfall. There is a tendency for the mid-level and boundary layer cooling to be preferentially distributed toward positive lag times. This is particularly true in the case of the boundary layer cooling of the two radiosonde arrays, shown in Figure 2.2(d).

Temperature soundings taken after the passage of convective squall lines, and under precipitating anvil clouds, often show a cool near saturated layer of air in the lowest few hundred meters. This layer is separated by an inversion from an overlying layer of warm dry air, between roughly 950 hPa and 850 hPa [*Zipser*, 1977]. In Figures 2.2 and 2.3, the warm dry layer that gives rise to these characteristic "onion" shaped soundings occurs between 950 hPa and 800 hPa, and is strongest 10 to 20 hours after peak rainfall.

Tropical convection produces a long-range temperature response in the background atmosphere. The lower tropospheric cooling has a spatial scale of roughly 1000 km, while the upper tropospheric warming has a spatial scale of 2000 km [*Folkins et al.*, 2008]. It is therefore likely that temperature anomalies prior to the rainfall maxima partially reflect the remote impact of the propagation of convective systems toward the radiosonde location, rather than simply the effects of local convection. Similarly, temperature anomalies at positive time lags will also reflect the remote effects of convective systems outside the 2º by 2º-averaging region.
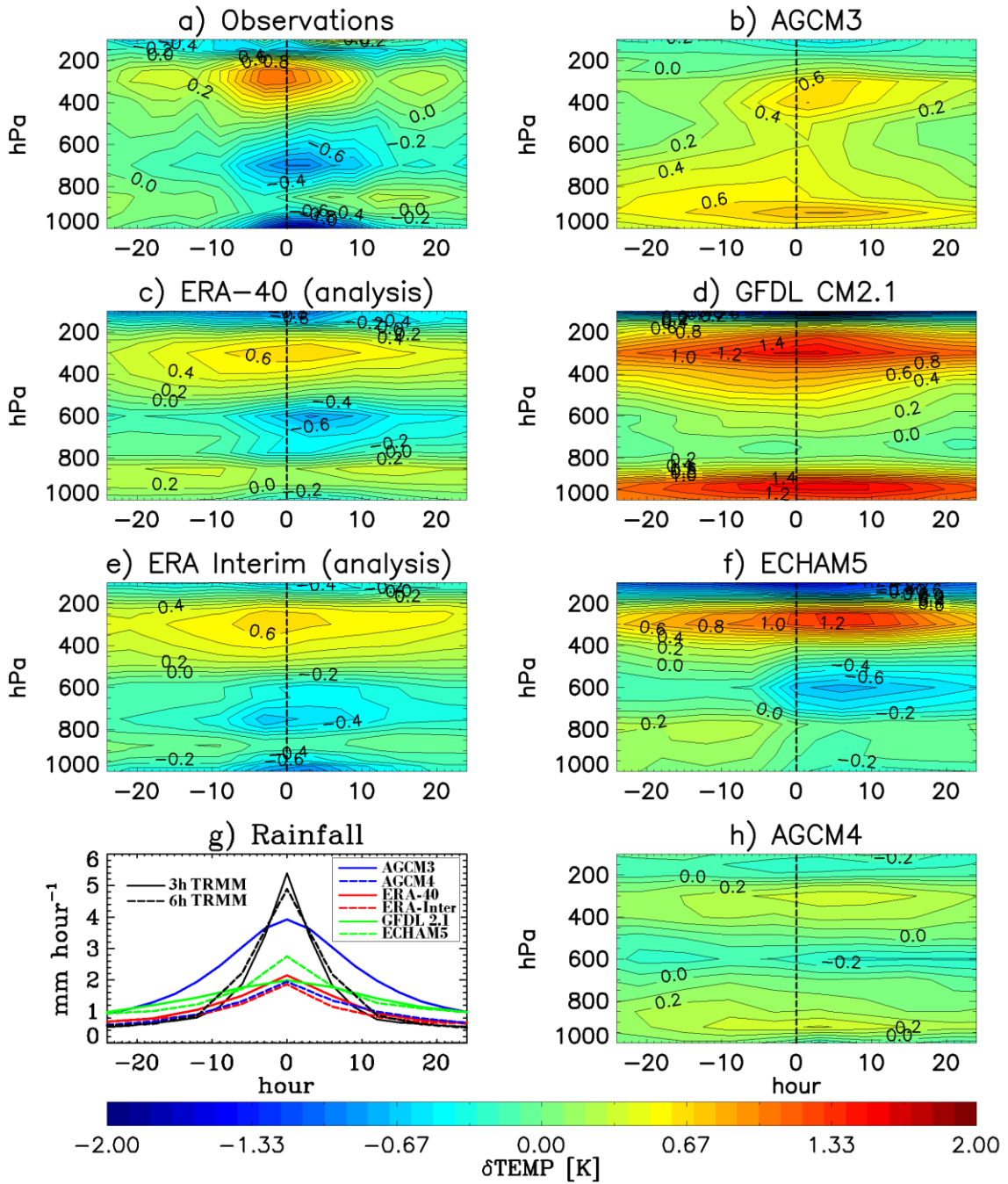
Figure 2.5: The observed temperature anomaly pattern in (a) is compared with the temperature anomaly pattern calculated from (b) CGCM3, (c) ERA-40, (d) GFDL CM2.1, (e) ERA-Interim, (f) ECHAM5, and (h) AGCM4. Figure (g) shows variation in rainfall with time before and after the top one percent rainfall events.

2.5.2 DISCUSSION OF THE OBSERVED RELATIVE HUMIDITY ANOMALY PATTERN

Figure 2.6(a) shows the observed relative humidity anomaly pattern associated with the top 1% high rainfall events at the four island stations. Deep convection gives raise to positive relative humidity anomalies at all altitudes except within the boundary layer. There is a broad upper level relative humidity maximum centered several hours after peak rainfall. Between 900 hPa and 700 hPa, relative humidity peaks approximately 4-5 hours prior to peak rainfall. Contours of constant relative humidity then tilt upward to the right for the next 20 hours. The slope in mid-level relative humidity prior to deep convection has been previously interpreted as a consequence of the development and growth of congestus clouds prior to deep convection [*Takayabu et al.*, 1996; *Mapes et al.*, 2006].
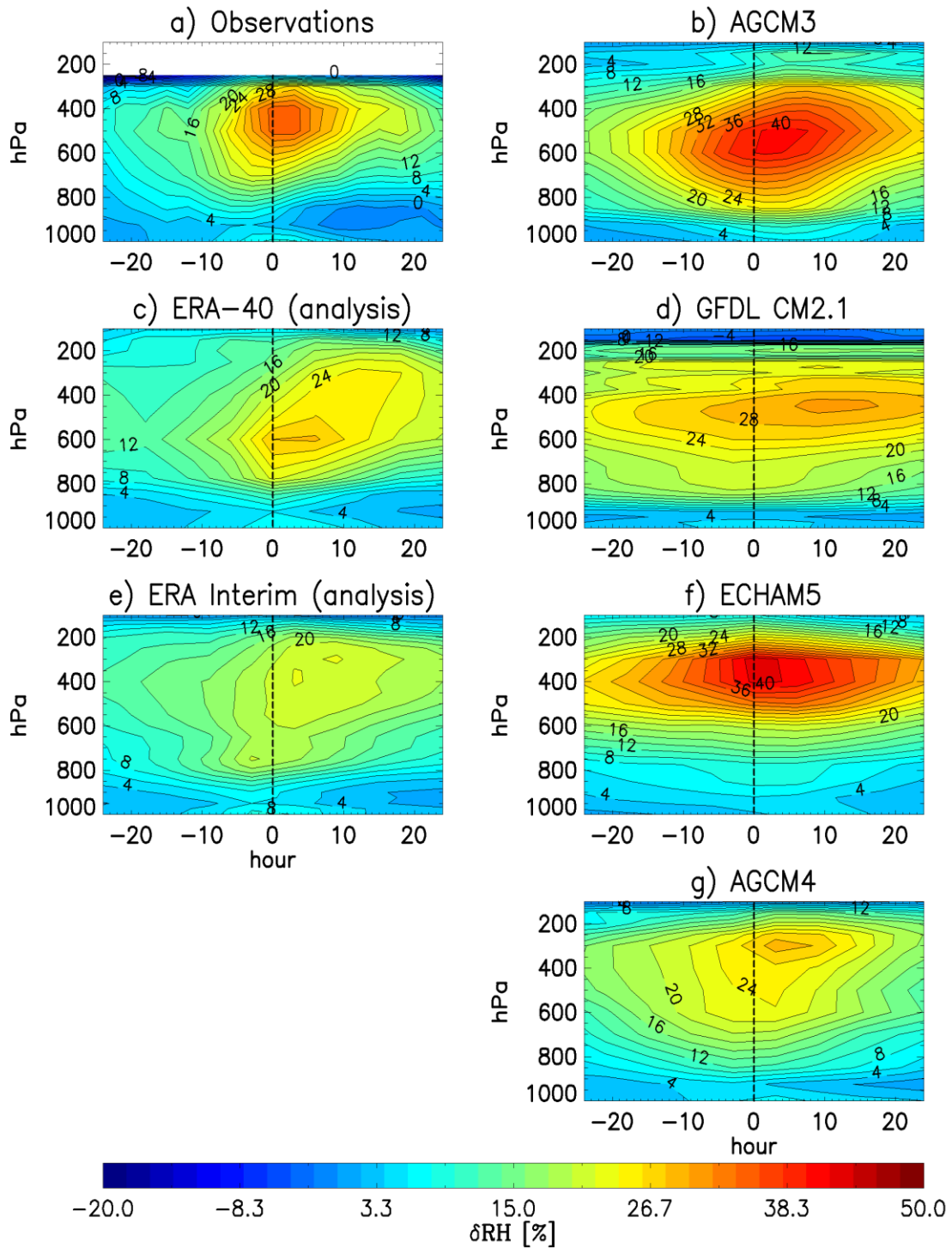
Figure 2.6: The observed relative humidity anomaly pattern in (a) is compared with the relative humidity anomaly patterns from (b) CGCM3, (c) ERA-40, (d) GFDL CM2.1, (e) ERA-Interim, (f) ECHAM5, and (g) AGCM4 model output.

2.5.3 DISCUSSION OF THE OBSERVED DIVERGENCE ANOMALY PATTERN

Figure 2.7(g) shows the variation of observed rainfall with time during rainfall events within the two radiosonde arrays on Borneo and the Malay Peninsula. Peak rainfall during these events is roughly 2.5 mm/hour, about half the intensity of the rainfall events over the tropical islands. This is mainly a reflection of the use of a 5 % rather than 1 % event threshold. There is also a pronounced diurnal cycle, reflecting the stronger diurnal cycle in tropical deep convection over land.

Figure 2.7(a) shows the divergence anomaly pattern associated with high rainfall events. Boundary layer convergence starts to intensify 10 hours prior to maximum rainfall. The onset of this low-level convergence is coincident with the emergence of a mid-level divergence feature centered at 500 hPa [*Schumacher et al.*, 2008]. The height and timing of this feature suggest that it arises from cumulus congestus outflow. These clouds are probably responsible for the observed mid-level relative humidity maximum prior to peak rainfall.

The vertical growth of congestus clouds is believed to be strongly affected by the stability of the atmosphere. Figure 2.2 shows that a mid-level cold anomaly develops prior to maximum rainfall. This cold anomaly would increase the atmospheric stability near 500 hPa, and contribute to the development of what is known as melting level inversions [*Johnson et al.*, 1996]. The existence of these stability layers favors detrainment from cumulus congestus clouds near 500 hPa [*Zuidema*, 1998; *Johnson et al.*, 1999; *Folkins*, 2009].
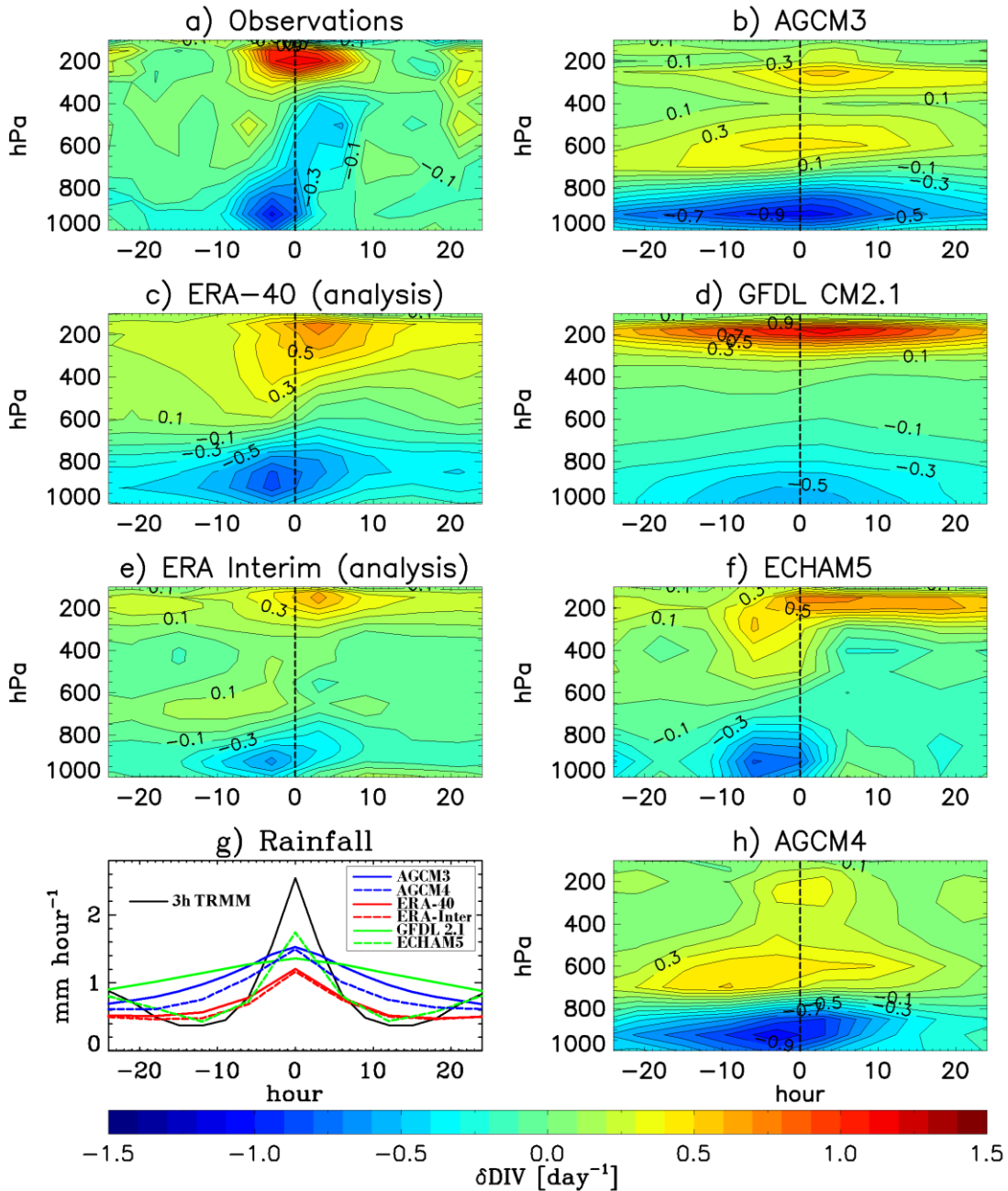
Figure 2.7: Time-height plots of the mass divergence anomaly about a maximum precipitation reference time. The observed divergence shown in (a) was calculated from soundings of the horizontal wind at the two triangular arrays shown in Figure 2.1, using the top 5 % rainfall events within these arrays as determined from TRMM 3B42 rainfall. The remaining divergence patterns are taken from climate models or reanalyses: (b) AGCM3, (c) ERA-40, (d) GFDL CM2.1, (e) ERA-Interim, (f) ECHAM5 (h) AGCM4. Figure (g) shows the variation in TRMM 3B42, modeled, and analyses rainfall, averaged over all top five percent events.

Deep convective outflow gives rise to a pronounced maximum in upper level divergence between 300 hPa and 150 hPa, centered at peak rainfall. The temporal and vertical separation between the congestus and deep outflow divergence maxima suggests that they originate from distinct cloud types with different convective heating profiles. The 500 hPa mid-level convergence maximum, which occurs after peak rainfall, is probably due to some combination of an increase in downdraft mass flux at the melting level, and an increase in upward mass flux within stratiform anvils [*Houze*, 2004]. The congestus divergence and stratiform convergence are of similar magnitude and occur at similar heights.

2.6 MODELED ANOMALY PATTERNS

Rainfall events were identified in the models and reanalyses using the same procedure as described for the TRMM 3B42 rainfall events, except that the native horizontal resolution of the models was retained in each case. The grid cells selected from each model were those nearest the radiosonde locations, or arrays. Figure 2.5(g) shows the average variation of rainfall with time during the modeled rainfall events over the remote marine radiosonde stations. In all models, the rainfall events are less intense than in TRMM 3B42.

The weakness of the modeled rainfall events is partly due to the longer temporal resolution of the model output. For all models except AGCM3, the rainfall events have been defined using accumulated rainfall output at 6 hours rather than 3 hours. For comparison, we also show the variation of rainfall with time if the TRMM rainfall events are defined using a version of the TRMM 3B42 dataset in which the temporal resolution

is degraded from 3 hours to 6 hours. The 6-hour TRMM rainfall event profile, as represented by the dashed black curve in Figure 2.5(g), is slightly less intense and less temporally confined than the 3-hour TRMM. However, the TRMM 6-hour rainfall event profile continues to be more sharply peaked than the models.

In some cases, the weaker rainfall event intensity of the models may also be partly due to the fact that their spatial resolution is slightly larger than the 2º by 2º spatial resolution used to define the TRMM rainfall events. It is well known, however, that global models tend to exhibit less rainfall variance than observations [*Scinocca and McFarlane*, 2004; *DeMott et al.*, 2007]. Models produce light precipitation (<10 mm/day) more often than observed, and underestimate strong precipitation (>10 mm/day) [*Sun et al.*, 2005; *Dai* 2006].

Despite the differences in rainfall event intensity, the observed invariance of the temperature and relative humidity anomaly patterns with respect to changes in event definition suggests that, in principle, models should be able to reproduce the basic aspects of the building block pattern, despite their reduced rainfall variance.

Figure 2.5 shows that each of the four general circulation models generates an upper tropospheric warming associated with high rainfall events, albeit with varying degrees of realism. In general, the upper tropospheric warming in the models is less temporally confined than in observations.

None of the climate models exhibits the strong boundary layer cooling coincident with maximum rainfall seen in the observations. The GFDL CM2.1 and AGCM3 models show a boundary layer warming. This discrepancy is probably a reflection of the absence,

from these models, of downdrafts originating at mid-levels capable of injecting air with low moist static energy into the boundary layer [*Barnes and Garstang*, 1982].

Although there is a narrow layer of mid-level cooling in the AGCM4 model, the only climate model showing a pronounced mid-level cooling is ECHAM5. This cooling occurs, however, mostly after peak rainfall. The observed mid-level cooling is almost symmetric about peak rainfall.

As would be expected, the temperature anomaly patterns of the two reanalyses are closer to observations. The greater dispersion of the upper tropospheric warming in the two reanalyses can probably be attributed to the greater width of the rainfall event maxima in these two models. Despite the input of surface observations, the ERA-40 temperature anomaly pattern does not exhibit surface cold pools in association with deep convection. There is some boundary layer cooling in ERA-Interim, but it is somewhat weaker than observed. Both reanalyses show a pronounced mid-level cooling. The absence, or weakness, of the surface cold pools in the models and reanalyses is unfortunate. The downdrafts associated with surface cold pools have been associated with the mesoscale organization of tropical convection [*Tompkins*, 2001] and the emergence of the congestus outflow mode [*Folkins*, 2009; *Khairoutdinov et al.*, 2009].

The right hand panels of Figure 2.6 show the change in relative humidity of the four climate models in response to high rainfall events. All four models show extensive upper level moistening. This moistening tends to be less confined both temporally, and in the vertical, than the observed moistening. The observed low level pre-moistening and tilt occurs to some degree in the AGCM4 climate model, and in the analyses, but is less evident in the other three climate models.

The right hand panels of Figure 2.7 show the divergence anomaly pattern of the four climate models. As would be expected, all models show a strong boundary layer convergence, and upper level divergence, in association with high rainfall events. Most models and analyses show at least some suggestion of a distinct congestus outflow mode. In general, however, the timing, strength, and height of the congestus outflow mode are not realistically represented.

ECHAM5 is the only climate model to show a post-convective mid-level stratiform convergence. It is, however, somewhat weaker and higher than the observed convergence. The two reanalyses do not fully represent the observed mid-level congestus divergence – stratiform convergence dipole. ERA-Interim does show a mid-level divergence dipole. But the dipole is weaker than observed, and there is a vertical misalignment between the divergence prior to maximum rainfall, and the convergence after maximum rainfall.

As with the temperature and relative humidity anomaly patterns, some of the differences between the observed and modeled divergence patterns are probably a result of differences in rainfall variance. The solid black line in Figure 2.7(g) shows the averaged variation in TRMM 3B42 rainfall with time during the top 5 % rainfall events inside the two radiosonde arrays shown in Figure 2.1. The other curves show the top 5 % rainfall events in the four models and two reanalyses. As was the case with the top 1 % rainfall events, the observed rainfall events are more sharply peaked than the models.

2.7 SUMMARY

We have used radiosonde measurements and TRMM 3B42 rainfall estimates to confirm and extend the building block model of tropical convection. High rainfall rates are coincident with three distinct temperature anomalies: upper level warming, mid-level cooling, and boundary layer cooling. Congestus clouds moisten the mid-troposphere prior to peak rainfall. This contributes to an upward tilt in relative humidity contours as rainfall proceeds. A mid-level congestus divergence – stratiform convergence dipole is symmetrically distributed about peak rainfall. After peak rainfall, a warm dry layer develops near 850 hPa. The temperature and relative humidity anomaly patterns of high rainfall events are insensitive to how high rainfall events are defined, at least in terms of their intensity and spatial extent. This supports previous arguments that the building block conceptual picture of moist convection is applicable across a broad range of spatio-temporal scales [*Mapes et al.*, 2006].

The observed divergence anomaly pattern was generated using two radiosonde arrays over land. There is no guarantee that this divergence pattern will also be representative of the tropical oceans. However, the similarity between the temperature and relative humidity anomaly patterns of the land arrays to those of the remote ocean islands suggests that the divergence patterns should also be similar.

We compared the observed anomaly patterns with those generated by high rainfall events in four climate models, and in two reanalysis datasets. Some aspects of the short timescale interactions between high rainfall events and the background atmosphere are not fully resolved in models. In particular, the mid-level congestus divergence – stratiform convergence dipole is not well represented in either the models or the

reanalyses. The ECHAM5 model and ERA-Interim analysis do successfully exhibit a mid-level divergence dipole. However, the timing, strength, and altitude of these dipoles are not fully consistent with observations.

Most of the models and reanalyses do not exhibit the strong surface cold pools that occur in association with high rainfall events. The ERA-Interim reanalysis, and to a lesser extent the ERA-40 reanalysis and the ECHAM5 model, do successfully exhibit some surface cooling in association with high rainfall events. In general, however, these differences suggest that, in both models and reanalyses, the transport of mid-tropospheric air with low moist static energy into the boundary layer via mesoscale downdrafts may be too weak.

In the tropics, rainfall heats and moistens the background atmosphere in such a way as to promote the propagation of coherent moving rainfall patterns. Models which are able to realistically simulate the short timescale impact of high rainfall events on the background atmosphere should also be more likely to simulate observed rainfall variability. Deep convection affects the water vapor budget through vapor and condensation detrainment, precipitation evaporation, downdraft detrainment, induced subsidence from updrafts, and induced uplift from downdrafts. In a general circulation model, it is difficult to determine whether the relative contribution of each of these processes to the water vapor budget as a function of altitude is realistic. However, if the water vapor budget of a model is realistic, the effect of convection on the background humidity field on short timescales should be well simulated. The types of local diagnostic tests discussed here may be useful in guiding the development of more predictive

convective parameterizations, both in terms of their rainfall forecasts on short timescales, and their climate forecasts on longer timescales.

2.8 ACKNOWLEDGEMENTS

CHAPTER 3. TESTING CONVECTIVE TRANSPORT ON SHORT TIME SCALES: COMPARISONS WITH MASS DIVERGENCE AND OZONE ANOMALY PATTERNS ABOUT HIGH RAIN EVENTS

Authors: Toni Mitovski[1], Ian Folkins[1], Randall V. Martin[1,2], and Matthew Cooper[1]

[1]Department of Physics and Atmospheric Science, Dalhousie University, Halifax, Canada

[2]Harvard-Smithsonian Center for Astrophysics, Cambridge, USA

3.1 ABSTRACT

High rain events in the western tropical Pacific were identified using the TRMM 3B42 gridded rainfall dataset. Horizontal wind measurements from radiosonde arrays, cloud top frequency measurements from CALIPSO, and ozonesonde measurements from SHADOZ, were used to construct anomaly patterns of divergence, cloud top frequency, and ozone mixing ratio about the high rain events. The observed divergence anomaly pattern was compared with patterns produced by the GEOS-4 and GEOS-5 assimilated meteorological datasets. The mid-level (~ 6 km) divergence dipole seen in observations – consisting of a local maximum in divergence 8 hours before peak rainfall and a local maximum in convergence 8 hours after peak rainfall – is not represented in the GEOS-4 or GEOS-5 meteorology. The ozone anomaly pattern shows ozone decreases at mid-levels (3 – 8 km) up to 16 hours prior to peak rainfall. These decreases occur in association with increases in the frequency of mid-level cloud tops and are due to increased detrainment from cumulus congestus clouds. The observed ozone anomaly pattern was compared with anomaly patterns produced by the GEOS-Chem chemical transport model, driven by GEOS-4 and GEOS-5 assimilated winds and temperatures.

The GEOS-Chem simulations also exhibit negative ozone anomalies at mid-levels in association with high rain events. However, these anomalies are nearly symmetric about peak rainfall, rather than strongest prior to peak rainfall. The upper level negative ozone anomalies of the models are more persistent than the observations. These results help characterize some of the difficulties of meteorological datasets in capturing the layered character of tropical convective outflow, and its timing with respect to high rain events.

3.2 INTRODUCTION

Short-lived species can be transported within convective clouds from the boundary layer to the free troposphere and affect the local rates of ozone and aerosol production. The accuracy of convective transport in global models is often tested using monthly or seasonal distributions of relative humidity and other chemical tracers [*Bey et al., 2001, Folkins et al., 2006*]. However, it is possible in principle for a model to generate realistic distributions of chemical tracers on monthly timescales, even if the short timescale convective events, which give rise to this distribution, are not accurately represented.

Assessing the accuracy of convective transport in a global model is a challenge. It is difficult to directly compare in situ measurements of chemical tracers from aircraft with models because models rarely simulate the details of a particular convective event with sufficient accuracy to make point-by-point comparisons meaningful. However, tropical convection often exhibits a repetitive sequence of vertical motions – the so-called building block pattern [*Mapes et al.*, 2006] – in which mid-level congestus clouds are followed by deep cumulonimbus clouds, which are then followed by precipitating stratiform anvil clouds. The existence of this pattern suggests that it may be useful to

construct anomaly patterns of chemical tracers in the time-height plane about high rain events using a long time series of observed profiles above a fixed location, and compare the results with models. The main practical difficulty with this approach is that it requires at least several hundred vertical profiles of a chemical tracer to develop statistically robust anomaly patterns.

Here, we use a 12 year record of ozone sondes (1998 – 2009) at Fiji and Samoa from the Southern Hemisphere Additional Ozonesondes (SHADOZ) campaign [*Thompson et al.*, 2003] to construct ozone anomaly patterns about high rain events. The rain events at Fiji and Samoa were identified using the TRMM (Tropical Rainfall Measuring Mission) 3B42 gridded rainfall product [*Kummerow et al.*, 1998]. The growth and decay of the rain events we selected typically occurred over a 10 – 20 hour period. When constructing the ozone anomaly patterns, we therefore looked for ozonesondes that occurred within 24 hours of a rain event.

The imprint produced by a convective cloud on the background distribution of a chemical tracer will be strongly influenced by how the cloud mixes with its environment, and in particular, its vertical profiles of convective entrainment and detrainment. Within an area containing a group of convective clouds, the sum of mass entrainment and detrainment is approximately equal to the mass divergence. Divergence anomaly patterns about high rain events are therefore useful for interpreting tracer anomaly patterns. Calculations of mass divergence require at least a triangular array of horizontal wind measurements. Due to the absence of nearby radiosonde stations, it was not possible to calculate mass divergence profiles at Fiji or Samoa. Mass divergence anomaly patterns

44

about high rain events were therefore constructed using measurements from two nearby radiosonde arrays.

The outflow from deep convection gives rise to pronounced features in the climatological profiles of mass divergence, ozone [*Pickering et al.*, 1993, 2001; *Kley et al.*, 1996; *Folkins et al.*, 2002, 2006; *Solomon et al.*, 2005; *Avery et al.*, 2010], and other chemical tracers [*Lelieveld and Crutzen* 1994; *Lawrence et al.*, 1999, 2003, *Nassar at al.*, 2009; *Liu et al.*, 2010]. Detrainment from congestus clouds gives rise to a second layer of preferred convective outflow near the melting level (~ 5.5 km). The existence of the congestus outflow layer is supported by measurements of cloud top height [*Zuidema*, 1998; *Dessler et al.*, 2006], mass divergence [*Thompson et al.*, 1979; *Mapes et al.*, 2006; *Mitovski et al.*, 2010], and relative humidity [*Johnson et al.*, 1999]. In this paper, we use ozone measurements to demonstrate the existence of the congestus outflow layer.

Unlike the deep outflow layer, the congestus outflow layer does not give rise to a local maximum in climatological profiles of mass divergence, or to a local minimum in climatological profiles of ozone mixing ratio. Anomaly patterns about high rain events are therefore essential for demonstrating the existence of the congestus mode, and for assessing its impact on the mass and ozone budgets of the tropical atmosphere.

The outline of the paper is as follows. In Section 2 we give background information on the various datasets used in the paper. In Section 3, we first give a meteorological overview of the rain events at Fiji and Samoa. We then discuss the methodology used to define the divergence anomaly patterns of two nearby radiosonde arrays. The observed divergence anomaly patterns are compared with patterns produced from the GEOS-4 and GEOS-5 assimilated meteorological datasets. We conclude Section 3 with a discussion of

the cloud top frequency anomaly patterns about high rain events obtained from the CALIPSO instrument. The focus of Section 4 is the construction of an ozone anomaly pattern about high rain events using the SHADOZ dataset, and its comparison with output from the GEOS-Chem chemical transport model. In Section 5, we argue that the observed ozone anomaly patterns are not strongly influenced by lightning generated NO. The main arguments of the paper are summarized in Section 6.

3.3 DESCRIPTION OF DATASETS

3.3.1 TRMM 3B42 RAINFALL

We used the TRMM 3B42 gridded rainfall product to identify rain events at various tropical locations. The TRMM rainfall estimates are constructed from combining several satellite borne instruments, including a precipitation radar, a multi-channel microwave radiometer, and visible and infrared sensors [*Kummerow et al*., 1998]. The dataset has a resolution of 3 hours (centered at the standard synoptic times of 00, 03, 06, 09, 12, 15, 18, and 21 UTC), a horizontal resolution of 0.25° x 0.25°, and extends from 1998 to the present.

3.3.2 SHADOZ OZONE

SHADOZ is an archive of ozonesonde profiles from 13 tropical locations [*Thompson et al*., 2003]. The soundings have been launched approximately two times per month since 1998, and provide high-resolution profiles of ozone mixing ratio. For this analysis, it was desirable to use data from ozonesonde stations located within oceanic regions characterized by frequent deep convection. The presence of a strong diurnal cycle

in the timing of the rain events would have hindered our analysis. We were therefore restricted to islands sufficiently small that the timing of the rain events was not strongly affected by the local sea breeze circulation. The most useful stations were Fiji (18.13 S, 178.40 E) and Samoa (14.23 S, 170.56 W). Between 1998 and 2009, there were 275 ozonesonde launches at Fiji, and 416 launches at Samoa. The locations of Fiji and Samoa are denoted in Figure 3.1 by open squares.
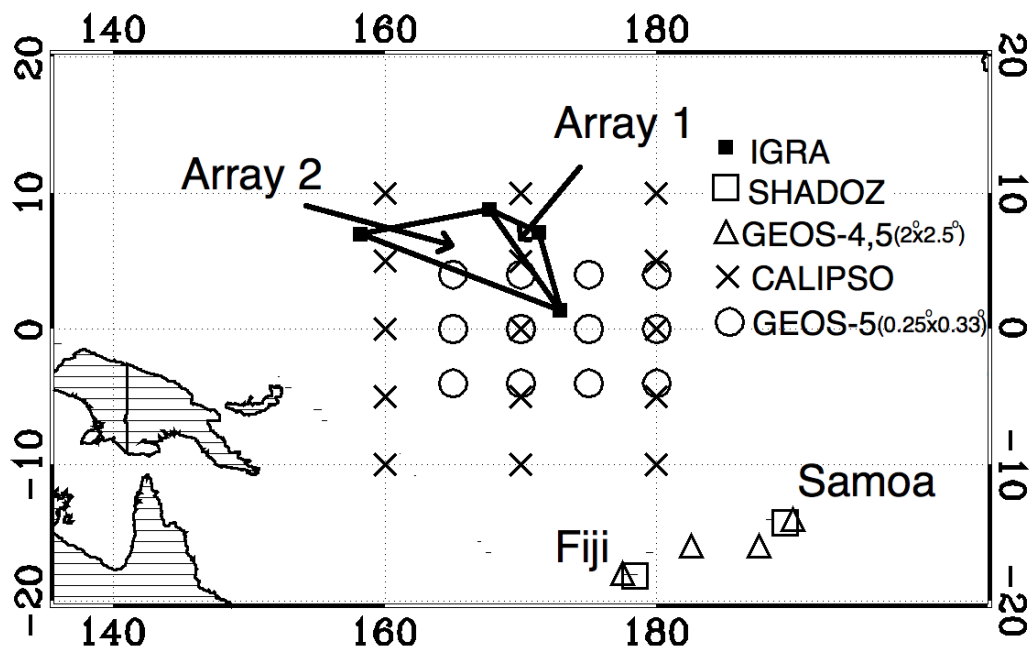
Figure 3.1: A map showing the locations of various observations used in this paper. Radiosonde (IGRA) locations are represented with solid squares. The two SHADOZ sites (Fiji and Samoa) are indicated with open squares. The open triangles show the GEOS-Chem (GEOS-4,5) grid locations used to define the divergence and ozone anomaly patterns of the models. The open circles show the GEOS-5 YOTC grid locations. The CALIPSO locations are indicated by crosses.

3.3.3 IGRA HORIZONTAL WIND

The IGRA (Integrated Global Radiosonde Archive) dataset contains radiosonde profiles stored at the National Climatic Data Center [*Durre et al.*, 2006]. Horizontal wind

measurements from these radiosondes, available at 00 UTC and at 12 UTC, are stored on the standard pressure levels of 1000, 925, 850, 700, 500, 400, 300, 250, 200, 150, and 100 hPa. We used horizontal wind data to calculate the mass divergence profiles of two adjacent triangular arrays, denoted Array 1 and Array 2. The locations of these two triangular arrays are shown in Figure 3.1. Most of the IGRA radiosonde locations have records for the past 30-40 years. Due to the availability of TRMM rainfall data, we used IGRA wind data from 1998 to 2009. Array 1 used radiosonde measurements from Kwajalein Atoll (8.73 N, 167.73 E), Majuro Atoll (7.08 N, 171.38 E), and Tarawa (1.35 N, 172.92 E). It has an area of 112,000 km^2, roughly corresponding to the area of a 3 x 3 degree grid box at the equator. Array 2 also used wind data from Kwajalein Atoll and Tarawa, with the third radiosonde location being Ponape (6.97 N, 158.22 E). It has an area of roughly 480,000 km^2, about four times larger than Array 1.

3.3.4   CALIPSO CLOUD TOPS

We used cloud top information from the Cloud-Aerosol Lidar and Infrared Pathfinder Satellite Observation (CALIPSO) level-2 cloud layer product [*Winker et al., 2009*]. The data are available in a variety of horizontal resolutions. The 1 km horizontal resolution profiles used here are produced from three profiles, each with a horizontal resolution of 0.33 km and a vertical resolution of 30 to 60 m in the troposphere. The detection of cloud tops is based in part on the existence of strong vertical gradients in the backscattered intensity, and an individual profile may be associated with multiple cloud tops. The likelihood of detecting a cloud top at lower altitudes is reduced when obscured by thick clouds at higher altitude. Here, we examined all CALIPSO profiles within the 15

48

2° x 2° grid cells between 10 N and 10 S, and between 160 E and 180 E. These grid cells are represented by crosses in Figure 3.1. This oceanic region is close to Fiji and Samoa, and is characterized by frequent deep convection. There were 648,730 1-km horizontal resolution CALIPSO profiles available within the 15 2° x 2° grid cells used here between June 2006 and December 2009.

The CALIPSO instrument is on a satellite with a sun-synchronous polar orbit that crosses the equator twice a day. There is a modest variation in the local crossing time over the 15 grid cells during the course of a year. The first crossing occurs between 01:08 and 03:00 UTC, while the second crossing occurs between 13:27 and 15:06 UTC. Local solar noon has an annual variation of 23:50 to 1:35 UTC over the 15 grid cells. The first crossing time therefore tends to occur about an hour after solar noon while the second crossing occurs about an hour after local midnight.

3.3.5 GEOS-4 AND GEOS-5 ASSIMILATED METEOROLOGY

Mass divergence anomaly patterns about high rain events were calculated in three assimilated meteorological datasets. The GEOS-4 and GEOS-5 datasets are produced by the Goddard Earth Observing System (GEOS) at the NASA Global Modeling and Assimilation Office (GMAO). We used GEOS-4 and GEOS-5 data from January 2004 to December 2006. Both are archived at a horizontal resolution of 2°x 2.5°. GEOS-4 has 19 vertical layers in the troposphere, while GEOS-5 has 36 vertical layers. The GEOS-4 and GEOS-5 datasets used here were also used to drive the GEOS-Chem model, and have a temporal resolution of 3 hours for rainfall, and 6 hours for the 3D variables.

GEOS-4 and GEOS-5 have different treatments of moist convection. GEOS-4 employs the Zhang and McFarlane parameterization [*Zhang and McFarlane, 1995*] for deep convection, and the Hack scheme [*Hack, 1994*] for shallow convection. GEOS-5 employs the relaxed Arakawa-Schubert convective parameterization for shallow and deep moist convection [*Moorthi and Suarez, 1992*].

We also used a higher spatial resolution 0.25° x 0.33° version of GEOS-5, made available from January 2009 to December 2009 as part of YOTC (Year of Tropical Convection). This dataset was archived at a temporal resolution of 1 hour for rainfall, and 3 hours for 3D variables.

3.3.6 THE GEOS-CHEM CHEMICAL TRANSPORT MODEL

The GEOS-Chem chemical transport model [*Bey et al., 2001*] version v8-03-01 (www.geos-chem.org) can be driven by a variety of meteorological datasets. The GEOS-Chem simulations discussed here were driven by the GEOS-4 and GEOS-5 assimilated meteorological datasets described above. These simulations extend from January 2004 to December 2006.

3.4 METEOROLOGICAL BACKGROUND

3.4.1 RAIN EVENT DEFINITION

The ozone anomaly pattern produced by a group of rain events will be sensitive to the spatial extent, duration, and intensity of the events. We first averaged the 0.25° x 0.25° TRMM 3B42 rainfall dataset to a lower spatial resolution of 2° x 2°. This ensured that the size of the observed rain events would be similar to the GEOS-4 and GEOS-5

grid resolution.

Rain events were considered to occur at Fiji or Samoa if the 3-hour rain rate at the 2° x 2° TRMM grid cell containing one of these islands exceeded a particular threshold. The selection of this threshold requires a compromise between the number of rain events and their intensity. We wanted the rain event threshold to be large enough that the rain events would be associated with significant perturbations in the ozone mixing ratio from climatology. On the other hand, given the limited number of ozonesondes at Fiji and Samoa, the rainfall event threshold had to be small enough that a sufficient number of ozonesonde profiles would be available to construct the ozone anomaly patterns. By using a rain event threshold of 1.5 mm/h, there were 116 ozonesondes at Samoa and 158 ozonesondes at Fiji, between 1998 and 2009, that occurred within 24 hours of a 2° x 2° 3-hour TRMM rain event. Rain events of this intensity were sufficiently infrequent at the other oceanic SHADOZ locations that the use of ozonesondes from these additional locations would not have contributed significantly to the number of ozonesondes available.

Figure 3.2 shows the spatial variation of the average rainfall anomaly at Fiji and Samoa for all rain events at these two locations using the above definition. The maps were obtained by first determining the rainfall distribution at Fiji and Samoa during a rain event using the native 0.25° x 0.25° resolution. After subtracting the appropriate seasonal mean from each high-resolution rainfall map, the high spatial resolution rainfall anomalies from all rain events at each location were added together. The 2° x 2° TRMM rain events at Fiji and Samoa are clearly larger than their respective islands, spread

51

significantly outside the 2°x 2° boxes used in their definition, and synoptic in scale (rather than being associated with mesoscale diurnal circulations).

The locations of the ozonesonde stations at Fiji and Samoa are denoted by crosses in Figure 3.2. Within a rain event, the effect of convection on the ambient ozone mixing ratio can be expected to scale with the convective mass fluxes, which should scale with the rain rate. The ozone anomalies associated with the rain events should therefore also be synoptic in scale, rather than being localized to the ozonesonde stations. The relative influence of horizontal advection on the ambient ozone mixing ratio can be expected to be larger on the periphery of an event.
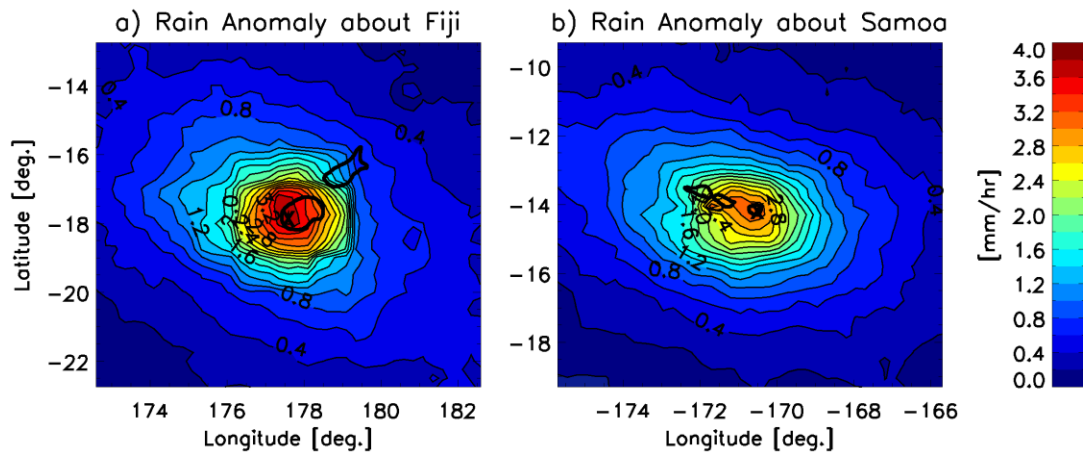
Figure 3.2: The rain anomaly map about high rain events for (a) Fiji and (b) Samoa. The locations of the sounding sites are at the center of each plot, and are represented with crosses. The outlines of the islands are indicated with thick black lines. The rain anomaly map is an average of the rain anomaly maps for all rain events during the 1998-2009 period. In calculating the rain anomaly about a rain event, we used the 0.25-degree 3B42 TRMM gridded rainfall dataset.

The rain events at Fiji and Samoa are typically quite short. Figure 3.3(a) shows the composite rain event profile obtained by averaging over all rain events at Fiji and Samoa that were associated with at least one ozonesonde. The time at which the rain event is defined corresponds to t = 0 on the horizontal axis. During a rain event, the rain rate

decreases to one half of peak intensity within about four hours of peak rainfall. Two

vertical lines in Figure 3.3(a) indicate this time interval. There is also some enhancement

in rain rate above background for up to 20 hours prior to peak rainfall.
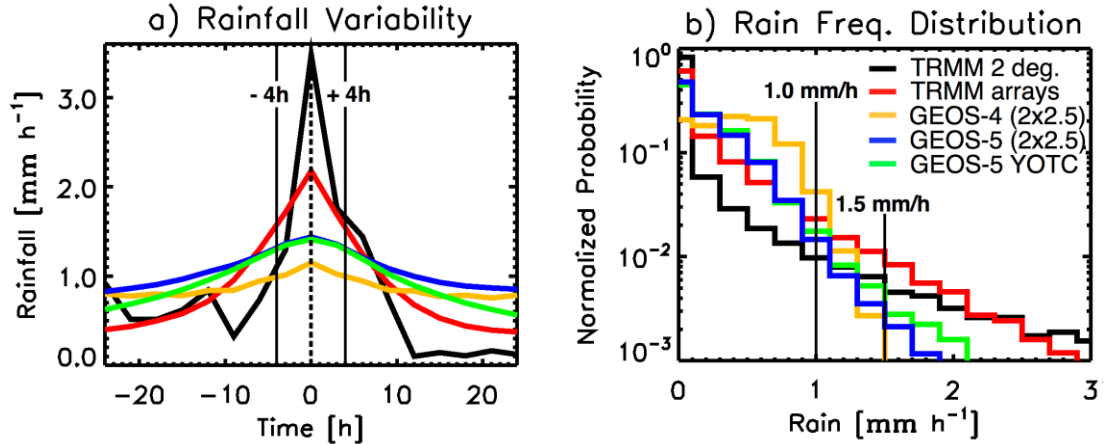
Figure 3.3: a) Variation in time of the mean rainfall rate during the rain events associated with various rainfall datasets. t = 0 corresponds to the time at which the rain event is defined; b) Rain frequency distribution per 0.2-mm/hr-rainfall bin. The black line shows TRMM 3B42 2x2 degree rain frequency distribution, the red line shows TRMM 3B42 over arrays, the golden line shows GEOS-4 2x2.5 degree, the blue line shows GEOS-5 2x2.5 degree, and the green line shows GEOS-5 0.25x0.33 degree rain frequency distribution.

The GEOS-4 and GEOS-5 rain events were defined using a procedure similar to

that used for the TRMM rain events. However, the frequency of occurrence of high

rainfall rates in the GEOS-4 and GEOS-5 rainfall datasets is substantially less than in the

TRMM 2° x 2° rainfall dataset. Figure 3.3(b) shows that the frequency of occurrence of

rainfall rates in excess of 1.5 mm/h is very low. In order to obtain a reasonable number of

GEOS-4 and GEOS-5 rain events, we therefore adopted a reduced rain event threshold of

1.0 mm/h. Two vertical lines in Figure 3.3(b) show the 1.0-mm/h and the 1.5-mm/h rain

thresholds.

We further increased the number of GEOS-4 and GEOS-5 rain events by

considering rain events not only at the two grid points containing Fiji (18 S, 177.5 E) and Samoa (14 S, 170 W), but also at the two nearby grid cells of (16 S, 177.5 W) and (16 S, 172.5 W). The four grid cells used to define the GEOS-4 and GEOS-5 rain events are indicated by open triangles in Figure 3.1.

3.4.2 DIURNAL ISSUES

Figure 3.4(a) shows the diurnal variation of the mean TRMM rain rate in the 2° x 2° grid cells containing Fiji and Samoa between 1998 and 2009. Local solar noon varies between 23:50 and 0:20 UTC over the course of a year at Fiji, and between 23:10 and 23:40 UTC at Samoa. Over land, the diurnal cycle in tropical rainfall tends to exhibit a peak in the late afternoon or early evening [*Nesbitt and Zipser, 2003*]. Over the oceans, the amplitude of the diurnal cycle is much smaller, with a tendency for peak rainfall early in the morning [*Nesbitt and Zipser, 2003*]. Figure 3.2 shows that the land area of the Fijian and Samoan islands is smaller than the TRMM 2° x 2° grid cells within which they are located. The diurnal cycle in rainfall within the two grid cells is therefore likely to be affected by both land and ocean forcings. Figure 3.4(a) shows there is a weak diurnal cycle at both grid cells. The diurnal cycle at the Samoan grid cell (solid curve) exhibits an early morning peak and appears to be more strongly influenced by the ocean. The diurnal cycle at the Fijian grid cell (dashed curve) exhibits an afternoon peak and appears to be more strongly influenced by land.

Figure 3.4(b) shows the diurnal variation in the total number of TRMM rain events at the two grid cells containing Fiji and Samoa, plotted as the number of rain events per three hour interval between 1998 and 2009, using the rain event definition discussed

above. There is a tendency for the rain events of the Samoan grid cell to occur near sunrise (about 12 UTC). A particular rain event contributes to the ozone anomaly pattern at Fiji or Samoa only if there is an ozonesonde launched within 24 hours of the event. Figure 3.4(d) shows that the ozonesondes at Fiji and Samoa tend to be launched near local solar noon. The diurnal cycle in the timing of the subset of the rain events used to produce the ozone anomaly patterns is shown in Figure 3.4(c). At both Fiji and Samoa, the diurnal cycle in the number of rain events that occur within 24 hours of an ozonesonde launch is weak.
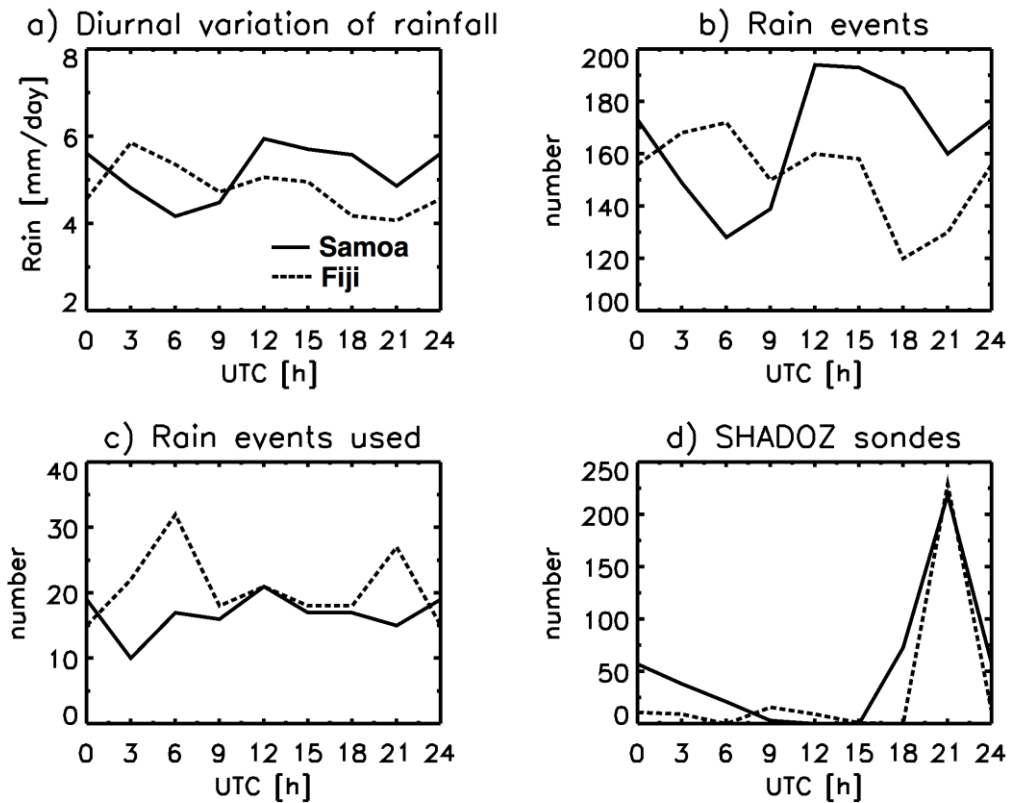
Figure 3.4: a) Diurnal variation of the 2x2 degree TRMM rainfall at Samoa (solid) and Fiji (dashed); b) total number of rain events per 3 hour interval for a rainfall threshold of 1.5 mmh^{-1}; c) number of rain events used to calculate the ozone anomaly patterns; d) diurnal variation in the launch time of the SHADOZ soundings. Local solar noon varies over the course of a year at Fiji between 23:50 and 0:20 UTC. Local solar noon at Samoa is between 23:10 and 23:40 UTC.

3.4.3   MASS DIVERGENCE ANOMALY PATTERNS FROM OBSERVATIONS

Convective clouds affect the concentrations of chemical tracers in the background atmosphere partly by entraining air from their environment and by detraining air into their environment. Within a population of growing convective clouds, entrainment usually exceeds detrainment at low levels, giving rise to a net horizontal transport of mass from the background atmosphere toward the growing clouds. This inward horizontal transport is ordinarily associated with low-level convergence. Conversely, the atmosphere tends to be divergent at height regions where detrainment exceeds entrainment. Preferred layers of inflow and outflow can be diagnosed from mass divergence anomaly patterns. These divergence patterns help interpret the anomaly patterns obtained from chemical tracers such as ozone.

Mass divergence anomaly patterns can be calculated using simultaneous horizontal winds from triangular arrays of radiosondes, launched either as part of an intensive field campaign [e.g. *Mapes et al.*, 2006], or from routine radiosonde profiles over land [*Mitovski et al.*, 2010]. Here, we use routine horizontal wind observations over a 12-year period (1998 – 2009) from two radiosonde arrays in the IGRA archive (called Array 1 and Array 2) near Kwajalein to diagnose the vertical variation of the net convective inflow and outflow associated with rain events over the western tropical Pacific Ocean. The locations of the two arrays are shown in Figure 3.1. Array 1 and Array 2 were chosen in part because they are close to Fiji and Samoa. The divergence anomaly patterns of the two arrays should therefore be similar to the divergence patterns of the rain events at Fiji and Samoa. In addition, because both arrays have an area comparable with a 2° x 2° grid cell, their divergence anomaly patterns can be compared with those calculated from the

GEOS-4 and GEOS-5 assimilated meteorological datasets.

Individual divergence profiles were first constructed from IGRA horizontal wind observations by interpolation from the vertices of each radiosonde array to the center of each side. The seasonal mean divergence profiles of the two standard radiosonde launch times were constructed for each array by averaging over the individual profiles.

Rain events at Arrays 1 and 2 were determined by first calculating a time series of the average rain rate within each array from the high resolution 0.25°x 0.25° TRMM rainfall product. Figure 3.3(b) shows the frequency distribution of the TRMM rain rate averaged over each of the two arrays. It is similar to the frequency distributions associated with the 2° x 2° Samoan and Fijian grid cells. Rain events within the two arrays were therefore considered to also occur at times when the average rain rate within each array exceeded a 1.5 mm/h threshold. With this choice, there were 1339 mass divergence profiles at Array 1, and 805 divergence profiles at Array 2, that occurred within 24 hours of a rain event. Mass divergence anomalies were calculated by subtracting from the individual profiles the seasonal mean divergence profile with the same launch time. The divergence anomaly profiles were then grouped into 3-hour time bins based on the time difference between the time of the divergence measurement and the time of the rain event. The anomaly profiles were then averaged to produce a composite mass divergence anomaly pattern for each array. These are shown in Figure 3.5(a) and 3.5(b).

The mass divergence anomaly patterns of Arrays 1 and 2 are similar. Both exhibit convergence near the surface prior to peak rainfall, a strong upper level divergence near 13 km at t = 0, and an antisymmetric divergence dipole near 6 km. The strong upper level

57

divergence centered at peak rainfall is presumably due to deep convection. The mid-level divergence dipole consists of a divergence 8 hours prior to peak rainfall and a convergence 8 hours after peak rainfall. The mid-level divergence maximum prior to peak rainfall has been interpreted as a signature of cumulus congestus clouds [*Thompson et al.*, 1979; *Mapes et al.*, 2006; *Mitovski et al.* 2010]. The mid-level convergence maximum after peak rainfall can be attributed to precipitating stratiform anvil clouds. These clouds are associated with a downdraft mass flux that increases below the melting level (~ 5.5 km). The required downdraft entrainment can be expected to be balanced in part by an inward convergent mass flux from the background atmosphere.
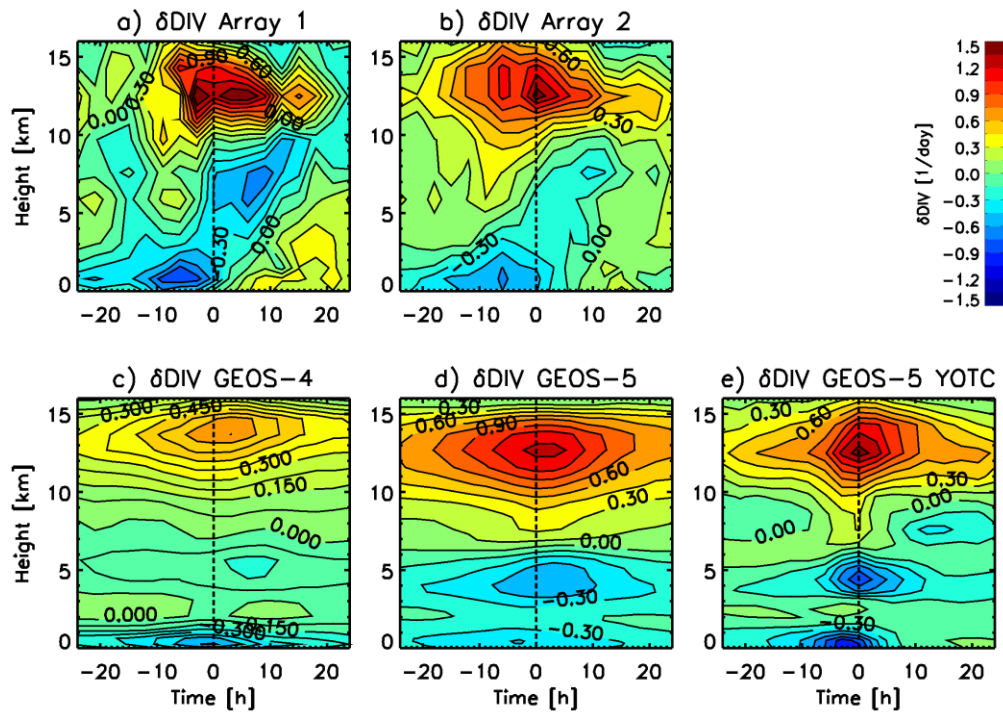
Figure 3.5: Divergence anomaly patterns about high rainfall events. The anomalies are with respect to seasonal mean profiles. The rain event threshold for the observed divergence anomaly patterns was 1.5 mmh^{-1}. For the models, we used a rain threshold of 1.0 mmh^{-1}. a) Observed divergence anomaly pattern over Array 1 and b) Observed divergence anomaly pattern over Array 2 using IGRA radiosonde data; c) Divergence anomaly generated using GEOS-4 meteorology; d) Divergence anomaly generated using GEOS-5 meteorology, and e) Divergence anomaly generated using a version of GEOS-5 with higher spatial resolution (YOTC).

The mid-level divergence dipole of Array 1 is stronger than the divergence dipole of Array 2. This difference may be due to the difference in area between the two arrays. For a given average rain rate, a larger radiosonde array will in general contain a greater mixture of cloud types at different stages of development than a smaller array. In particular, one would expect a larger array to contain a more diverse mixture of congestus and precipitating stratiform anvil clouds. Because the congestus divergence and stratiform convergence features occur at the same height, and are of opposite sign, they tend to cancel in a spatial average. The mid-level divergence dipole can therefore be expected to become progressively weaker when defined for rain events of larger arrays [*Folkins et al.*, 2008]. The larger size of Array 2 may therefore account for the weakness of its mid-level divergence dipole relative to Array 1.

The progressive disappearance of the mid-level divergence dipole, in response to an increase in size of the averaging region, also applies to temporal averages. Figure 3.6 shows the climatological divergence profiles of Arrays 1 and 2 from 1998 to 2009, averaged over all times in which the rain rate within each array exceeded 4 mm/day. Although the deep outflow mode is very prominent, there is no evidence of a congestus divergence or a stratiform convergence. This demonstrates the importance of using divergence anomaly patterns about high rain events to isolate these features.
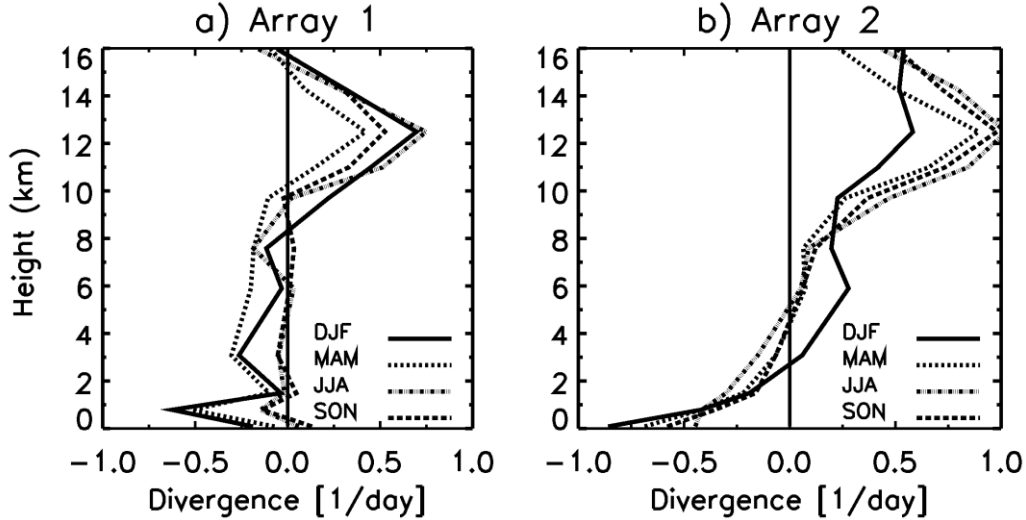
Figure 3.6: Seasonal mean divergence profiles of a) Array 1 and b) Array 2 from 1998 to 2009, averaged over all times in which the rain rate within each array exceeded 4 mm day^{-1}. The locations of Arrays 1 and 2 are shown in Figure 3.1.

3.4.4 MASS DIVERGENCE ANOMALY PATTERNS FROM GEOS-4 AND GEOS-5

Meteorological datasets can be used to construct mass divergence anomaly patterns about high rain events using a procedure similar to that described above for radiosonde arrays, except that the divergence is calculated from spatial derivatives in the horizontal wind using wind information at the four closest grid cells. As discussed previously, we also used a lower rain event threshold for the GEOS-4 and GEOS-5 rain events (1.0 mm/h rather than 1.5 mm/h), and considered rain events at two nearby grid cells in addition to the grid cells containing Fiji and Samoa.

The mass divergence anomaly patterns of these four grid cells are shown in Figures 3.5(c) and 3.5(d). The divergence anomaly patterns of GEOS-4 and GEOS-5 show some features that are consistent with observations. These include a boundary layer convergence feature and an upper tropospheric divergence feature. However, unlike the observations, the boundary layer convergence features of GEOS-4 and GEOS-5 are

60

coincident rather than prior to peak rainfall. In addition, the GEOS-4 and GEOS-5 divergence anomaly patterns do not exhibit a mid-level divergence dipole. Instead, the two models exhibit a mid-level convergence maximum centered at peak rainfall ($t = 0$). These differences are consistent with previous results showing that the mid-level divergence dipole is poorly represented in both climate models and assimilated meteorological datasets [*Mitovski et al*., 2010]. Figure 3.5 also shows that the GEOS-4 divergence anomalies are smaller than the GEOS-5 divergence anomalies. This is consistent with the smaller enhancement above background of the GEOS-4 rainfall rates during rain events (shown in Figure 3.3(a)).

The weaknesses in the representation of the mid-level divergence dipole in global models could be due in part to a lack of spatial resolution. We have therefore calculated the mass divergence anomaly pattern of the higher spatial resolution (0.25° x 0.33°) YOTC version of GEOS-5. We looked for rain events at the 12 grid cells in this high resolution dataset nearest the two IGRA radiosonde arrays. These were located between 165 E and 180 E and 4 S and 4 N, and are indicated by circles in Figure 3.1. The rainfall frequency distribution of the 12 grid cells is shown in Figure 3.3(b). Although there is a slightly increased incidence of high rainfall rates, it is similar to the rain frequency distribution of the lower spatial resolution version of GEOS-5 (shown in blue). High rain events from the high spatial resolution version of GEOS-5 were therefore also considered to occur during times at which the rain rate exceeded 1.0 mm/h.

Figure 3.5(e) shows the mass divergence anomaly pattern of the high resolution GEOS-5 YOTC dataset, evaluated at the 12 grid cells discussed above. It is similar to the divergence pattern produced by the lower spatial resolution version of GEOS-5. The

main difference with the observed anomaly pattern is that the mid-level convergence feature occurs at t = 0, whereas the observed anomaly pattern exhibits a mid-level divergence dipole that is antisymmetric about t = 0.

Although the intensity of a divergence anomaly patterns is sensitive to the rain event threshold, the overall shape of the anomaly pattern is not strongly sensitive to this threshold. It can be shown that the high-resolution divergence anomaly pattern generated using a rain event threshold of 1.5 mm/h is similar to the pattern generated using a threshold of 1.0 mm/h.

3.4.5   CLOUD TOP FREQUENCY ANOMALY PATTERN FROM CALIPSO

Cloud top height measurements do not give direct insight into the vertical profile of mass detrainment from a convective cloud, except that one can usually assume that convective outflow is vertically distributed between cloud base and cloud top. Nevertheless, cloud top anomaly patterns about high rain events do provide an interesting complement to the mass divergence patterns discussed above.

The cloud top anomaly patterns were produced as follows. We first looked for 2° x 2° TRMM rain events from the 2006 - 2009 CALIPSO period at the 15 locations indicated by crosses in Figure 3.1 (again using the 1.5 mm/h TRMM rain event threshold). Once a TRMM rain event was identified, we searched for 1 km horizontal resolution CALIPSO profiles (both cloudy and clear) inside the 15 2° x 2° grid cells that occurred within 24 hours of a TRMM event. The vertical resolution of the cloud top data of each profile was reduced to 1 km, and each profile was assigned to a 3 hour time bin based on the difference between the CALIPSO measurement time and the time of the

TRMM rain event. The number of cloud tops in each 1 km layer and 3-hour time bin was then normalized by the total number of CALIPSO profiles (cloudy + clear sky) used in that time/height bin. This procedure was repeated for each season. Finally, we subtracted the seasonal mean cloud top frequency from the cloud top patterns for each season, and then averaged the four anomaly patterns together. This produced the annual mean cloud top frequency anomaly pattern shown in Figure 3.7.

The most prominent feature of the cloud top frequency anomaly pattern is a very strong positive anomaly that develops at upper levels 12 hours prior to peak rainfall (t = 0). The onset of this anomaly is roughly coincident with the onset of the deep convective divergence anomaly shown in Figure 3.5(a) and 3.5(b). The 3 km vertical offset between the deep convective divergence (~ 13 km) and cloud top frequency (~ 16 km) anomalies demonstrates the absence of a direct relationship between mass outflow and cloud top height. The upper level cloud top anomaly is probably due to some combination of direct injection of ice crystals from deep convective detrainment, and *in situ* ice crystal formation that develops in response to an upper level cooling near 16 km that occurs in association with high rain events [*Mitovski et al., 2010*].

Figure 3.8 shows the seasonal mean cloud top frequency profiles from all 15 grid cells. The overall shape of this profile is consistent with cloud top frequency climatologies from previous lidar measurements [*Dessler et al*., 2006]. The modest peak between 5 and 8 km of about 4% per km can be attributed to congestus clouds.
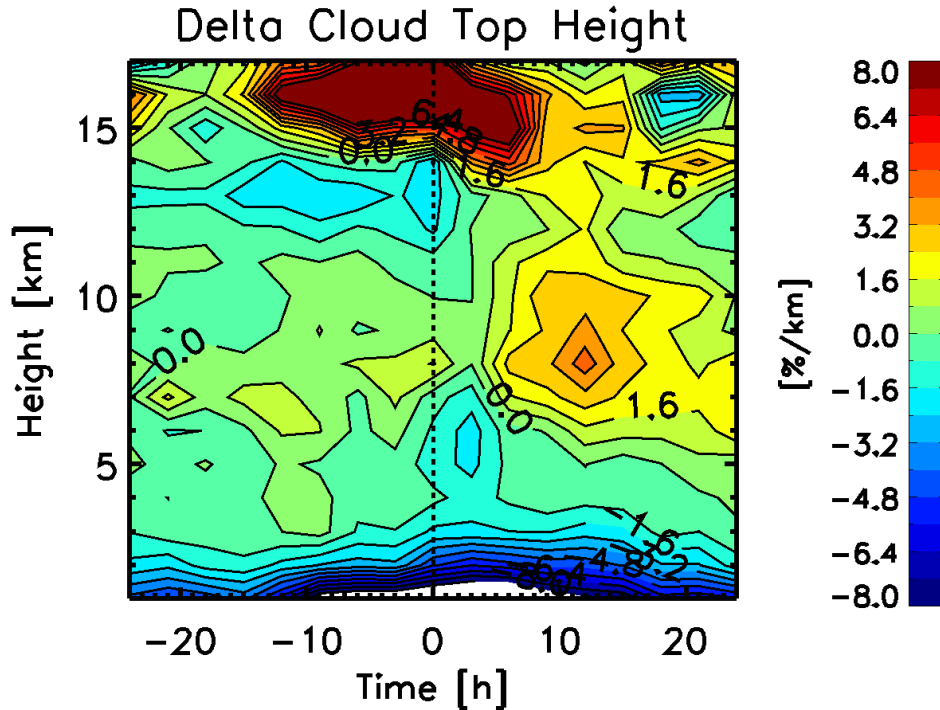
Figure 3.7: Cloud top frequency anomaly patterns. The anomaly pattern was generated using the 1-km horizontal resolution CALIPSO cloud top measurements, and 2 x 2-degree TRMM 3B42 rainfall data over 15 tropical locations (shown with crosses in Figure 3.1) for the period between 2006 and 2009.

The cloud top anomaly pattern shows that there is an absolute increase of 1-3% per km in the frequency of occurrence of cloud tops between 5 and 8 km up to 15 hours prior to peak rainfall (t = 0). This corresponds to a relative increase above background of about 50%. Some of the congestus clouds that develop prior to peak rainfall are probably obscured by the increased incidence of high altitude cirrus clouds. As a result, the magnitude of the mid-level cloud top enhancement prior to peak rainfall may be underestimated.
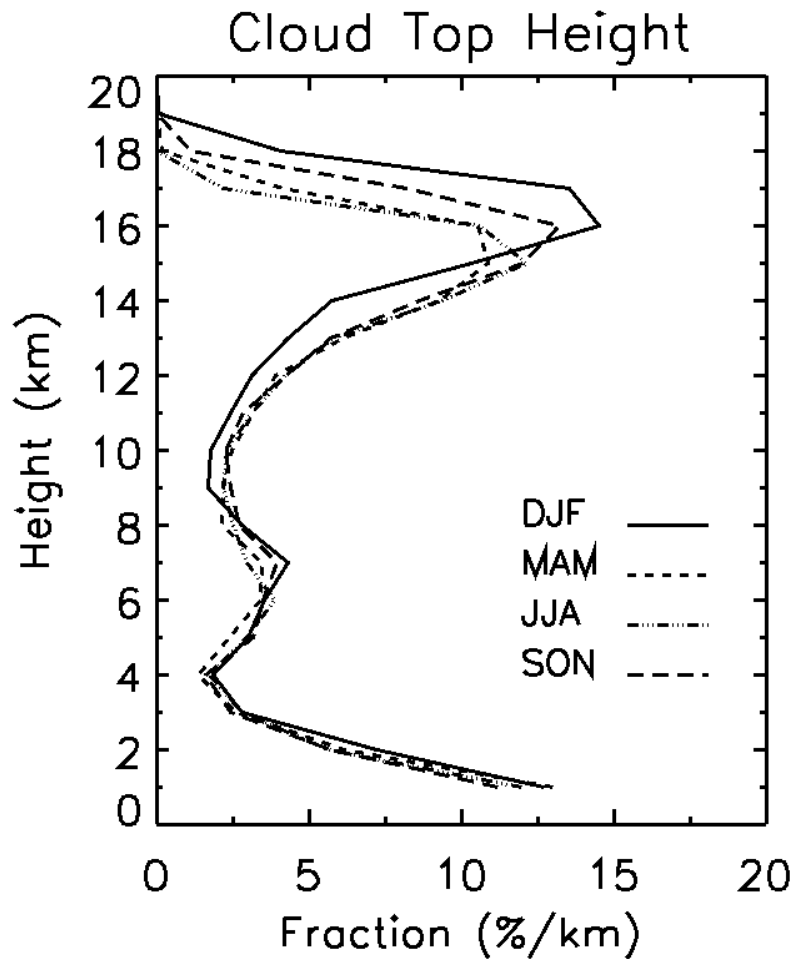
Figure 3.8: Seasonal mean cloud top frequency profiles from all 15 grid cells. The crosses in Figure 3.1 show the locations of the 15 grid cells. The profiles were calculated using CALIPSO measurements for the period 2006-2009.

The cloud top anomaly pattern also shows that there is an increased incidence of clouds with tops between 5 and 12 km that develops after peak rainfall. This corresponds to a period when an increased incidence of stratiform anvil clouds is expected. This increase is coincident with a decrease in the occurrence of high altitude cirrus clouds. Presumably, this decrease allows the lidar to penetrate to lower heights, and measure cloud tops that had previously been obscured.

The cloud top anomaly pattern shown in Figure 3.7 was constructed using CALIPSO observations from both local noon and local midnight crossing times. Although there is a diurnal cycle in cloudiness associated with the diurnal cycle in rainfall over the oceans, it can be shown that the cloud top anomaly patterns produced by the two sets of profiles are similar.

3.5 OZONE

3.5.1 OZONE ANOMALY PATTERNS FROM SHADOZ OBSERVATIONS

Rapid rates of ozone destruction generate low ozone mixing ratios in the tropical marine boundary layer. Layers of preferred convective detrainment should therefore be associated with negative ozone anomalies. Figure 3.9 shows seasonal mean ozone mixing ratio profiles at Fiji and Samoa, generated by all SHADOZ measurements from 1998 to 2009. The upper tropospheric minimum in ozone mixing ratio near 13 km is characteristic of oceanic regions with frequent deep convection, and has been attributed to a local maximum in deep convective outflow at the same altitude [*Lawrence et al., 2003, Folkins and Martin, 2005*].

There is no evidence in Figure 3.9 of a mid-tropospheric minimum in mean ozone mixing ratios associated with enhanced detrainment from congestus clouds. Instead, there is a local maximum in ozone mixing ratio near 6 km. This maximum has been attributed to a change in the sign of the rate of chemical ozone production. Ozone is chemically produced in the upper troposphere at a rate of 1 - 2 ppbv/day [*Jacob et al*., 1996]. After detraining from a deep convective cloud, the ozone mixing ratio of an air parcel will therefore initially increase as it sinks toward the surface. However, the rate of ozone

destruction from the $O(^1D) + H_2O \rightarrow 2OH$ reaction increases with the rise in ambient water vapor concentrations. At some point, usually in the mid-troposphere, the net ozone production becomes negative and the ozone mixing ratio of an air parcel will decrease with continued sinking toward the surface (at least in unpolluted regions). This change in net chemical production has been used to explain the decrease in climatological ozone mixing ratio below 6 km [*Folkins and Martin, 2005*]. However, it is likely that the ozone decrease below 6 km is at least partially attributable to increased detrainment from congestus clouds, both by direct injection of lower ozone air from the boundary layer, and by providing a source of water vapor. In this section, we use ozone anomaly patterns about high rain events to demonstrate that direct injection of low ozone air from the boundary layer does indeed generate negative ozone anomalies in the mid-troposphere, and therefore has an impact on mean ozone profiles.
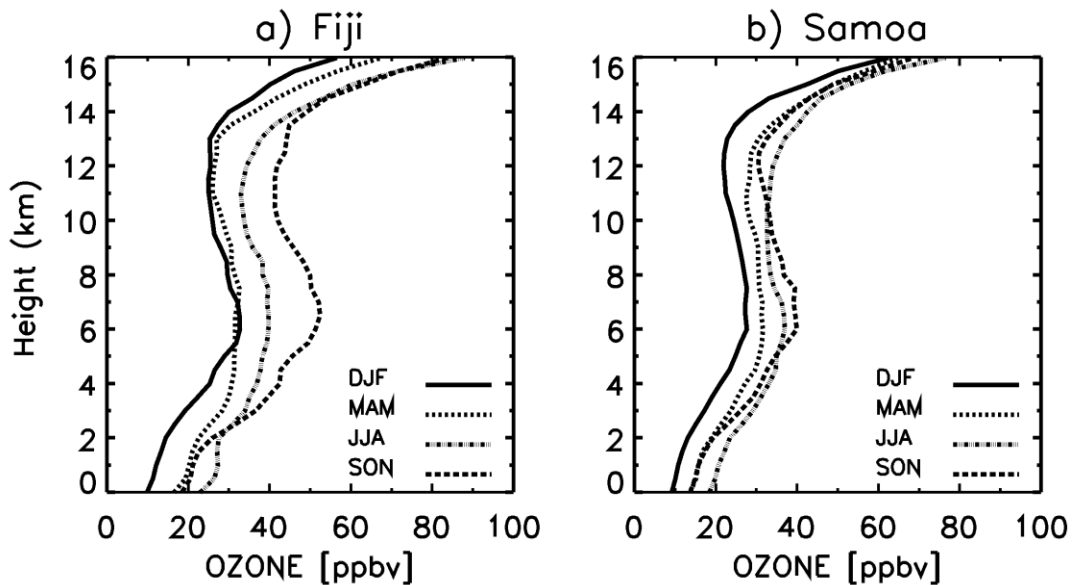
Figure 3.9: Seasonal mean ozone profiles at a) Fiji and b) Samoa. The seasonal profiles were calculated using SHADOZ soundings for the period 1998-2009.

Ozone anomaly patterns about high rain events were defined using a procedure similar to the procedure used above for the mass divergence and cloud top frequency anomaly patterns. We used all ozonesondes at Fiji and Samoa within 24 hours of a TRMM rain event at the 2° x 2° grid cells containing Fiji and Samoa. The ozonesondes were grouped into 3-hour time bins based on the difference between the time of the ozonesonde launch and the time of the rainfall event. Ozone anomalies were calculated by taking the deviation from the appropriate seasonal mean, and then averaged to produce an annual mean ozone anomaly pattern. The ozone anomaly patterns at Fiji and Samoa were similar, and therefore combined into a single composite anomaly pattern. This composite pattern is shown in Figure 3.10(a).

The ozone anomaly pattern shows that negative ozone anomalies develop at mid-levels roughly 16 hours prior to peak rainfall. This mid-level ozone decrease develops in concert with enhancements in the frequency of mid-level cloud tops, and extends over a similar altitude range (4 – 8 km). The mid-level negative ozone anomalies that develop prior to peak rainfall can therefore be attributed to increased detrainment from congestus clouds.

Within several hours of peak rainfall (t = 0), there is a strong negative ozone anomaly that extends from the boundary layer to the tropopause. The duration of this full depth negative ozone anomaly is approximately coincident with the upper level divergence anomaly, and can therefore be attributed to enhanced outflow from deep convection.

Figure 3.10(a) also shows that positive ozone anomalies develop near the tropopause (~ 17 km) after peak rainfall. These ozone anomalies appear to be associated with the propagation of Kelvin waves.
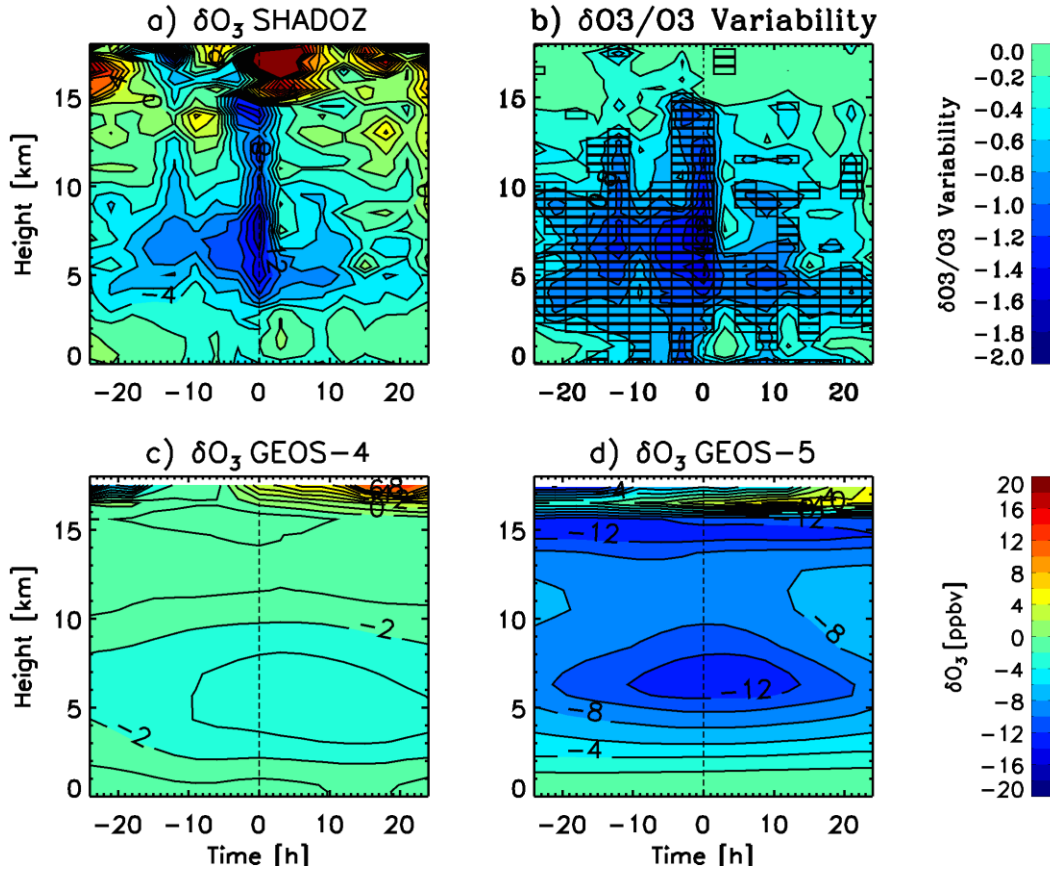
Figure 3.10: Observed and modeled ozone anomaly pattern about high rain events. The anomalies are with respect to seasonal mean profiles. The rain event threshold for the observed ozone anomaly patterns was 1.5 mmh[-1]. For the models, we used a rain threshold of 1.0 mmh[-1]. a) Observed ozone anomalies at Fiji and Samoa using SHADOZ data; b) Ratio of the ozone anomalies in panel A to the background variability. The black rectangles in panel B show the locations of the mean ozone anomalies that are considered significant according to a version of t test with p=0.05; c) Ozone anomalies from GEOS-Chem using GEOS-4 meteorology, and d) Ozone anomalies from GEOS-Chem using GEOS-5 meteorology.

3.5.2 OZONE ANOMALY PATTERNS FROM GEOS-CHEM

Rain events were selected from the GEOS-4 and GEOS-5 precipitation datasets

using the same procedure previously used when constructing the GEOS-4 and GEOS-5 divergence anomaly patterns. We then selected ozone profiles from the GEOS-Chem model within 24 hours of the GEOS-4 and GEOS-5 rain events between January 2004 and December 2006. Ozone anomalies were calculated by taking the difference from seasonal mean ozone profiles defined over the same time period. The ozone anomaly patterns generated by the GEOS-Chem model using GEOS-4 and GEOS-5 meteorology are shown in Figures 3.10(c) and 3.10(d). The GEOS-4 ozone anomalies are about twice as small as the GEOS-5 ozone anomalies. This is consistent with the relative strength of the GEOS-4 and GEOS-5 divergence anomalies, and appears to reflect the smaller increase above background of the GEOS-4 rain rates during rain events.

In both GEOS-4 and GEOS-5, convection gives rise to two layers of reduced ozone, roughly centered at 6 and 16 km. The mid-level ozone reductions of the two GEOS-Chem simulations are roughly symmetric about peak rainfall (t = 0), whereas the observed mid-level ozone reductions are strongest prior to peak rainfall. Both versions of GEOS-Chem exhibit upper level negative ozone anomalies that are much more persistent than the observations, presumably reflecting the greater persistence of the GEOS-4 and GEOS-5 rain events (shown in Figure 3.3(a)).

3.5.3 STATISTICAL SIGNIFICANCE OF OBSERVED OZONE ANOMALIES

The ozone anomaly pattern shown in Figure 3.10(a) is clearly noisy, and some of the features would probably not appear in an anomaly pattern constructed from a larger number of ozonesondes. One way to assess the statistical significance of the ozone anomaly $\overline{\delta O_3}(z,t)$ of a given height-time bin is to divide the anomaly by a measure of the

variability in background ozone. We calculated the vertical profile of the standard deviation in ozone mixing ratio at Fiji and Samoa for each of the four seasons using the following formula.

$$\sigma_{all}(z) = \sqrt{\frac{1}{m-1}\sum_{i=1}^{m}\left[O_{3,i}(z) - \overline{O_3}(z)\right]^2} \tag{3.1}$$

$O_{3,i}(z)$ refers to an ozone measurement at height z from sonde i; m refers to the total number of sondes at Fiji or Samoa between 1998 and 2009 during a season, and $\overline{O_3}(z)$ refers to the appropriate seasonal climatological profile. The four seasonal standard deviation profiles of each location were averaged to produce a combined annual mean standard deviation for Fiji and Samoa. The ratio of the mean ozone anomaly to the standard deviation is shown in Figure 3.10(b). In general, the ozone anomaly exceeds the background variability in regions where the anomaly itself is largest: at mid-levels prior to peak rainfall, and throughout the troposphere during high rainfall events.

We also used a version of the T test to determine the statistical significance of the ozone anomalies. In this test, the mean ozone anomaly of each bin is divided by a standard deviation that is calculated from the ozone anomalies of the rain events.

$$T_{test} = \frac{\overline{\delta O_3}(z,t)}{\sqrt{\sigma_{event}^2(z,t)/n}} \tag{3.2}$$

The standard deviation of the event ozone anomalies is give by

$$\sigma_{event}(z,t) = \sqrt{\frac{1}{n-1}\sum_{i=1}^{n}\left[\delta O_{3,i}(z,t) - \overline{\delta O_3}(z,t)\right]^2} \tag{3.3}$$

where $\delta O_{3,i}(z,t)$ refers to a rain event ozone anomaly at height z from sonde i, and n is the total number of ozone anomaly measurements in a particular time/height bin (typically around 20). The mean ozone anomalies are considered to be significant if the value of T_{test} is greater than a particular tabulated value $T_{crit}(n,p)$ [*Armitage et al.*, 2002], where p refers to the likelihood that the observed mean anomalies could have been generated by chance alone. Here, we used 95 percent statistical significance threshold, setting p = 0.05. The black rectangles in Figure 3.10(b) show the locations of the mean ozone anomalies that are considered significant according to this criterion.

Some features of the observed ozone anomaly pattern are unlikely to be robust, despite being considered statistically significant according to the T test. For example, the mean TRMM rain event profile shown in Figure 3.3(a) was constructed from only those rain events at Fiji and Samoa between 1998 and 2009 that occurred within 24 hours of an ozonesonde. It exhibits a secondary rainfall peak at -12 hours that appears to be associated with coincident negative ozone anomalies above 8 km. However, this secondary rainfall peak does not appear in the mean TRMM rain event profile constructed from all rain events at Fiji and Samoa between 1998 and 2009. It is therefore unlikely that the negative ozone anomaly above 8 km at -12 hours would occur in an ozone anomaly pattern constructed from an ozonesonde dataset with a higher sampling rate (i.e. more frequent than the biweekly sampling rate used in SHADOZ).

3.6 LIGHTNING

We have attributed the negative ozone anomalies associated with high rain events to the effects of convective transport. However, lightning also occurs during deep

convection and affects the ozone budget in a variety of ways. The NO that is produced by lightning destroys ozone on short timescales (due to the reaction of NO with ozone), but produces ozone on longer timescales. In-situ measurements of lightning NO_x (NO + NO_2) in the vicinity of deep convection were made during the "Stratospheric Climate Links with Emphasis on the Upper Troposphere and Lower Stratosphere" (SCOUT-O3) and "Aerosol and Chemical Transport in Deep Convection" (ACTIVE) aircraft campaigns, conducted over northern Australia in November-December 2005 [*Vaughan et al.*, 2008]. NO_x enhancements due to lightning were about 1 ppbv in the upper troposphere, and less than 0.5 ppbv in the middle troposphere [*Huntrieser et al.*, 2009]. In the tropics, lightning is much less frequent over the oceans than over land [*Christian et al., 2003*], so these NO_x enhancements should be considered an upper limit for Fiji and Samoa. On the short timescales relevant to this analysis, the expected decreases in ozone associated with lightning generated NO can be assumed to be less than 1 ppbv.

3.7 SUMMARY

This paper has outlined a new methodology for assessing the impact of convection on the background distribution of a chemical tracer. Rain events in the western equatorial Pacific were identified using particular thresholds for spatial extent, intensity, and duration. The spatial extent threshold is intended to ensure that the rain events are synoptic in scale rather than being associated with mesoscale diurnally forced circulations.

Once rainfall events were identified, we constructed anomaly patterns in the time height plane that help characterize the imprint of convection on the background fields of

mass divergence, cloud top height frequency, and ozone mixing ratio. There has recently been increased recognition of the importance of the layered character of tropical convective outflow [*Thompson et al.*, 1979; *Johnson et al.*, 1999]. The impact of the deep outflow mode can be immediately identified in climatological profiles of divergence, cloud top frequency, and ozone. The impact of the congestus outflow mode on the climatological profiles of divergence and ozone mixing ratio is much less apparent. The effects of the congestus outflow mode on the background distributions of mass and ozone can only be determined through the use of anomaly patterns about high rain events. We have found that the onset of mid-level (3 – 8 km) negative ozone anomalies occurs approximately 16 hours prior to peak rainfall. Modest increases in mid-level cloud top frequency occur over a similar time period, and support the interpretation that the negative mid-level ozone anomalies prior to peak rainfall can be attributed to enhanced detrainment from congestus clouds. The divergence field exhibits a delayed response to the increased frequency of congestus clouds, with a local maximum in mid-level divergence appearing about 8 hours prior to peak rainfall.

In global chemical transport models, the spatial scale of convective clouds is much smaller than the grid scale, so that the convective transport of chemical tracers is parameterized rather than explicitly modeled. The observationally based divergence and ozone anomaly patterns discussed here should provide useful diagnostics for testing the accuracy of this parameterized vertical transport. In agreement with a previous comparison [*Mitovski et al, 2010*], we found the mid-level divergence dipole is poorly represented in two assimilated meteorological datasets. In particular, the two models had difficulty representing the mid-level temporal asymmetry in the divergence field

associated with congestus divergence prior to peak rainfall, and stratiform convergence after peak rainfall.

The ozone anomaly patterns of the GEOS-Chem chemical transport model, when forced by GEOS-4 and GEOS-5 assimilated meteorology, exhibit both mid-level and upper tropospheric negative ozone anomalies. However, the upper tropospheric negative ozone anomalies of the two simulations are much more persistent than in the observations. This difference is probably due to the excessive persistence of the GEOS-4 and GEOS-5 rain events. At mid-levels, the negative ozone anomalies of the GEOS-Chem simulations are roughly symmetric about peak rainfall (t = 0), whereas the observed mid-level ozone anomalies are strongest prior to peak rainfall. This lack of asymmetry in the mid-level ozone response of the two models is probably due to the lack of asymmetry in the mid-level divergence anomalies of the GEOS-4 and GEOS-5 assimilated meteorological datasets.

3.8 ACKNOWLEDGEMENTS

CHAPTER 4. ANOMALY PATTERNS ABOUT STRONG CONVECTIVE EVENTS IN THE TROPICS AND MIDLATITUDES: OBSERVATIONS FROM RADIOSONDES AND SURFACE WEATHER STATIONS

Authors: Toni Mitovski[1] and Ian Folkins[1]

[1]Department of Physics and Atmospheric Science, Dalhousie University, Halifax, NS, Canada

4.1 ABSTRACT

We use 13 years (1998 - 2010) of rainfall estimates from the Tropical Rainfall Measuring Mission (TRMM) 3B42 dataset to identify high rain events located close to radiosonde or surface weather stations. This is done in four regions: the Western Tropical Pacific, Tropical Brazil, Southeast China, and Southeast United States. We then construct composite anomaly patterns of a large number of variables about these high rain events. These variables include temperature, relative humidity, surface pressure, Convective Available Potential Energy (CAPE), geopotential height, mass divergence, relative vorticity, and potential vorticity. One motivation of this analysis is to identify regional differences in the interaction between strong convective events and the background atmosphere. We find, overall, that the changes in meteorological variables which occur during the evolution of strong convective events in mid-latitudes are similar to the changes that occur in the tropics. In mid-latitudes, however, strong convective events are associated with stronger anomalies in surface pressure and geopotential height, and exhibit a warm anomaly in the lower troposphere prior to peak rainfall. In the Southeast

United States, the near surface layer of positive CAPE that occurs prior to high rain events is thicker than in the Western Tropical Pacific. In the two mid-latitude regions, the mid-level PV maximum that develops during the growth stage of high rain events acquires a downward tilt toward the surface during the decay stage, suggesting downward transport toward the surface. A conceptual model previously used to interpret the anomaly patterns of the 2-day equatorial wave [*Haertel and Kiladis*, 2004] is used to interpret the anomaly patterns associated with more general types of high rain events in the tropics.

4.2   INTRODUCTION

With some exceptions [*Cotton et al.*, 1989; *DeMott et al.*, 2007], most observationally based analyses of the anomaly patterns associated with strong convective events have been based on measurements over the tropical oceans. Here, we use routine radiosonde observations to construct composite anomaly patterns of a large number of meteorological variables about high rain events in four regions: the Western Tropical Pacific, Tropical Brazil, the Southeast United States, and Southeast China. This approach enables us to identify regional similarities and differences in the interaction between deep convection and the background atmosphere. The meteorological variables we analyze include temperature, relative humidity, column water vapor, Convective Available Potential Energy (CAPE), geopotential height, mass divergence, surface pressure, relative vorticity, and potential vorticity. We first use the Tropical Rainfall Measuring Missing (TRMM) 3B42 dataset to identify 2x2-degree grid cells in which the rain rate exceeds a particular threshold. We then look for radiosonde or surface measurements that are co-

located, and within 48 hours, of the TRMM high rain events. To obtain better statistics, this procedure is repeated at many radiosonde stations, using a large number of rain events from 1998 to 2010. This approach has been previously followed using routine radiosonde profiles [*Sherwood and Wahrlich*, 1999; *Mitovski et al.*, 2010], measurements from field campaigns [*Sobel et al.*, 2004; *Mapes et al.*, 2006; *DeMott et al.*, 2007; *Mapes et al.*, 2009], satellite data [*Zelinka and Hartmann*, 2009; *Masunaga*, 2012], and re-analysis data [*Benedict and Randall*, 2007; *Rapp et al.*, 2011]. Some of the anomaly patterns shown in this paper, especially with respect to temperature and relative humidity anomaly patterns in the tropics, therefore reproduce well known relationships. However, radiosonde observations have not been used to directly calculate the anomaly patterns of other meteorological variables such as geopotential height and potential vorticity, or the vertical profile of CAPE in the boundary layer.

4.3 DATASETS

4.3.1 RAINFALL DATA

The TRMM 3B42 gridded rainfall dataset is constructed from several satellite borne sensors. These include a precipitation radar, multichannel microwave radiometer, and visible and infrared sensors [*Kummerow et al.*, 1998; *Liu et al.*, 2012]. The data is available at 3-h temporal (centered at 00:00, 03:00, 06:00, 09:00, 12:00, 15:00, 18:00, and 21:00 UTC), and 0.25 x 0.25 degree horizontal resolution. We used TRMM 3B42 rainfall to identify high rain events between Jan 1998 and Dec 2010.

4.3.2 RADIOSONDE DATA

The Integrated Global Radiosonde Archive (IGRA) dataset is stored at the National Climatic Data Center (NCDC) [*Durre at al.*, 2006]. We used data from 53 radiosonde locations from the 1998 – 2010 time period. The locations of these stations are shown as open squares in Figure 4.1, and are located in four regions: 6 from the Western Tropical Pacific, 11 from Tropical Brazil, 19 from the Southeast United States, and 17 from Southeast China. The soundings provide temperature and relative humidity profiles at variable vertical resolution. Within the Southeast United States region, there were on average 42 temperature and relative humidity measurements below 100 hPa. The comparable numbers for the radiosonde stations in the Western Tropical Pacific, Tropical Brazil, and Southeast China regions, are 39, 26, and 14, respectively. The soundings also provide horizontal wind measurements at the surface and at the standard pressure levels of 1000, 925, 850, 700, 500, 400, 300, 250, 200, 150, and 100 hPa. Although some of the IGRA soundings are available every 6 hours, the majority of the soundings are available twice per day at the 00:00 and 12:00 UTC standard synoptic times.
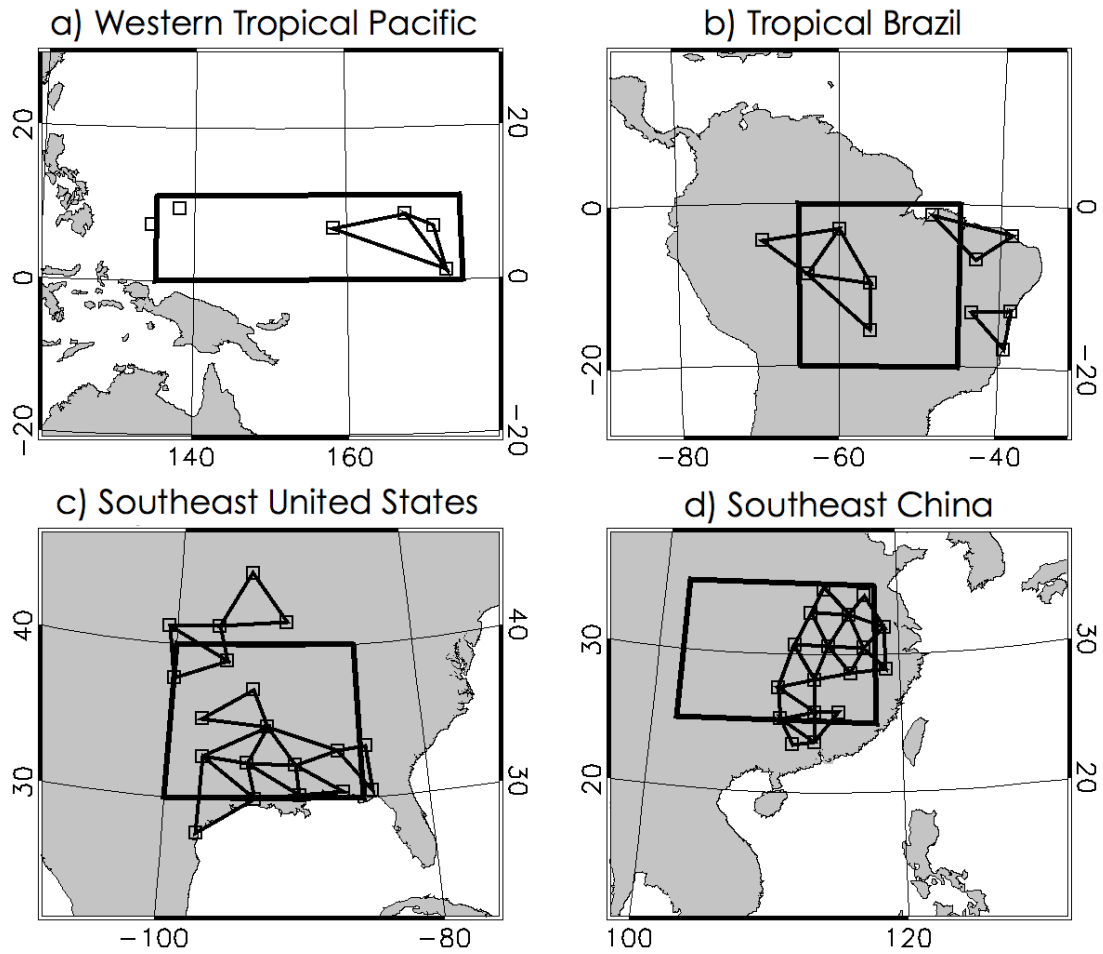
Figure 4.1: Open squares refer to the co-located IGRA radiosonde station and the ISH weather stations used to construct the anomaly patterns. The triangles show the radiosonde arrays used to calculate the mass divergence, relative vorticity, and potential vorticity anomaly patterns. The large rectangles show the regions within which rain events were chosen to calculate the radial variation of temperature about high rain events.

The divergence and vorticity anomaly calculations require simultaneous horizontal wind measurements from triangular radiosonde arrays. For these variables, we used 2 arrays from the Western Tropical Pacific, 5 arrays from Tropical Brazil, 14 arrays from the Southeast United States, and 17 arrays from Southeast China. The average area of the Western Tropical Pacific arrays was 296,000 km^2 (roughly equal to the area of a 5x5-degree grid box at the equator), 57,000 km^2 for the Southeast United States arrays

(roughly equal to a 2.5x2.5-degree grid box at 30°N), 207,000 km^2 for the Tropical Brazil arrays, and 31,000 km^2 for the Southeast China arrays.

4.3.3 HOURLY SURFACE DATA

Over land, convective precipitation usually peaks in the late afternoon [*Nesbitt and Zipser*, 2003]. The rain events used to construct the anomaly patterns over land also occur more frequently in the late afternoon. Within a given region, the radiosonde are usually launched at two fixed local solar times. The incomplete diurnal sampling of the radiosondes, in combination with the existence of diurnal cycles in both the rain event frequency and the meteorological variables, will introduce biases into the calculation of our anomaly patterns. It is therefore important that, where possible, the radiosonde anomaly patterns be validated against surface measurements with better temporal resolution. The Integrated Surface Hourly (ISH) dataset consists of surface weather observations from about 20,000 worldwide-distributed stations [*Lott et al.*, 2001]. The data is archived at the NCDC, and contains hourly and synoptic (3-hourly) surface weather observations of several variables, including temperature, relative humidity, and pressure. We used ISH data between 1998 and 2010, from surface stations, which were co-located with the 53 IGRA radiosonde stations shown in Figure 4.1.

4.3.4 GLOBAL POSITIONING SYSTEM DATA

We used Global Positioning System (GPS) radio occultation temperature measurements from the Constellation Observing System for Meteorology, Ionosphere and Climate (COSMIC) six-satellite constellation [*Anthes et al.*, 2008], downloaded from

the COSMIC Data Analysis and Archive Center (CDAAC). There are approximately 2,000 high-vertical resolution (~100 m in the troposphere) COSMIC temperature profiles over the earth per day. Over a particular region, the COSMIC profiles are distributed roughly uniformly in local solar time. They can therefore also be used to help determine whether the calculated radiosonde temperature anomaly patterns over land exhibit a diurnal bias. We used COSMIC temperature profiles within the Southeast United States (between 30°N and 40°N and between 85°W and 100°W) and Southeast China (between 25°N and 35°N and between 103°E and 118°E) regions shown in Figures 4.1c and 4.1d. For both regions, we restricted attention to the convective summer season (June, July, and August) from 2006 to 2010.

4.4 RAIN EVENT DEFINITION

In the construction of the radiosonde and surface station anomaly patterns, high rain events were considered to occur at locations where the mean TRMM 3B42 rainfall over a 2 by 2 degree box centered at each station exceeded 1.5 mm/h over a TRMM 3-hour time interval. For the calculation of the mass divergence and relative vorticity anomaly patterns, we used triangular radiosonde arrays, and rain events were defined using the average TRMM 3B42 rain rate within each array. For the Southeast United States and Southeast China regions, we restricted attention to June, July, and August. For the tropical Brazil and the Western Tropical Pacific regions, we used rain events from the entire year.

Figure 4.2a shows the composite TRMM 3B42 2x2-degree mean rain event profiles from the four regions. The mean peak rain rate of close to 3 mm/h is significantly higher

than the rain event threshold of 1.5 mm/h. The composite rain event profiles were constructed from events co-located with radiosonde or surface stations, rather than from rain events within the variably sized radiosonde arrays. The rain event profiles are quite similar to each other, partly reflecting the use of a common rain event threshold for all regions. High rain events develop slightly more rapidly over the three land regions than the Tropical Western Pacific. Rainfall starts to increase roughly 9 hours prior to peak rainfall and drops to near background levels roughly 9 hours after peak rainfall.
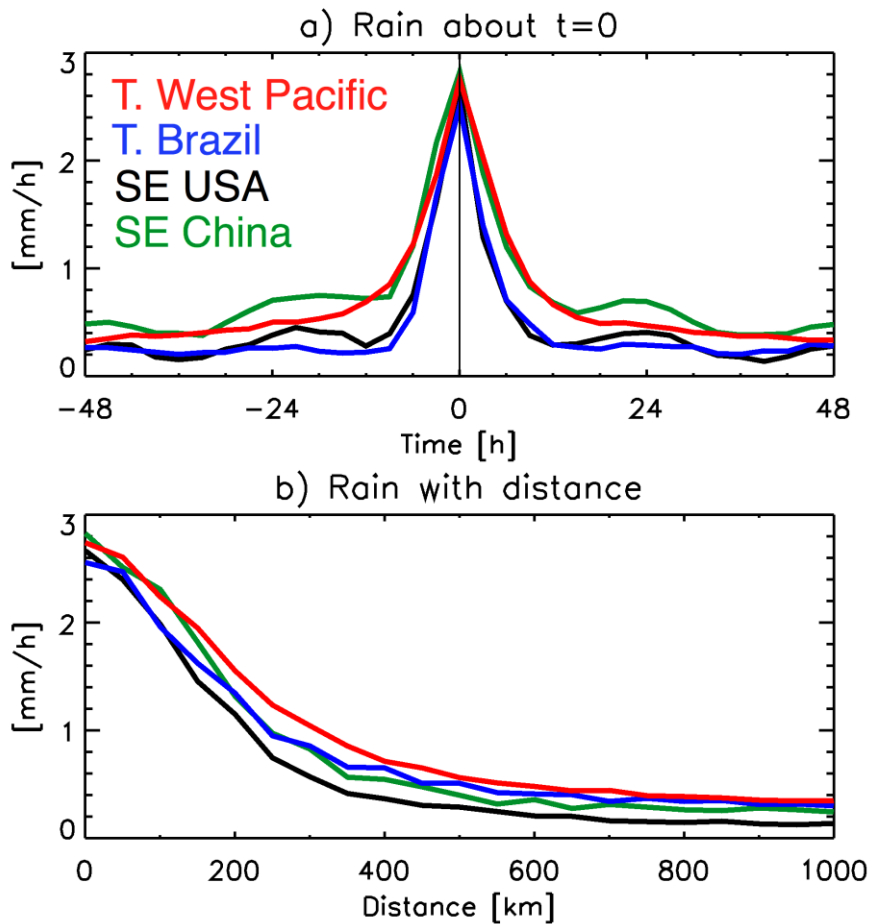
Figure 4.2: (a) The variation in mean rainfall during the growth and decay of the TRMM 3B42 2x2-degree high rain events within each region. (b) The radial variation in mean rainfall about the high rain events.

Within a particular region, the GPS COSMIC temperature profiles tend to be randomly distributed in space. In order to identify high rain events co-located with GPS temperature profiles, we first calculated the mean TRMM 3B42 rain rate in 2x2-degree grid boxes, separated from each other by 1 degree. For example, the Southeast United States region shown in Figure 4.1c enclosed an area between 30°- 40°N and 85°- 100°W. Within this region, we calculated the mean rain rate in 10 x 15 = 150 overlapping 2x2-degree grid boxes, and searched for GPS temperature profiles within each box. The Southeast China region shown in Figure 4.1d enclosed an area between 25°- 35°N and 103°- 118°E, and was also partitioned into 150 overlapping boxes.

Figure 4.2b shows the variation in average rain rate as a function of radial distance from the high rain events. The rain events of the various regions have a similar spatial scale, with the rain rate typically decaying to a near background value within about 400 km of peak rainfall.

4.5 DIURNAL VARIABILITY

Figure 4.3a shows the average diurnal variation of the TRMM 3B42 rain rate within each of the four regions. As is well known [*Nesbitt and Zipser*, 2003], the rainfall rate within the three land regions peaks in the late afternoon or early evening. Within the Tropical Western Pacific region, the rainfall rate exhibits a small peak near 3 am. Figure 4.3b shows the diurnal variation in the frequency of occurrence of the rain events used to construct the radiosonde temperature anomaly patterns. The time of the diurnal peak in the rain event frequency is usually close to the time of the diurnal rainfall peak. The larger number of rain events within the Tropical Brazil region, despite the lower rain rate,

is due to the use of rain events throughout the entire year, rather than June – August for the two mid-latitude regions.
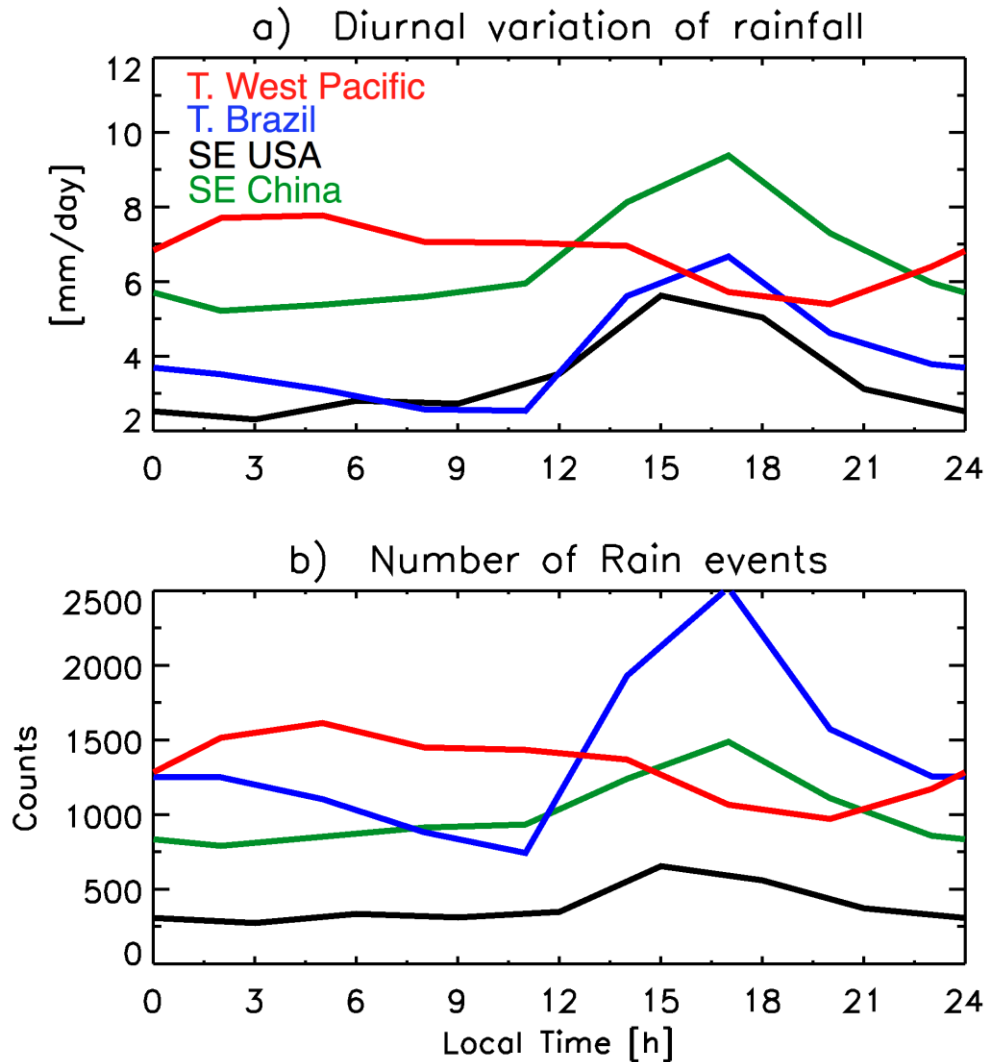
Figure 4.3: (a) The variation in TRMM 3B42 2x2-degree rainfall with local solar time, averaged over the radiosonde locations of each region shown in Figure 4.1. (b) The diurnal variation in the number of high rain events within each 3-hour time bin, calculated from all rain events used in the construction of the temperature anomaly patterns.

Figure 4.4 shows the number of IGRA radiosonde profiles within each region that occurred within 48 hours of a rain event, and could therefore be used in the construction of the temperature anomaly patterns. Within the Southeast United States, there were

approximately 21,000 profiles at 06 and 18 h local solar time available from the 1998 –
2010 time period. We used 25,000 profiles from Tropical Brazil (08 and 20 h local solar
time), 55,000 profiles from Southeast China (also at 08 and 20 h local solar time), and
roughly 80,000 soundings from the Tropical Western Pacific, distributed at local solar
times of 00, 09, 10, 11, 12, 21, 22, and 23 h. The broader range of local solar times from
the Tropical Western Pacific reflects the broader longitudinal distribution of the
radiosonde stations in this region.
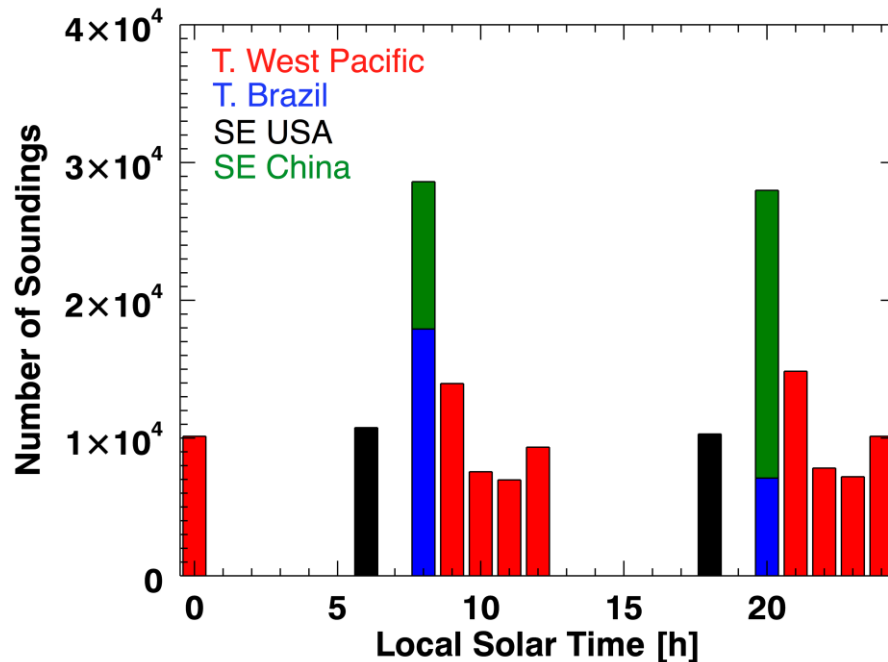
Figure 4.4: The number of available soundings, at each local solar time, within 48 hours
of the rainfall events used in the construction of the temperature anomaly patterns.
Different colors refer to different regions.

4.6 RESULTS

4.6.1 TEMPERATURE ANOMALY PATTERNS FROM RADIOSONDES

Once a rain event at a radiosonde station had been identified, we searched for radiosonde launches that had occurred within 48 hours of the rain event. These soundings were then assigned to 3-h time bins, based on the difference between the radiosonde launch and rain event times. At each location, the radiosonde measurements were used to define climatological temperature profiles for each individual launch time, month, and year. These climatological profiles were then used to convert the temperature profiles near high rain events to temperature anomaly profiles. We then averaged the temperature anomaly profiles within each 3-h time bin.

The composite temperature anomaly patterns generated using the above procedure within each region are shown in Figure 4.5a, 4.5b, 4.5c, and 4.5e. For all regions, high rain events are associated with an upper-level warming centered at 300 hPa that is coincident with peak rainfall [*Cotton et al.*, 1989; *Sherwood and Wahrlich*, 1999; *Kiladis et al.*, 2005; *Mapes et al.*, 2006; *Mitovski et al.*, 2010]. With exception of Southeast China, the regions also show a 700 hPa lower tropospheric cooling coincident with peak rainfall. Each region shows a strong boundary layer cooling (below 900 hPa) after peak rainfall. This cooling is significantly larger and more persistent over the three land regions than over the Tropical Western Pacific. Deep convection over the three land regions is preceded by a warm anomaly in the lower troposphere. Over Tropical Brazil and Southeast China, this warming extends upward from the surface to 800 hPa, but extends to 600 hPa over the Southeast United States.

The details of the temperature anomaly patterns shown in Figure 4.5a, 4.5b, 4.5c, and 4.5e will be sensitive, to some degree, to the assumptions used to define the rain events. For example, the use of a larger rain event threshold would be expected to generate larger temperature anomalies. It has been shown, however, that the shapes of the temperature anomaly patterns are not sensitive to the value of the rain event threshold or the assumed event area [*Mitovski et al.*, 2010].
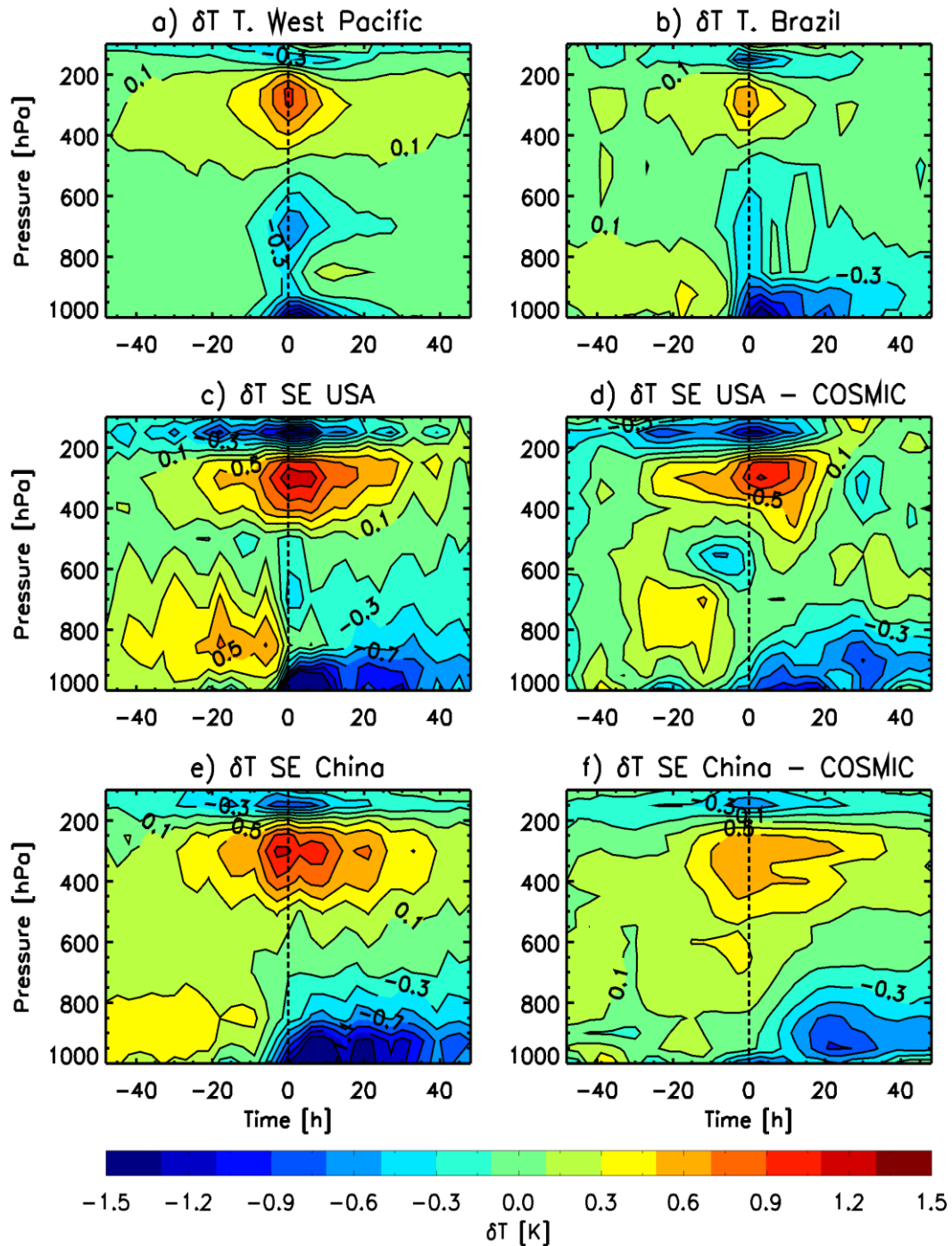
Figure 4.5: (a), (b), (c), and (e) show temperature anomaly patterns about the TRMM high rain events, calculated using IGRA radiosonde profiles from each region. (d) and (f) show temperature anomaly patterns calculated using the COSMIC GPS temperature profiles.

4.6.2 TEMPERATURE ANOMALY PATTERNS FROM GPS

The GPS COSMIC temperature profiles were used to also construct temperature anomaly patterns of the Southeast United States and Southeast China regions. During the summer convective season (JJA) between 2006 and 2010, there were 2,111 profiles from the United States, and 1,538 profiles from China, which were co-located within 48 hours of a TRMM rain event. The COSMIC temperature anomaly patterns from these two regions are shown in Figure 4.5d and 4.5f. Although the COSMIC and radiosonde temperature anomaly patterns are in good overall agreement, the COSMIC boundary layer cooling is much smaller than the boundary layer cooling obtained from the radiosonde data. There are several reasons why the COSMIC temperature anomaly patterns may be less accurate near the surface. COSMIC provides vertical profiles of atmospheric refractivity, which can be used to calculate the vertical profile of atmospheric density [*Anthes et al*., 2008]. Variations in water vapor can be expected to more strongly affect the atmospheric density at higher temperatures closer to the surface. In the absence of an independent method of constraining the water vapor profile, the relative accuracy of the COSMIC temperature retrievals can be expected to be smaller at lower altitudes. The standard deviation of the difference between COSMIC and radiosonde temperatures does increase toward the surface, though this does not appear to be associated with an increase in the mean bias [*Sun et al.*, 2010]. The refractivity gradient at the top of the boundary layer frequently exceeds the critical refraction, which can result in a systematic negative refractivity bias in the radio occultations within the boundary layer [*Xie et al*., 2012]. Finally, the number of COSMIC temperature retrievals decreases toward the surface, especially for altitudes below 2 km [*Anthes et al*., 2008].

4.6.3 ANOMALIES IN PRESSURE, TEMPERATURE, AND RELATIVE HUMIDITY AT THE SURFACE

Figure 4.6 shows the surface temperature, surface relative humidity, and surface pressure anomalies during high rain events within each of the four regions, calculated from both the radiosonde and surface weather station data. In general, the radiosonde anomaly profiles (solid lines) are in good agreement with the profiles generated by higher temporal resolution surface station measurements (dotted lines).

The top row of Figure 4.6 shows the surface temperature anomaly during high rain events. The three land regions show larger surface cooling than the Tropical West Pacific region. This is consistent with Figure 4.5, which also shows that the boundary layer cooling over land exhibits greater persistence and depth. One explanation for this difference is that the relative humidity in the lower troposphere over the three land regions tends to be smaller than the relative humidity in the lower troposphere over the ocean region. Downdrafts over land would therefore be expected to exhibit stronger negative buoyancies, have a higher probability of penetrating the boundary layer, and possibly, generate more persistent cooling. It is also possible that, due to a weaker effective heat capacity over land, the sensible heat flux from the surface in response to a cold anomaly near the ground is likely to be weaker over land than the ocean. In addition to these possibilities, the warm anomaly in the lower troposphere just before peak rainfall may in part arise from the tendency for heavy rain events to form in the warm sectors, just ahead of the cold front, of midlatitude low-pressure systems. The warm anomaly may also arise from the fact that convection is most frequent during the afternoon, when the

solar heating is strongest. The cold anomaly following the precipitation, which is deeper and more persistent over land than over the Tropical Ocean, could be affected by nocturnal cooling and the tendency for cold fronts to cross the region after heavy rainfall ends.

The middle row of Figure 4.6 shows the anomaly in surface relative humidity during high rain events. Within all four regions, convective rainfall is associated with a sharp increase in surface relative humidity that is coincident, or slightly lags, peak rainfall. As would be expected, the size of the relative humidity increase scales with the size of the temperature decrease, with the two mid-latitude land regions exhibiting the largest increases in surface relative humidity.
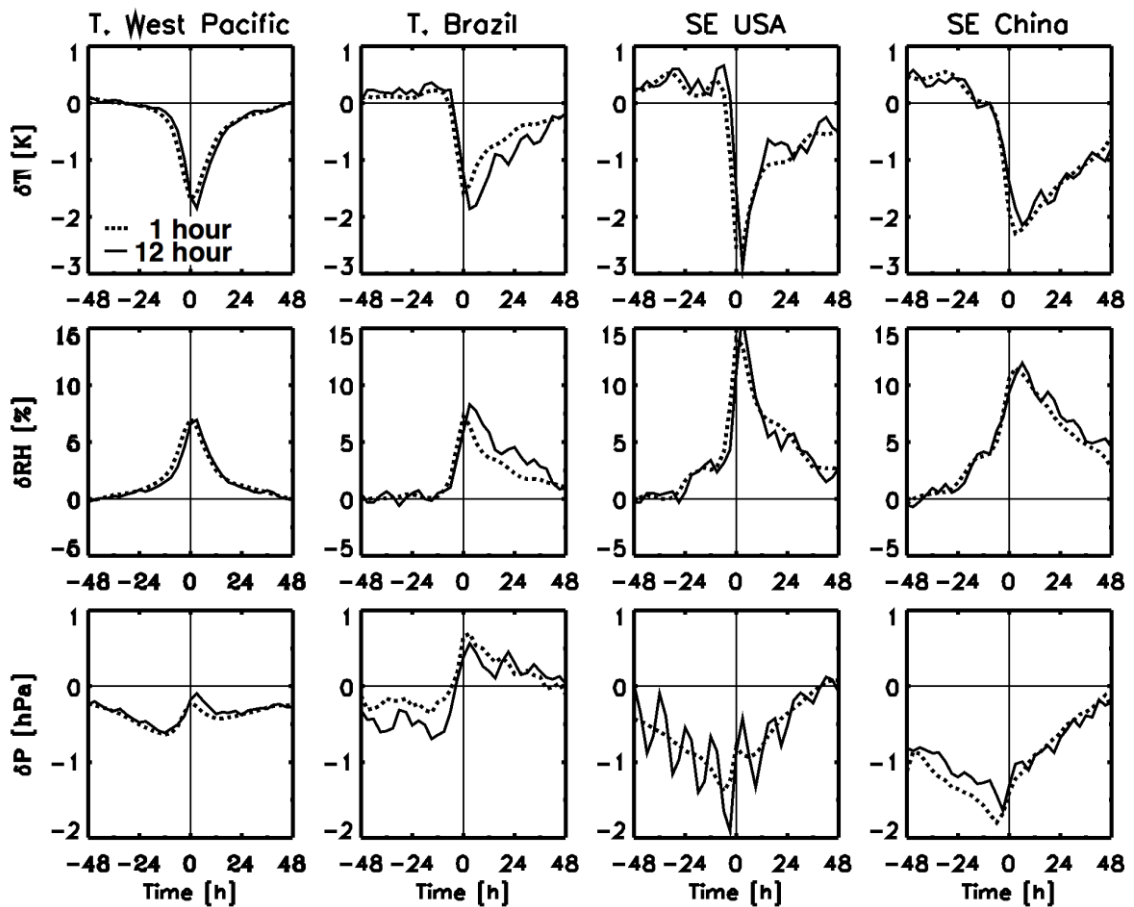
Figure 4.6: Within each figure, the dotted line refers to an anomaly profile calculated using 1-h ISH surface data, while the solid lines refer to anomaly profiles calculated using 12-h IGRA radiosonde data. (upper row) The variation of the surface temperature anomaly during high rain events. (middle row) The variation of surface relative humidity anomaly during high rain events. (bottom row) The variation in the surface pressure anomaly during high rain events. Each column refers to a different region with from left to right: the Tropical Western Pacific, Tropical Brazil, Southeast USA, and Southeast China regions.

The bottom row of Figure 4.6 shows the surface pressure anomalies during high rain events. These anomalies show larger regional differences than the temperature and relative humidity anomalies. In the Western Tropical Pacific, there is a 0.5 hPa minimum in surface pressure 10 hours prior to peak rainfall, followed by a small local maximum that slightly lags peak rainfall. In the Tropical Brazil region, there is a more rapid increase in surface pressure during high rain events. In the two mid-latitude regions, high rain events are associated with 1-2 hPa reductions in surface pressure over a 2-3 day timescale.

The surface pressure anomalies of the radiosonde stations within the Southeast United States, and to a lesser extent within Southeast China and Tropical Brazil, are significantly different from the surface pressure anomalies obtained from the surface stations. These deviations have a 12-hour periodicity. The black curve in Figure 4.7a shows the average diurnal cycle of the surface pressure anomaly for the Southeast United States surface stations. The red curve shows the diurnal cycle of the surface pressure anomaly, calculated using only those surface pressure measurements for which the rain rate of the local grid cell exceeded 1 mm/h. During the afternoon (14:00 − 18:00 local time), the presence of rainfall is not associated with deviations in surface pressure from the mean diurnal cycle. However, outside this afternoon and early evening time window,

93

rainfall is associated with reduced surface pressure. Figure 4.7c shows that the surface pressure anomaly during high rain events depends on the time at which the rain event occurs. Each anomaly curve is constructed from high rain events having a common TRMM time, converted here to the approximate local solar time. The three curves with the largest negative anomalies in surface pressure are associated with rain events at 21:00 (solid green curve), 00:00 (solid blue curve), and 03:00 (solid red curve). The two anomaly curves with the smallest negative anomalies in surface pressure are associated with rain events which occur at 15:00 (dashed red curve) and 18:00 (solid black curve). This is consistent with Figure 4.7a. Rain events which occur during the late evening and early morning are associated with larger decreases in surface pressure (relative to the mean surface pressure at that local time) than rain events in the late afternoon.

a) Diurnal δPs

b) δPs about 0-24 rain events

c) δPs about 3-h rain events

95
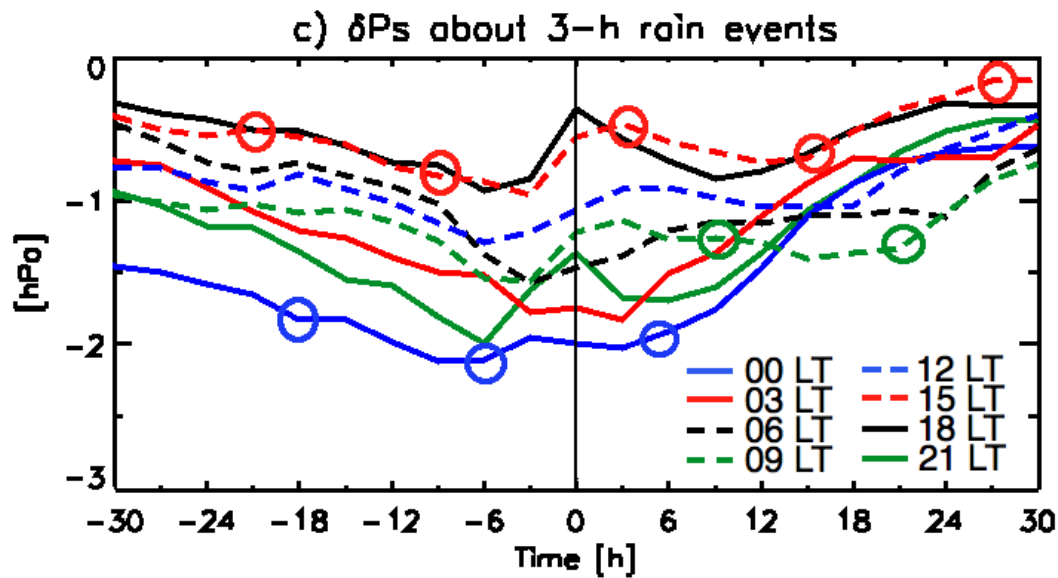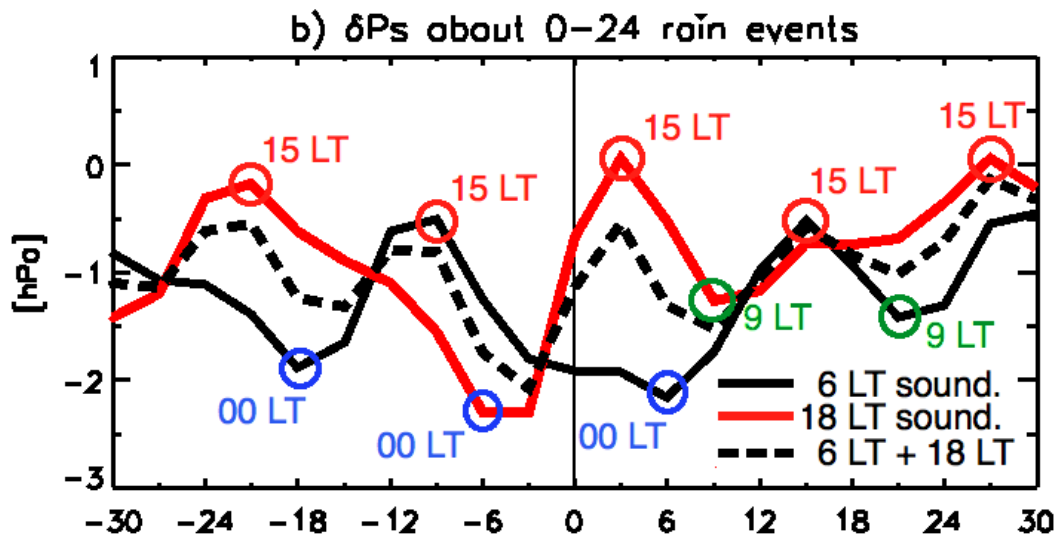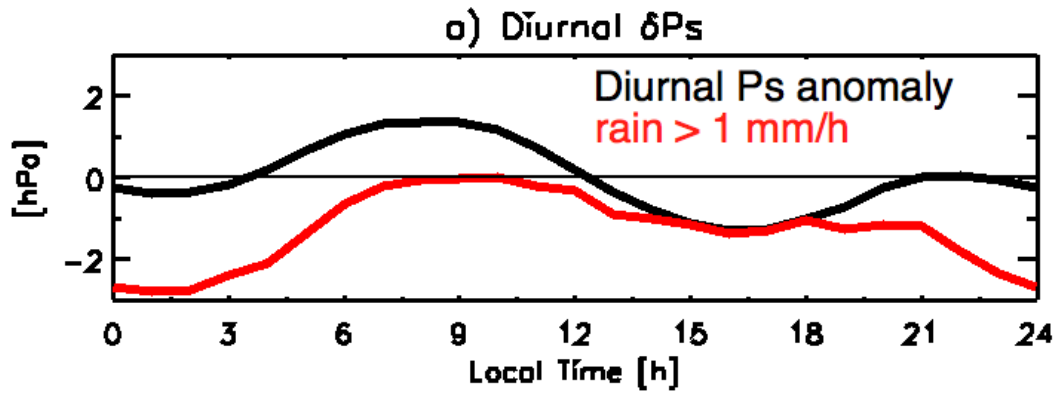
Figure 4.7: (a) The black curve of the top panel shows the diurnal variation in the surface pressure anomaly, plotted against local solar time, of the surface stations within the Southeast United States region shown in Figure 4.1 (June, July, and August). The red curve was obtained from the subset of surface pressure measurements at which the local rain rate of each surface station exceeded 1.0 mm/h; (b) The solid black curve shows the surface pressure anomaly about high rain events constructed using radiosonde measurements launched at 6 LT only. The red curve shows the surface pressure anomaly about high rain constructed from radiosonde measurements at 18 LT only. The black dashed line shows the combined surface pressure anomaly of the two radiosonde launch times. (c) Each curve shows the surface pressure response, calculated using ISH surface station data within the Southeast United States region, to TRMM rain events occurring at a particular time. For each curve, the local time of the TRMM rain events is shown in the legend. The circles in the middle panel indicate the local time of the rain events about which the pressure anomaly was calculated. For example, the red circles of the middle panel indicate surface pressure anomalies calculated from radiosondes launched at 18 LT, from rain events at 15 LT. Each red circle of the middle panel corresponds to a red circle in the lower panel, which indicates the effect of rain occurring events at that time on the surface pressure anomaly. In general, maxima in the curves of the middle panel occur at times when the corresponding rain events are associated with a smaller surface pressure anomaly, and vice versa.

The existence of a diurnal cycle in the magnitude of the surface pressure anomaly associated with high rain events leads to errors when the twice daily radiosonde profiles are used to construct the surface pressure anomaly patterns. The twice daily radiosonde launches occur at local solar times of 6 and 18 h. Figure 4.7b shows the surface pressure anomaly constructed from the individual sondes, as well as the combined response shown previously in Figure 4.6. For the two individual anomalies, there is a 24 h oscillation generated by changes in the local solar time of the rain events. For example, the curve generated using the 6 local time (LT) radiosonde launches and the curve generated using the 18 LT radiosonde launches both show maxima associated with rain events occurring at 15 LT, and minima associated with rain events occurring at 00 LT. The anomaly pattern is consistent with Figure 4.7c, which shows weaker surface pressure anomalies for rain events in the late afternoon, and stronger surface pressure anomalies for rain

events at night. The combined radiosonde surface pressure anomaly profile in Figure 4.7b, indicated by the dashed line, is equal to the average of the two individual radiosonde profiles, weighted by the relative frequency of the rain events used to construct the two profiles. Inspection of Figure 4.7b shows that the 12-hour oscillation in the combined radiosonde surface pressure anomaly pattern is an artifact generated from the 24-hour oscillations of the two individual curves. More generally, for variables which exhibit a coupling with convective precipitation which varies over the diurnal cycle, artifacts may be introduced when using 12 hourly radiosonde profiles to construct anomaly patterns in that variable.

4.6.4 RADIAL DISTRIBUTION OF THE CONVECTIVE TEMPERATURE RESPONSE

The temperature anomaly patterns shown in Figure 4.5 show the time evolution of the local temperature response to deep convection, but give no indication of the spatial scale over which these temperature anomalies extend. The radiosonde measurements can be used to calculate the vertical profile of the temperature anomaly as a function of the radial distance from the rain events. We first identified all 2x2-degree rain events within each of the regional boxes shown in Figure 4.1, and then searched for radiosonde measurements within 1000 km of the rain event which had occurred within 3 hours of the rain event time. The radiosonde temperature profiles were then stored in 50 km bins, based on the distance between the rain event and the radiosonde location. Each temperature profile was converted to an instantaneous anomaly profile by subtracting the climatological launch-time/monthly/yearly temperature profile at that location. The

temperature anomaly profiles within each 50-km bin at each pressure level were then averaged, and the results shown in Figure 4.8.
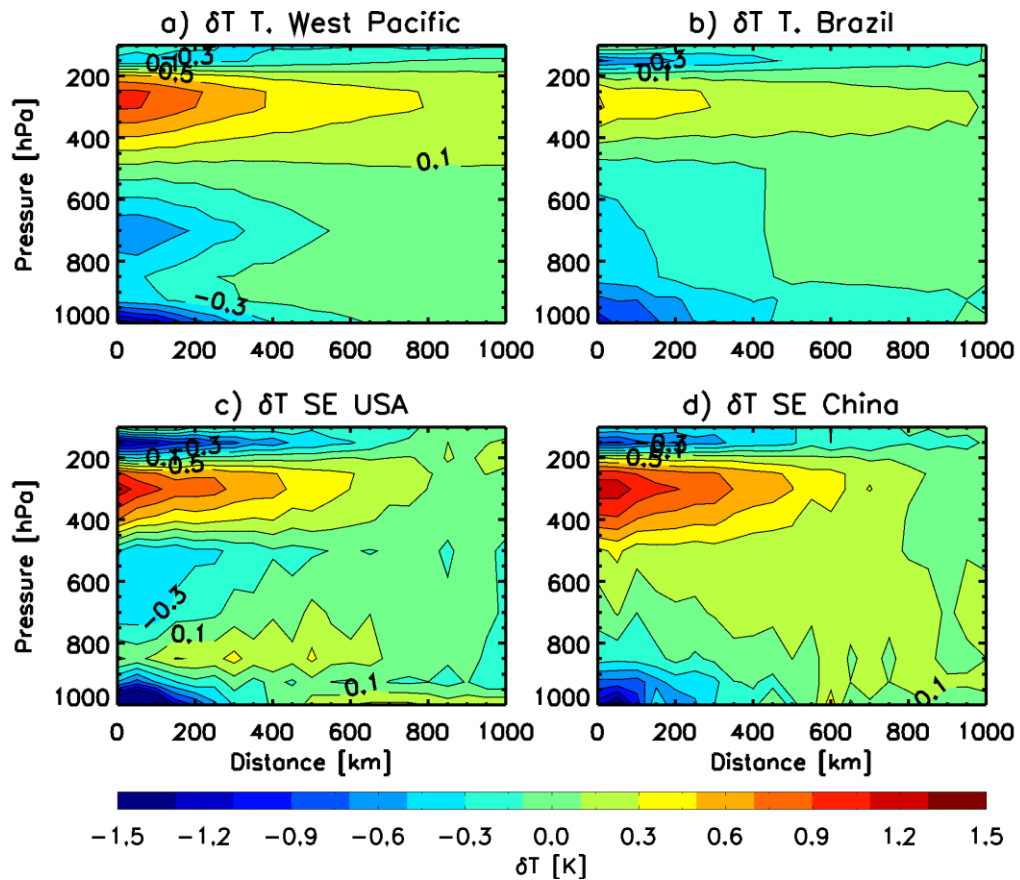
Figure 4.8: The radial distribution of the temperature anomaly about high rain events in each region. The horizontal axis refers to the radial distance between a radiosonde location and a TRMM high rain event. The patterns were constructed from radiosonde launches within 3 h of a TRMM rain event.

The dominant feature of the radial temperature anomaly pattern is an upper level (300 hPa) warming that extends roughly 1000 km outward from the rain event. All four regions also exhibit a strong near surface (below 900 hPa) cooling that extends roughly 300 km outward from the rain event. The Western Tropical Pacific Ocean and Southeast United States regions also exhibit a strong lower tropospheric cooling between 800 hPa and 500 hPa. This lower tropospheric cooling is less pronounced over Tropical Brazil,

and absent over Southeast China. The regional differences in the local convective temperature response shown in Figure 4.5 are therefore not restricted to the immediate environment of deep convective events, but extend to larger spatial scales.

4.6.5 RELATIVE HUMIDITY

The IGRA radiosonde dataset supplies vertical profiles of water vapor pressure, which can be converted to relative humidity. At temperatures below 0 °C, we normalized the vapor pressure by the saturation vapor pressure over ice [*Emanuel*, 1994]. In general, radiosonde measurements of vapor pressure are less accurate at colder temperatures [*Kley et al.*, 2000]. The relative humidity was therefore not calculated for pressure levels above 200 hPa. Figure 4.9 shows the relative humidity response to high rain events, calculated using a procedure similar to that used for the temperature anomaly patterns. Within each region, peak rainfall is associated with values of relative humidity that exceed 80 % at most altitudes. The gradual moistening of the lower troposphere prior to high rain events has been attributed to the influence of congestus clouds [*Takayabu et al.*, 1996; *Mapes et al.*, 2006], but this interpretation has been recently challenged [*Hohenegger and Stevens*, 2013; *Masunaga*, 2013]. Rain events within the Southeast United States occur within a background atmosphere that is significantly drier than the other three regions, particularly in the upper troposphere.
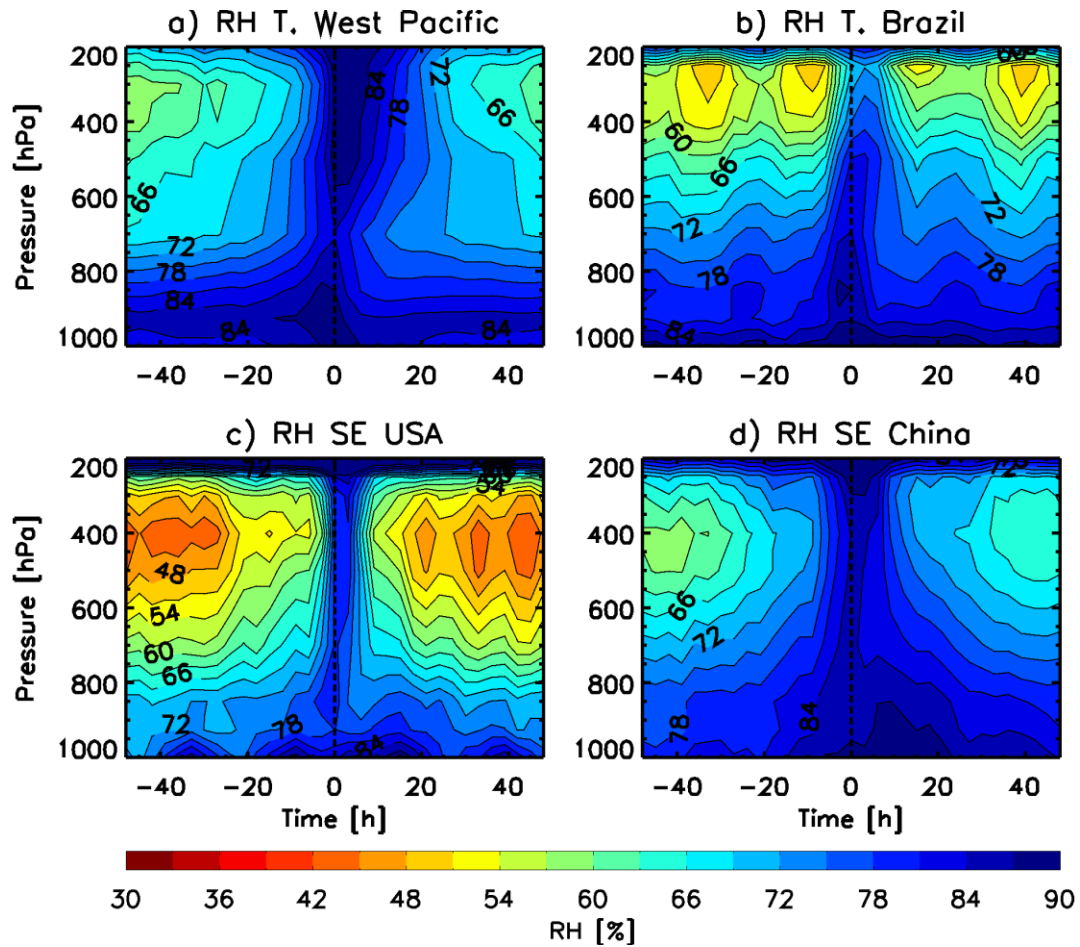
Figure 4.9: The variation in relative humidity during the evolution of high rain events in each region. The horizontal axis refers to time since peak rainfall.

4.6.6 TOTAL COLUMN WATER VAPOR ANOMALY

The relative humidity and temperature measurements of the radiosonde profiles can be used to calculate the total column water vapor, defined here as the mass of water vapor per unit area between the surface and 200 hPa (also known as the precipitable water). Figure 4.10 shows the column water vapor anomaly during the growth and decay of high rain events within each region. Rain events in the Southeast United States occur at much lower values of column water than the other three regions (not shown). However, the change in column water during high rain events in the Southeast United States is very

similar to the change in Southeast China and the Western Tropical Pacific (7-10 kg/m^2). Rain events in Tropical Brazil are associated with smaller increases in column water (less than 4 kg/m^2).
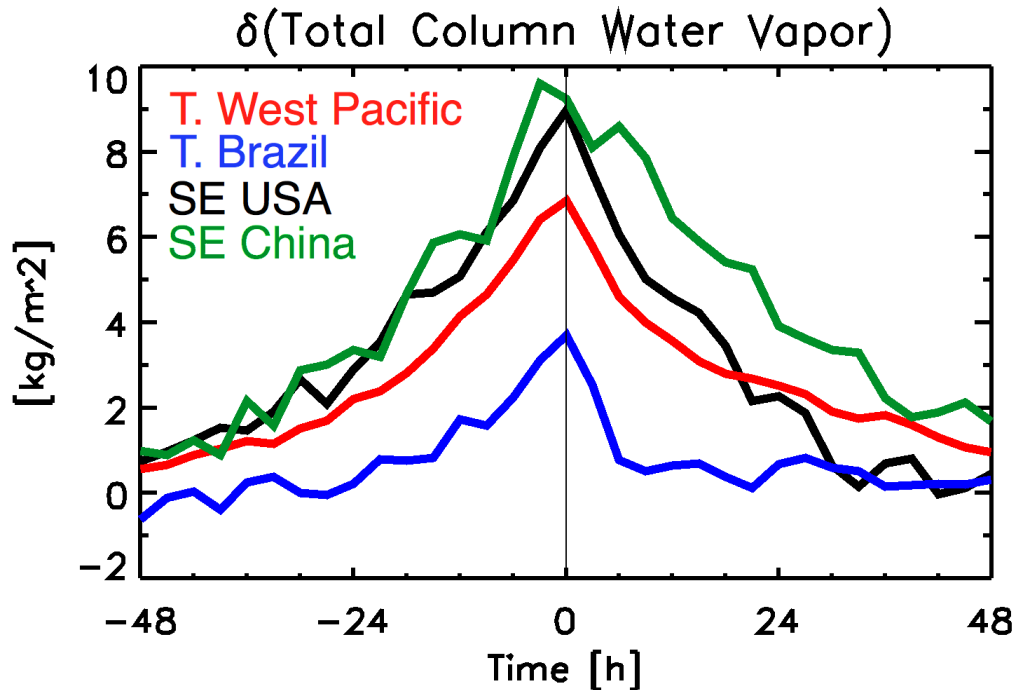
Figure 4.10: The variation of the total column water vapor anomaly about high rain events in each region. The total column water vapor anomaly is a mass weighted vertical integral of the specific humidity anomaly between 1000 and 200 hPa, as measured by a radiosonde profile.

4.6.7 CONVECTIVE AVAILABLE POTENTIAL ENERGY

The existence of air parcels near the surface with positive Convective Available Potential Energy (CAPE) is a precondition for moist convection [*Sherwood and Wahrlich*, 1999]. We calculate CAPE by starting with air parcels near the surface whose pressure, temperature, and relative humidity are equal to the values given by a radiosonde profile at a particular pressure level. We lift the air parcel subject to the assumptions of constant moist static energy and total water (i.e. no condensate removal), no mixing, and

no ice formation. Unfortunately, only the radiosonde profiles of the Western Tropical Pacific and Southeast United States regions had sufficient vertical resolution to resolve the vertical structure of boundary layer CAPE.

The evolution of CAPE and the CAPE anomaly during the growth and decay of high rain events within these two regions is shown in Figure 4.11. In both regions, the decay stages of high rain events are associated with strongly negative CAPE anomalies which maximize near the surface several hours after peak rainfall. This CAPE reduction is presumably associated with some combination of preferential entrainment of higher moist static energy air parcels from the boundary layer by convective updrafts and by the injection of lower moist static energy air into the boundary layer from the mid-troposphere [*Zipser*, 1977; *Sherwood and Wahrlich*, 1999].

Figure 4.11 also shows that the near surface layer of positive CAPE is considerably thicker in the Southeast United States region than in the Western Tropical Pacific. Model simulations suggest that convective storms which grow from a deeper near surface moist layer, especially in the range of 1.5 – 2 km, can experience significantly less updraft dilution and develop stronger updraft speeds than those which grow from thinner moist layers [*McCaul and Cohen*, 2002]. In this case, Figure 4.11 may partially explain the well known fact that convective updrafts which occur over the ocean exhibit smaller updraft speeds than those which occur over land [*Lucas et al.*, 1994], though other factors are probably also involved [*Robinson et al.*, 2008].
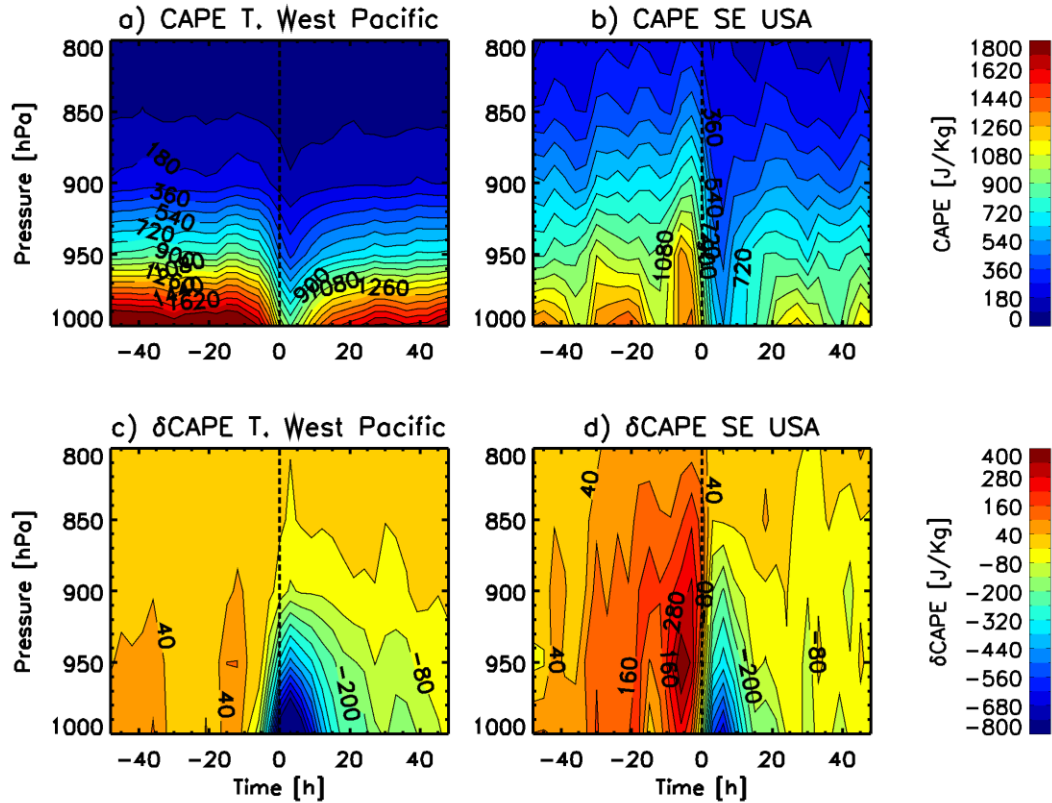
Figure 4.11: Panels (a) and (b) show the variation in boundary layer CAPE during high rain events in the Western Tropical Pacific and Southeast United States regions. The horizontal axis refers to time since peak rainfall. Panels (c) and (d) are similar to the upper panels, but show the CAPE anomaly.

Due to the diurnal cycle in CAPE over land [*Dai et al*., 1999], and the higher frequency of rain events during the late afternoon, some of the CAPE enhancement within the Southeast United States shown in Figure 4.11b prior to peak rainfall can be attributed to the diurnal cycle. The CAPE anomaly, in which the diurnal effect has been reduced by subtracting from each CAPE measurement the mean value of CAPE for each particular radiosonde launch time, station, and month is shown in Figures 4.11c and 4.11d. Within the Western Tropical Pacific, there is very little change in CAPE prior to peak rainfall. Within the Southeast United States, the largest positive CAPE anomaly (~

600 J/kg) occurs for parcels originating from 950 hPa roughly 6 hours prior to peak rainfall.

Figure 4.11 also shows that there is a 12-hour oscillation in the Southeast United States CAPE and CAPE anomaly patterns that mainly occurs prior to peak rainfall. This oscillation is an artifact generated by the same mechanism that produces the surface pressure oscillation shown in Figure 4.7. Although the top panel of Figure 4.6 shows that the surface temperature errors in the Southeast United States introduced by this sampling bias are small, these errors have a larger relative impact on CAPE.

4.6.8 GEOPOTENTIAL HEIGHT

Geopotential height profiles were calculated from the surface pressure, and temperature and relative humidity profiles of individual radiosondes. The geopotential height at the surface of each location was set equal to the local surface station altitude. We used stations whose altitude was less than 200 m. We then iteratively calculated the geopotential height upward from the surface using the hypsometric equation. This equation defines the geopotential height (GPHT) at a pressure level n (p_n) in terms of the geopotential height at a lower pressure level n-1 (p_{n-1}), the virtual temperature at levels n-1 ($T_{v,n-1}$) and n ($T_{v,n}$), and the pressure thickness dp.

$$GPHT_n = GPHT_{n-1} + R_d \left(\frac{T_{v,n-1} + T_{v,n}}{2g} \right) d \ln p. \qquad (4.1)$$

In this equation, p refers to pressure in Pascals, R_d to the specific gas constant of dry air (287.04 $Jkg^{-1}K^{-1}$), T_v to the virtual temperature of an air parcel, and g to standard gravity (9.806 ms^{-2}), and dlnp is defined as

$$d\ln p = \frac{p_{n-1} - p_n}{0.5(p_{n-1} + p_n)}.$$ (4.2)

To obtain the geopotential height anomaly, we subtracted from each geopotential height the mean geopotential height for that station, month, and radiosonde launch time. We then grouped the resulting geopotential height anomaly profiles of each region in 3-hour time bins about their respective rain events. Figure 4.12 shows the geopotential height anomaly patterns associated with the high rain events of each region. The anomaly pattern of the Southeast Unites States exhibits a 12 hour oscillation. This oscillation is stronger in the lower troposphere, and can be attributed to the 12 hour oscillation in lower tropospheric surface pressure discussed earlier.

The geopotential height anomaly patterns of the four regions show some common features. Each region shows a strong positive geopotential height anomaly in the upper troposphere centered at 200 hPa. This anomaly is generated mainly by the upper tropospheric 300 hPa warm anomaly shown in Figure 4.5. Figure 4.12 also shows that the positive upper tropospheric geopotential height anomalies within each region rapidly decrease above 200 hPa. This decrease with height can be attributed to the intense narrow cold anomalies centered near 150 hPa shown in Figures 4.5 and 4.8, which prevent the positive upper tropospheric geopotential height anomalies associated with strong convective events from penetrating into the lower stratosphere [*Holloway and Neelin*, 2007].

In the two tropical regions, the negative mid-level geopotential anomaly is largest at 500 hPa, and roughly symmetric about peak rainfall. The onset of negative geopotential height anomalies in the lower tropospheric begins prior to the lower tropospheric cooling shown in Figure 4.5a, and can be mainly attributed to local

105

reductions in surface pressure. For example, the lower left panel of Figure 4.6 shows that the surface pressure of the Western Tropical Pacific region decreases by roughly 0.6 hPa prior to peak rainfall. This would generate a geopotential height decrease of roughly 5.2 m, comparable with the lower tropospheric geopotential height anomalies prior to peak rainfall shown in Figure 4.12a.

Figure 4.12: The variation in geopotential height (GPHT) during high rain events in each region. The horizontal axis refers to time since peak rainfall.

In the two mid-latitude regions, negative surface pressure anomalies several days prior to peak rainfall contribute to negative geopotential height anomalies in the boundary layer. As peak rain rates develop, the cold anomalies in the boundary layer and mid-

106

levels contribute to the intensification and upward extension of these negative geopotential height anomalies to 400 hPa. These negative mid-level geopotential height anomalies are much stronger, deeper, and more persistent than those observed in the tropics.

4.6.9 MASS DIVERGENCE

At a given pressure level, the net horizontal mass inflow or outflow from a convecting region can be estimated using horizontal wind measurements from radiosonde arrays. We calculated the mass divergence of the triangular arrays shown in Figure 4.1 using the following expression.

$$\nabla \cdot \vec{V} = \sum \frac{\vec{V} \cdot \vec{n} dl}{A} \tag{4.3}$$

$V \cdot \vec{n}$ refers to the wind component normal with respect to a line that connects two points of the array, dl to the distance between the two points, and A to the surface area of the array.

The number of divergence profiles available to construct the anomaly patterns is usually much less than the number of available temperature or relative humidity profiles, partly because a divergence calculation require a complete ring of simultaneous horizontal wind measurements. The native resolution TRMM 3B42 dataset was used to calculate the average rainfall rate within the arrays shown in Figure 4.1. The rain event frequency is in general smaller for larger arrays. On average, there were 164 divergence profiles available per 3 h time bin from the two arrays in the Western Tropical Pacific, 205 profiles from the 14 arrays in the Southeast United States, 414 profiles from the 17 arrays in the Southeast China, and 102 profiles from the 5 arrays in the Equatorial Brazil.

Figure 4.13 shows the divergence anomaly patterns of each region. The four patterns are quite similar. The dominant feature of each pattern is a strong divergence maximum in the upper troposphere (200 hPa). This divergence maximum occurs near peak rainfall, but in three of the regions shows a tendency for stronger persistence after peak rainfall. Each region also shows a strong convergence feature in the boundary layer prior to peak rainfall, extending from the surface to 800 hPa. In the Western Tropical Pacific, this feature occurs 6 hours prior to peak rainfall. For rain events within the three land regions, the time difference between the boundary layer divergence maximum and peak rainfall is roughly equal to 3 hours.

The divergence anomaly pattern of the Western Tropical Pacific region shown in Figure 4.13 exhibits an antisymmetric mid-level divergence dipole about peak rainfall [*Thompson et al.*, 1979; *Mapes et al.*, 2006; *Mapes et al.*, 2009; *Mitovski et al.*, 2010]. Within the three land regions, there is also a tendency for mid-level divergence to occur prior to peak rainfall and mid-level convergence to occur after peak rainfall. However, the timing of these divergence features is closer to peak rainfall than in the Western Tropical Pacific.
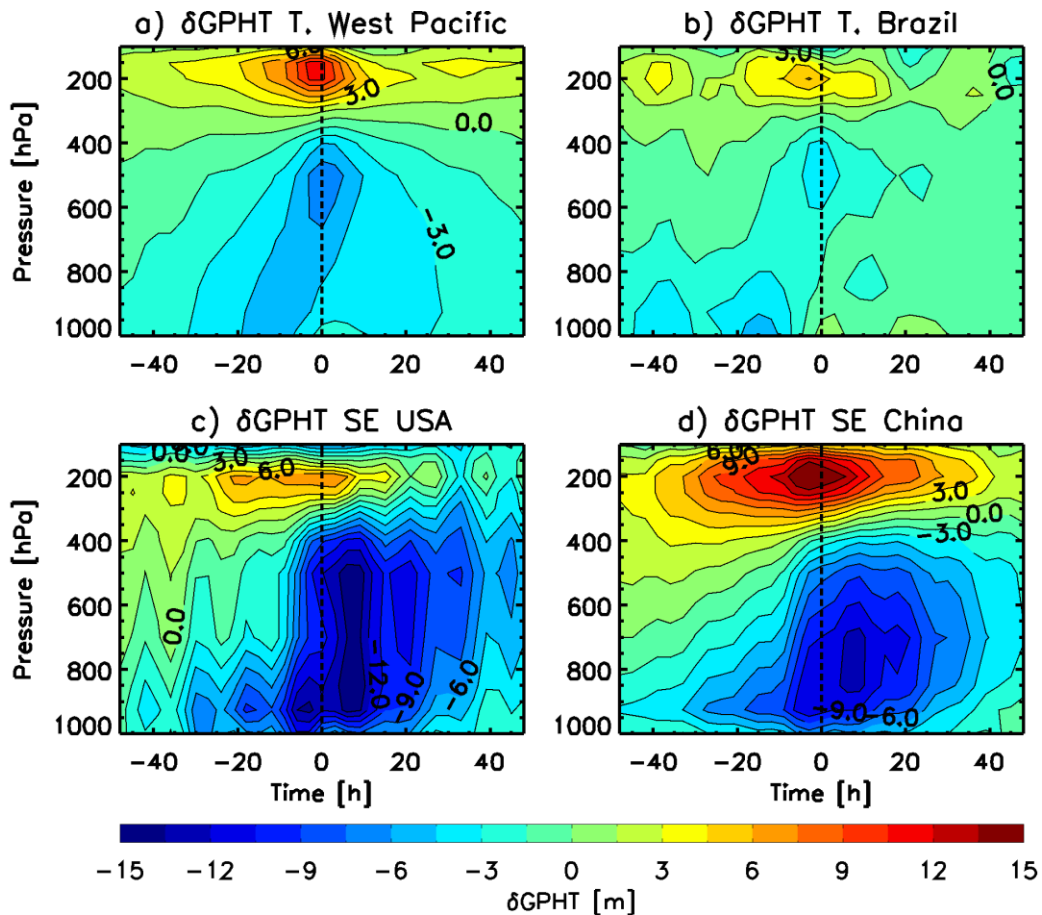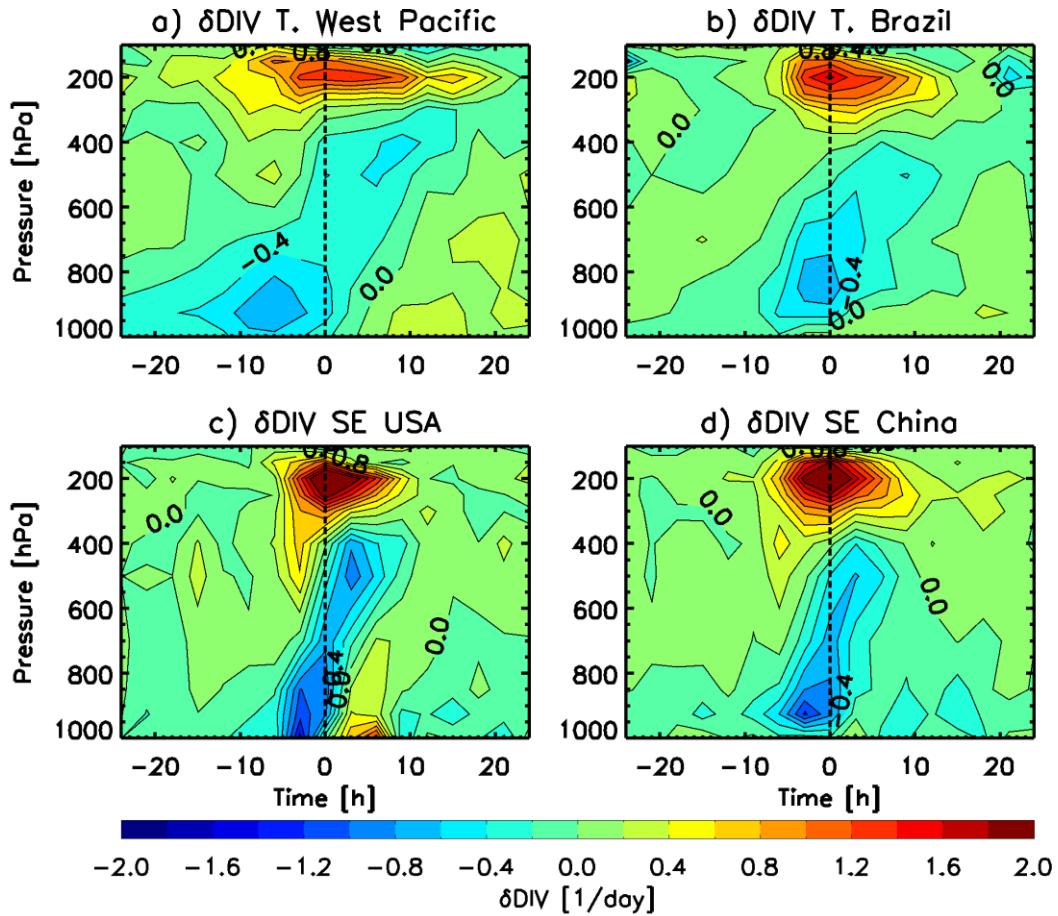
Figure 4.13: The variation in the mass divergence anomaly during high rain events in each region. The horizontal axis refers to time since peak rainfall.

4.6.10 RELATIVE VORTICITY

Relative vorticity was calculated from the horizontal wind measurements of a radiosonde array using the following expression.

$$\zeta = \sum \frac{V_p dl}{A} \tag{4.4}$$

V_p refers to the wind component parallel to a line connecting two points in the array, dl to the distance between the two points, and A to the surface area of the array.

Unfortunately, the relative vorticity anomaly patterns of the two tropical regions were irregular and did not show strong features. This can probably be attributed to the

weakness of the Coriolis parameter at the latitudes characteristic of the radiosonde arrays of these two regions, which would weaken the relative impact of the divergence term on the local vorticity budget. Figure 4.14a and 4.14b shows the relative vorticity anomaly patterns of the two mid-latitude regions. Within the Southeast China and Southeast United States regions, positive relative vorticity anomalies develop in the boundary layer one day prior to peak rainfall. These features are presumably associated with the coincident development of boundary layer convergence. At peak rainfall, the positive vorticity anomalies intensify and grow vertically to 400 hPa. The timing in the growth and vertical extent of these vorticity anomalies is consistent with the mid-level convergence features shown in Figure 4.13. Both regions also show a strong negative (anticyclonic) vorticity anomaly in the upper troposphere [*Cotton et al.*, 1989], as would be expected to develop in response to the strong upper tropospheric outflow features shown in Figure 4.13.

4.6.11 POTENTIAL VORTICITY

The production of Potential Vorticity (PV) within convective systems is believed to have a role in the development of the midlevel jet [*Franklin et al.*, 2006]. PV was calculated from the temperature and horizontal wind profiles of the radiosonde arrays using then following expression.

$$PV = \left(\zeta + f\right)\left(-g\frac{\partial \theta}{\partial p}\right) \tag{4.5}$$

In this equation, ζ refers to relative vorticity, f to the Coriolis parameter, g to standard gravity (9.806 ms^{-2}), θ to potential temperature, and p to pressure.

The PV and PV anomaly patterns about high rain events within the Southeast United States and Southeast China regions are shown in Figure 4.14c, 4.14d, 4.14e, and 4.14f, respectively. The tropopause is indicated by the strong vertical gradient in PV near 200 hPa. In both regions, high rain events are associated with strong negative PV anomalies near the tropopause. The development of this anomaly is consistent with a reduction in convective heating in going from the troposphere to the stratosphere.

Figures 4.14e and 4.14f also show that high rain events within the two regions are associated with positive PV anomalies that extend from the surface to 400 hPa. The stratiform type temperature response shown in Figures 4.5 and 4.8 would be expected to be associated with positive stability and PV anomalies in the mid-troposphere [*Hertenstein and Schubert*, 1991; *May et al.*, 1994; *Franklin et al.,* 2006]. It has been shown that convective rainfall variability within the western half of the Southeast United States region shown in Figure 4.1c is modulated by PV anomalies generated along Rocky Mountains [*Li and Smith*, 2010]. This source of convective variability is likely to have some influence on the overall PV anomaly in this region. Figure 4.14e also shows that high rain events in the Southeast United States are also associated with strong positive PV anomalies near the surface. This increase is consistent with the increase in boundary layer stability that occurs during high rain events.
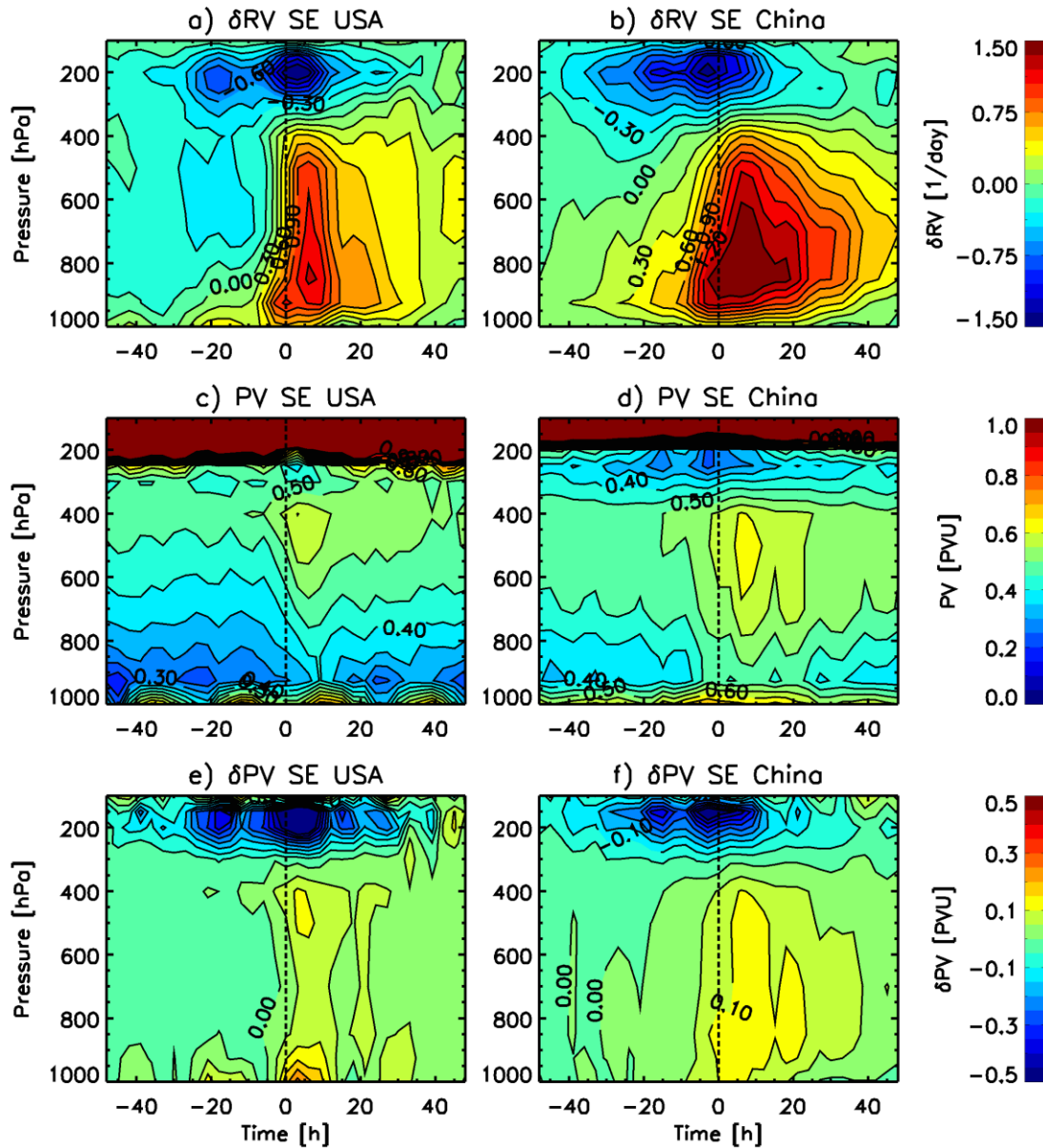
Figure 4.14: Panels (a) and (b) show the variation in the relative vorticity anomaly about high rain events, calculated from radiosonde arrays in the Southeast United States and China. Panels (c) and (d) show the variation in Potential Vorticity (PV) about high rain events. Panels (e) and (f) show the variation in the potential vorticity anomaly about high rain events. The horizontal axis refers to time since peak rainfall. The potential vorticity is expressed in potential vorticity units (PVU), where 1 PVU $= 10^{-6} m^2 s^{-1} K kg^{-1}$.

4.6.12 TENDENCIES

Figure 4.15a shows the relative humidity tendency about high rain events in the Western Tropical Pacific, calculated from the relative humidity anomaly pattern shown in Figure 4.9a. The tendency pattern is dominated by moistening during the growth stage of high rain events at all altitudes, but especially in the upper troposphere. During the decay stage, drying is strongest in the lower troposphere. Figure 4.15b shows the temperature tendency about high rain events in the Western Tropical Pacific, calculated from the temperature anomaly patterns shown in Figure 4.5a. The pattern is dominated by the development of a stratiform temperature response prior to peak rainfall, and the erosion of this response after peak rainfall.

Diagnostic interpretations of the anomaly patterns which occur during the evolution of strong convective events usually attribute the observed patterns to a combination of convective and large scale forcings [*Yanai et al.*, 1973]. The large scale forcings refer, for example, to the temperature and relative humidity tendencies associated with the mean vertical motion within a radiosonde array and to horizontal advection. The convective forcings then refer to the sum of the remaining physical tendencies which can not be attributed to the large scale flow. These include not only the tendencies associated with moist convective circulations internal to the radiosonde array, but also to the tendencies generated by other forms of turbulent mixing as well as radiative heating and cooling. For a convective system, the particular partitioning of the observed (or residual) tendency into large scale and convective components will depend on the size of the radiosonde array used to diagnose the mean vertical velocity within the array.
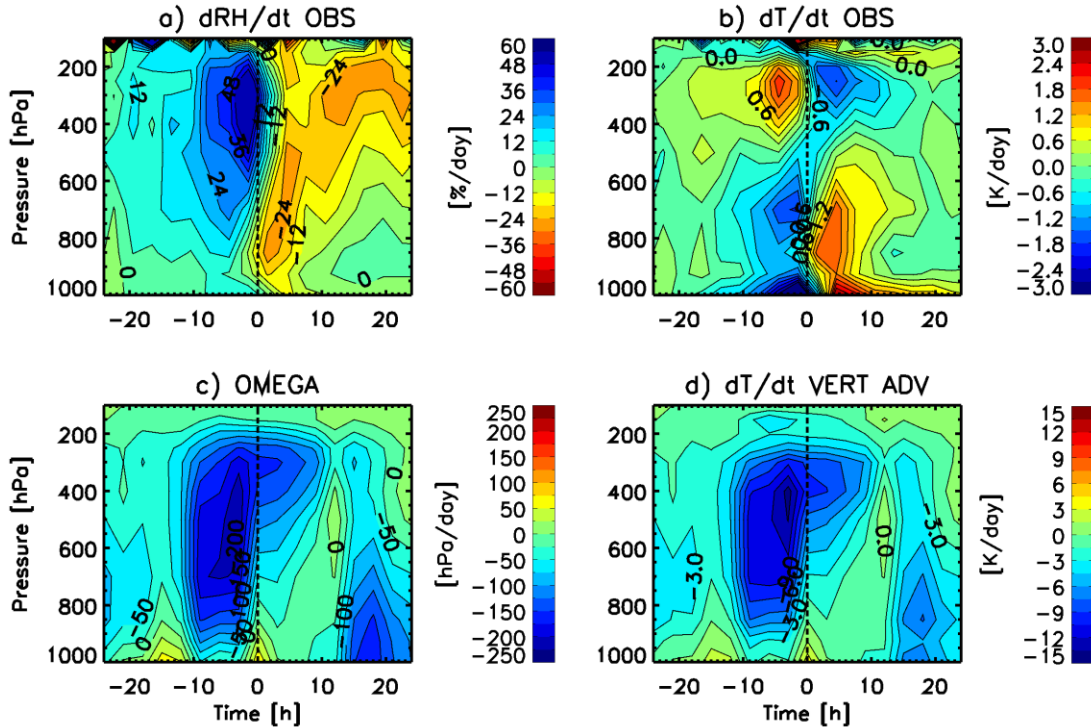
Figure 4.15: (a) The relative humidity tendency pattern (dRH/dt) calculated from the Western Tropical Pacific relative humidity pattern shown in Figure 4.9a. (b) The observed temperature tendency pattern (dT/dt), calculated from the Western Tropical Pacific temperature anomaly patterns shown in Figure 4.5a. (c) The vertical pressure velocity calculated from the Western Pacific divergence anomaly pattern shown in Figure 4.13a. (d) The temperature tendency pattern due to vertical advection, calculated from the vertical pressure velocity and stability anomaly patterns.

Figure 15c shows the evolution of the domain averaged vertical motion (pressure velocity) within the two Western Tropical Pacific radiosonde arrays shown in Figure 4.1. It was calculated from the divergence anomaly pattern shown in Figure 4.13a, the climatological divergence profile of each array, and by imposing the boundary condition $\omega = 0$ at the 100 hPa pressure level. During the growth stage of high rain events, there is strong upward motion throughout the troposphere, with somewhat larger ascent in the lower troposphere. After peak rainfall, the vertical motion is mainly confined to the upper troposphere [*Mapes et al.*, 2006]. Figure 4.15d shows the temperature tendency pattern

associated with the vertical motion pattern shown in Figure 4.15c, calculated by multiplying the calculated pressure velocity by the appropriate static stability. The heating rate from the large scale vertical motion appears to account for some features of the observed temperature tendencies. In particular, the lower tropospheric warming after peak rainfall appears to be partially due to the weakness of the lower tropospheric dynamical cooling during the decay stage of high rain events.

4.7 DISCUSSION IN TERMS OF TWO MODE DYNAMICAL RESPONSE

Most of the rainfall variability in the Tropical West Pacific is associated with clusters of enhanced convective activity propagating parallel to the equator and which have horizontal flows similar to those exhibited by equatorially trapped shallow water waves [*Kiladis et al.*, 2009]. One of the more common wave types has a period of roughly 2 days, usually propagates westward with a speed of 10 – 30 m/s, and is referred to as the 2-day wave [*Takayabu*, 1994]. The temperature, divergence, and specific humidity anomaly patterns generated by these waves [*Kiladis et al.*, 2009] are similar to the anomaly patterns obtained here by averaging over all tropical high rain events. The anomaly patterns of the 2-day waves can be reproduced by a simple model in which the dynamical response to convective heating is dominated by two vertical modes [*Haertel and Kiladis*, 2004]. The first vertical mode is associated with upward or downward vertical motion, which extends throughout the troposphere, peaks at mid-levels, and can be mainly thought of as the dynamical response to full depth convective heating. The upward motion (dynamical response), represented with vertical arrow at the center of the circulation in Figure 4.16(a), is a response to the deep convective heating Q (eq. 1.4),

115

which is prescribed in the HK04 model. The dynamical response is a large-scale vertical motion, while convective motions are small-scale vertical motions. Convective motions are internal to the array used to calculate the observed divergence patterns and hence can not be detected. The dynamical heating from this mode is roughly equal to the full depth convective heating, but almost exactly out of phase. As illustrated in Figure 4.16a, the full depth heating generated by deep convection is therefore almost exactly cancelled locally by the adiabatic cooling generated by the upward motion of the first mode. As a result, the induced subsidence heating and drying from deep convection is effectively exported to larger spatial scales.
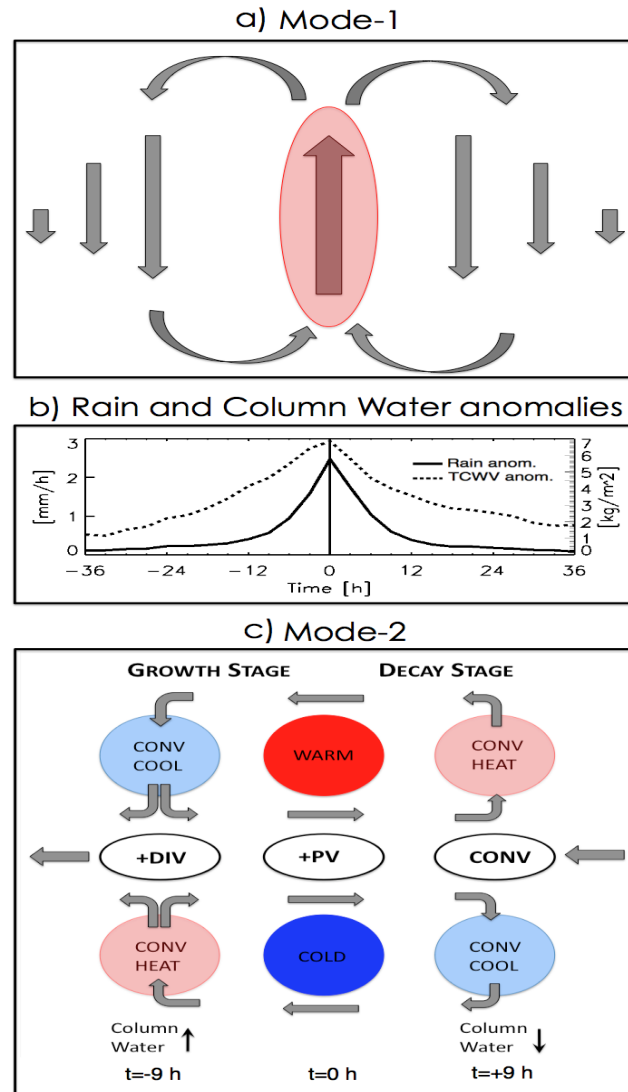
Figure 4.16: (a) The top panel shows the convective heating and large scale circulation associated with mode 1. The convective heating is indicated with the red oval, and the large-scale dynamical motions by the arrows. (b) Rainfall and column water anomalies about high rain events in Western Tropical Pacific region. (c) The convective heating and large scale circulations associated with mode 2. Dark blue and red ovals show observed cold and warm temperature anomalies. This figure has been adapted and modified from Figure 10 of Haertel and Kiladis [2004].

The convective heating and induced vertical motion patterns associated the second vertical mode [*Haertel and Kiladis*, 2004] are illustrated in Figure 4.16c. During the growth stage of high rain events, there is convective warming in the lower troposphere

(e.g. from cumulus congestus clouds), and convective cooling in the upper troposphere. The convective cooling is presumably associated with evaporation of the condensate detrained from deep convection. Convective warming and convective cooling are generated within convective clouds. Convective warming will generate positive geopotential height anomalies above the warming. This will generate pressure gradient accelerations out of the convective region, which by mass conservation will result in upward motion under the positive geopotential height anomalies. This upward vertical motion, will generate dynamical cooling.

The large scale upward motion in the lower troposphere and downward motion in the upper troposphere of mode 2 give rise to the observed mid-level divergence that occurs prior to peak rainfall, shown in Figure 4.13a. As with the first vertical mode, the heating tendencies associated with convection and the dynamical response oppose one another. However, because the magnitude of the dynamical heating exceeds the magnitude of the convective heating, the observed temperature tendency during the growth stage of high rain events is in phase with the dynamically induced cooling of the lower troposphere and the dynamical warming of the upper troposphere. After peak rainfall, the convective heating of the second mode is associated with convective cooling in the lower troposphere and convective warming in the upper troposphere (e.g. as would arise from precipitating stratiform anvil clouds). The induced dynamical motion is downward in the lower troposphere and upward in the upper troposphere, as required to generate the observed mid-level convergence. The magnitude of the dynamical heating again exceeds the magnitude of the convective heating, so that the net heating rate from the second mode is positive in the lower troposphere and negative in the upper

118

troposphere, giving rise to the observed residual heating pattern which damps the stratiform temperature anomaly pattern generated during the growth stage of high rain events.

The net upward lower tropospheric motion of the second mode would favour moistening of the lower troposphere during the growth stage. Conversely, the net downward motion of the second mode would favour the drying of the lower troposphere during the decay stage. These effects are consistent with the observed relative humidity tendencies shown in Figure 4.15a. However, for the upper troposphere, it is not possible to interpret the observed relative humidity tendency in terms of the expected residual vertical motion of the second mode. This is particularly true during the growth stage where the upper troposphere warms (suggesting net descent), but the observed moistening is quite strong. This is presumably a reflection of the relatively greater role of detrained condensate in affecting the moisture budget of the upper troposphere.

In the above conceptual model [*Haertel and Kiladis*, 2004], the growth and decay of the dominant stratiform temperature response is attributed to an imbalance between the convective and dynamical heating of the second mode. It is not clear why the dynamical heating tendency of the second mode should be larger than that of the convective heating tendency. However, presumably, there is a self selection procedure whereby the size, propagation speed, and heating patterns of observed convective systems are self selected in ways that are favorable to their continued existence. This would include the rapid removal of the deep convective heating signature via the mode 1 dynamical response, so that the rainfall system continues to have sufficient CAPE, and the mid-level divergence

during the growth stage, which would increase the column moist static energy [*Haertel at al.*, 2008].

The mid-level divergence and associated upward lower tropospheric motion prior to peak rainfall would also promote the development of positive column water vapor anomalies during the growth stage of high rain events. Column water affects the growth of convective instabilities by modifying the effect of entrainment on updraft buoyancy [*Sherwood*, 1999; *Sherwood and Wahrlich*, 1999; *Raymond*, 2000]. For rain events in the Western Tropical Pacific, Figure 4.10 shows that column water starts to increase up to 48 hours prior to peak rainfall. This is much earlier than the onset of increases in rainfall (about 12 hours prior to peak rainfall), and suggests that the induced lower tropospheric uplift from the second mode may extend a considerable distance in front of a rain event. The radial temperature anomalies shown in Figure 4.8 support this viewpoint by showing that the lower tropospheric cold anomalies extend roughly 600 km outward from high rain events, again much larger than the size of the rain event itself. A slow synoptic scale rise in column water starting roughly 36 hours prior to peak rainfall also occurring prior to rainfall increases has been previously observed in other datasets [*Holloway and Neelin*, 2010].

The development of the stratiform temperature response during the growth stage of high rain events contributes to increases in mid-level stability and PV. During the decay stage, the net downward motion in the lower troposphere from the convective and large scale circulations (which contribute to the observed decrease in lower tropospheric relative humidity) would also be expected to transport the enhanced mid-level PV toward the surface. Although we could not calculate PV anomaly patterns of the two tropical

regions, the PV patterns shown in Figure 4.14 for the Southeast United States and Southeast China regions give support for the existence of a tongue of higher PV air extending downward toward the surface from the 400 hPa level after peak rainfall. The downward advection of the mid-level PV maximum after peak rainfall may play a role in hurricane genesis. In the "top down" theory of hurricane genesis [*Gjorgjievska and Raymond*, 2013], a mid-level positive PV anomaly generated by the stratiform heating profile of a mesoscale convective system is advected toward the surface by evaporative cooling, where it then initiates the formation of a warm core anticyclone [*Bister and Emanuel*, 1997].

4.8 SUMMARY

We have used the TRMM 3B42 gridded rainfall dataset to identify 2x2-degree rain events in four regions: the Western Tropical Pacific, Tropical Brazil, Southeast China, and Southeast United States. Within each region, we selected rain events in close proximity to radiosonde or surface weather stations. These measurements were then used to construct composite anomaly patterns of a large number of meteorological variables about high rain events. One motivation of this analysis was to determine the regional similarities and differences in the interaction between strong convective events and the background atmosphere. The second motivation was to help determine the pathways by which the atmosphere returns to a balanced state following moist convection, and to help understand how these pathways affect the evolution of convective systems.

Our analysis shows that there are many similarities in the interaction between strong convective events and the background atmosphere between the four different

regions. With the partial exception of Southeast China (which appears to lack the 700 hPa cooling maximum), deep convection occurs in association with the development of a stratiform type temperature response in the background atmosphere. In all four regions, the upper tropospheric warming extends roughly 1000 km outward from deep convective events, while the lower tropospheric cooling extends roughly 600 km. The upper tropospheric warming and lower tropospheric cooling generate increased stability at mid-levels. The mid-level stability increase can be expected to enhance convective detrainment in the mid-troposphere and promote the development of cumulus congestus clouds. High rain events in each of the four regions are associated with strong boundary layer cooling during the decay stage. This boundary layer cooling was stronger in the three land regions than in the Western Tropical Pacific.

In two of the four regions, we were able to calculate the time evolution of the vertical structure of CAPE in the boundary layer during high rain events. In agreement with previous studies [*Sherwood and Wahrlich*, 1999] the boundary layer cooling after peak rainfall contributes to the development of strongly negative CAPE anomalies throughout the boundary layer in both regions. Within the Southeast United States region, the CAPE enhancement prior to peak rainfall was roughly 200 J/kg. The near surface layer of positive CAPE was much deeper over land than the ocean. Within the Southeast United States region, the positive CAPE layer extended to roughly 800 hPa, whereas within the Western Tropical Pacific region it extended to only 900 hPa.

There were regional variations in the interaction between strong convective events and the background atmosphere. In the two mid-latitude regions, the mid and lower tropospheric negative geopotential height anomalies that developed during and after high

rain events were much stronger, more vertically coherent, and more persistent than in the two tropical regions. These more strongly negative geopotential height anomalies can be partly attributed to the more strongly negative surface pressure anomalies that develop during mid-latitude convection. An additional difference is that each of the three land regions exhibited warming in the lower troposphere prior to peak rainfall, a feature absent from the tropical ocean region. Finally, the mid-level stratiform convergence of the two mid-latitude regions occurred closer in time to peak rainfall than in the two tropical regions.

Within the Southeast United States region, rain events which occur during the evening are associated with larger reductions in surface pressure than those which occur during the day. It is not clear whether the larger surface pressure reductions at night were driven by a diurnal change in the nature of deep convection, or whether the larger surface pressure reduction at night is associated with more strongly forced synoptic environments for convective events. However, if convection does indeed force the larger nighttime surface pressure reductions, diurnal changes in behavior of deep convection may contribute to the observed diurnal cycle of surface pressure in this region.

Convective circulations modify the temperature, relative humidity, and surface pressure of the background atmosphere, and contribute to the generation of geopotential height anomalies. These geopotential height anomalies, in concert with any pre-existing dynamical forcings, contribute to the large-scale circulations which occur in association with convective events. The observed anomaly patterns therefore result from both the direct effects of convection and the large-scale flow. We have suggested that a two mode dynamical model originally developed to explain the anomaly patterns of the 2-day wave

[*Haertel and Kiladis*, 2004], and later used to interpret anomalies associated with the Madden-Julian oscillation [*Haertel et al.*, 2008], is an appropriate conceptual model for interpreting the mean anomaly patterns of high rain events over the tropical oceans. In this model, the negative mid-level geopotential height anomalies that develop during the growth stage of convective events help drive a convergent mid-level inflow toward high rain events during the decay stage that requires, by mass balance, compensatory lower tropospheric uplift in the background atmosphere. This uplift appears to be responsible for the development of positive column water vapor anomalies which develop up to 48 hours prior to peak rainfall, and roughly 36 hours prior to the onset of increases in rain rate.

We were able to calculate the vorticity and potential vorticity anomaly patterns of high rain events in the Southeast China the Southeast United States regions. In both of these regions, high rain events are associated with negative anomalies in both upper tropospheric relative and potential vorticity which extend into the lower stratosphere. Below 400 hPa, convective events are associated with positive anomalies in relative vorticity and potential vorticity. During the decay stage of high rain events, the mid-level positive PV anomaly appears to be transported toward the surface by the net downward circulation.

CHAPTER 5. CONCLUSION

5.1 SUMMARY OF THE PRESENT WORK

In Project 1 (Chapter 2), we used the TRMM 2x2-degree gridded rainfall to isolate high rainfall events in the Western Tropical Pacific. We then used radiosonde measurements from 10 stations located in the Western Tropical Pacific to construct composite anomaly patterns of temperature, relative humidity, and divergence about the high rain events. One purpose of this project was to show the interaction between convection and the background atmosphere on short timescales expressed with composite anomaly patterns.

A boundary layer convergence and midlevel divergence start to develop 10 hours prior to peak rainfall. We attributed the midlevel divergence prior to peak rainfall to congestus outflow. An upper level divergence develops during peak rainfall. We attributed this feature to deep convective outflow. A midlevel convergence and a boundary layer divergence develop after peak rainfall. We attributed these features to stratiform anvil clouds. The congestus divergence and the stratiform convergence features occur at ~500 hPa, are of similar magnitude (0.5/day), and are symmetrically distributed about peak rainfall.

The observed relative humidity shows a maximum in the lower troposphere (900 to 700 hPa) prior to peak rainfall. A layer of positive relative humidity anomalies throughout the troposphere, with exception of the boundary layer, develops during peak rainfall. After peak rainfall, relative humidity peaks in the middle and upper troposphere.

An upper level warming of approximately 1 K, centered at 300 hPa, is nearly

symmetric about peak rainfall. A midlevel cooling of about 1 K, centered at 700 hPa, and a boundary layer cooling of about 2 K are preferentially distributed after peak rainfall. We also showed that the magnitudes of the temperature and relative humidity anomalies are sensitive to changes in rainfall event definition; stronger events generate stronger anomalies. The shape of the temperature and relative humidity anomaly patterns, however, is nearly insensitive to changes in rainfall event definition.

Another purpose of this project was to compare the observed composite anomaly patterns to the composite anomaly patterns derived using general circulation model and reanalysis outputs. Therefore, we compared observed composite anomaly patterns to those generated by high rain events in four climate models (AGCM3 and AGCM4, GFDL CM2.1, and ECHAM5) and two reanalyses products (ERA-40 and ERA-Interim). In all four models and reanalyses, the rainfall events are less intense and less temporally confined than in TRMM 3B42. Consequently, in all four models, the upper-level warming, moistening, and divergence features are less temporally confined. Only ECHAM5 and ERA-Interim exhibit a mid-level convergence-divergence dipole. In these models, however, the altitude, timing, and amplitude of the midlevel divergence-convergence dipole are not fully consistent with observations. ERA-40 and ERA-Interim underestimate the boundary layer cooling that develops in response to high rainfall. Three of the models show boundary layer warming in association with high rain events. These discrepancies suggest that the mesoscale downward transport of mid-level air with low moist static energy into the boundary layer in models and reanalyses may be too weak. The observationally based composite anomaly patterns should provide useful diagnostics for testing the accuracy of parameterized convection.

In Project 2 (Chapter 3), we used the TRMM 2x2-degree rainfall to isolate high rain events in the Tropical Pacific. We then used horizontal wind measurements from radiosonde arrays, ozonesonde measurements from SHADOZ, and measurements of cloud top heights from CALIPSO to construct anomaly patterns of divergence, ozone mixing ratio, and cloud top height frequency about the high rain events. Previous studies have used measurements of mass divergence, relative humidity, and cloud top height to show the existence of congestus outflow layer. The purpose of this project was to use measurements of chemical tracer (ozone) to show the existence of the congestus outflow layer.

A mid-level divergence and a mid-level positive cloud top frequency anomaly develop prior to peak rainfall. We attributed these features to congestus outflow. A strong positive cloud top frequency anomaly develops in the upper troposphere and is roughly coincident with an upper level divergence. We attributed these features to deep convective outflow. A positive cloud top frequency anomaly develops in the middle and upper troposphere after peak rainfall. This anomaly is coincident with a mid-level convergence and an upper level divergence. The cloud top and divergence anomalies after peak rainfall correspond to a period when an increased occurrence of stratiform anvil clouds is expected.

We showed that, negative ozone anomalies develop at midlevels prior to peak rainfall. Because the midlevel ozone anomalies are coincident with enhancements in the frequency of midlevel cloud tops and midlevel divergence, we attributed the midlevel ozone anomalies to congestus outflow.

We compared observed ozone anomaly patterns to those generated by high rain

128

events in GEOS-Chem chemical transport model, when forced by GEOS-4 and GEOS-5 assimilated meteorology. Both simulations show two layers of negative ozone anomalies. These layers are centered at 6 km and 16 km. The ozone anomalies in GEOS-Chem, when forced by GEOS-5, are comparable to the observed anomalies, whereas the ozone anomalies in GEOS-Chem, when forced by GEOS-4, are about 3 times smaller than the observed anomalies. Unlike the observed midlevel ozone anomalies, which are strongest prior to peak rainfall, the midlevel ozone anomalies in both simulations are nearly symmetric about peak rainfall. The simulated ozone anomalies are also much more persistent than observations. The excessive persistence of the ozone anomalies can be attributed to excessive persistence of GEOS-4 and GEOS-5 rain events.

Most of the observationally based analyses of the interaction between convection and the background atmosphere have been based on measurements over the tropical oceans. The purpose of the third project (Chapter 4) was, therefore, to identify the regional differences and similarities in the interaction between convection and the background atmosphere on short-time scales.

We used the TRMM 3B42 dataset to identify strong rain events in four regions: the Western Tropical Pacific, Tropical Brazil, the Southeast United States, and Southeast China. We then used 12-hour data from 53 radiosondes and 1-hour data from 53 surface weather stations to construct composite anomaly patterns of meteorological variables about high rain events in four regions. In addition to temperature, relative humidity, and divergence anomaly patterns about high rain events, we also constructed anomalies in surface pressure, total column water vapor, geopotential height, CAPE, and relative and potential vorticity about high rain events.

High rain events in all four regions are associated with an upper-level warming centered at 300 hPa, low-level cooling centered at 700 hPa, and strong boundary layer cooling. The cooling centered at 700 hPa, is less pronounced over China. The boundary layer cooling is stronger and more persistent over the land regions. Over the three land regions, a warm low-level anomaly develops prior to peak rainfall. In all regions, the boundary layer cooling extends about 300 km and the upper level warming extends 1000 km outward from the rain events.

In the Western Tropical Pacific and Southeast United States regions, CAPE maximizes prior to peak rainfall and minimized several hours after peak rainfall. The maximum CAPE anomaly in the Southeast United States is about 10 times larger than the maximum CAPE anomaly in the Western Tropical Pacific. The near surface layer of positive CAPE extends to 800 hPa in the Southeast United States region and only extends to 900 hPa in the Western Tropical Pacific.

In all regions, negative low-level geopotential height anomalies start to develop prior to peak rainfall and can be mainly attributed to reduction in surface pressure. All regions show positive upper level geopotential height anomalies at times of peak rainfall, which can be mainly attributed to positive upper level temperature anomalies. In the tropical regions, negative mid-level geopotential height anomalies are largest at t=0, while in the midlatitude regions, the negative anomalies are largest after peak rainfall. The negative mid-level geopotential height anomalies are much stronger and much deeper in the mid-latitude regions and can be attributed to larger negative surface pressure and larger negative temperature anomalies in the lower troposphere.

With exception of Tropical Brazil, all regions show a strong boundary layer

convergence prior to peak rainfall. All regions show a strong upper level divergence near peak rainfall and mid-level convergence after peak rainfall. In the three land regions, the mid-level divergence-convergence dipole tends to occur closer to peak rainfall than in the Western Tropical Pacific. Within the Southeast United States and Southeast China, the boundary layer convergence is associated with a cyclonic boundary layer relative vorticity anomaly, while the upper level divergence is associated with an anticyclonic upper level relative and PV anomalies. We showed that a positive PV anomaly is generated in the middle troposphere during peak rainfall. After peak rainfall, the PV anomaly is advected towards the surface by the net downward transport. The downward transport of PV may play a role in hurricane genesis.

The relative humidity tendency anomaly about high rain events in the Western Tropical Pacific shows strong moistening of the middle and upper troposphere prior to peak rainfall and drying of the lower troposphere after peak rainfall. The temperature tendencies show cooling of the lower troposphere and warming of the upper troposphere prior to peak rainfall and warming of the lower troposphere and cooling of the upper troposphere after peak rainfall.

In Chapters 2, 3, and 4, we follow similar methodology to construct composite anomaly patterns in the 2-4 day period encompassing a heavy precipitation event. The results were then interpreted using two conceptual models of convective systems. In Chapter 2 and Chapter 3, we interpret the observations in light of the building block model. In Chapter 4, we interpret the observations using a simple dynamical model of Haertel and Kiladis

In the building block model, congestus clouds precede deep convective clouds,

which are then followed by stratiform anvil clouds. Congestus clouds premoisten the lower troposphere, and thus increase the likelihood for deep convection to be triggered. In the first two projects we show that, a boundary layer convergence is coincident with a midlevel divergence, midlevel RH maximum, and negative ozone anomalies in the lower troposphere. Because these features occur before peak rainfall, we suggested that they might arise from cumulus congestus outflow. We associated the upper-level divergence, centered at peak rainfall, with deep convective outflow. In the first two projects we also show that the convergence maximum at 500 hPa, which occurs after peak rainfall, to be probably due to an increase in downdraft mass flux below the melting level and increase in upward mass flux above the melting level within stratiform anvils. The cooling of the lower troposphere after peak rainfall is consequence of these downdrafts.

In the building block model, the durations of zones of congestus, deep, and stratiform clouds in MCSs are modulated by large-scale waves [Mapes 2006]. The building block model is useful conceptual model of mesoscale convective systems. The building block model, however, does not, by itself, quantitatively explain for the observed stratiform temperature response or boundary layer cooling that occur in association with high rain events.

We used the dynamical model of Haertel and Kiladis (HK04) to interpret the results in Chapter 4. In this model, the observed anomalies are generated by the residual of the tendencies from convective and large-scale forcings. The large-scale forcings represent the mean vertical and horizontal motion within radiosonde arrays. The convective forcings include moist convective circulations (convective heating, compensatory subsidence, and dynamical response to convective heating), radiative

heating and cooling, and turbulent mixing. In the HK04 model, convection may develop locally or may be preexisting and advected over the region of interest. The stratiform temperature response that occurs in association with high rain events is residual of the convective and large-scale forcings.

For rain events of the same size the time interval between some features, for instance the time interval between the mid-level divergence and the mid-level convergence, would be smaller for faster propagating systems. It is difficult to identify a unique speed of a rain event due to multi-scale nature of tropical convection. For example, Kelvin waves moving eastward around 20 m/s are often associated with smaller westward propagating waves that form at the leading edge and propagate backward against the motion of the parent Kelvin wave. The speed then will depend on the size of the rain event we choose. The observed anomalies here show the average over systems with different propagating speed including local developing systems. The observed temperature and divergence anomalies (in the thesis) averaged over systems with different propagating speed are similar with the temperature and divergence anomalies generated by the HK04 model, in which the wave velocity propagated westward with 16 m/s. The HK04 model can therefore be used to explain the mean temperature and divergence perturbations generated by systems with different propagating speed including local developing systems.

5.2 FUTURE DIRECTIONS

The easterly winds are the dominant surface winds in the equatorial Pacific. These winds, sometimes called trade winds, drive the warm surface water westward, which

results in warmer water over the Western Pacific and cooler water over the Eastern Pacific. There are situations when the trade winds can be suppressed or even reversed. Situation when the zonal equatorial wind anomaly, with respect to the climatological zonal mean, is greater than 5 ms^{-1}, lasts for at least 2 days, and extends over at least 500 km, is known as the westerly wind burst [WWB, *Gebbie and Tziperman*, 2009].

Westerly wind bursts drive the warm surface water eastward, generating eastward propagating Kelvin waves [*Harrison and Schopf*, 1984]. The eastward propagating Kelvin waves, as well as the suppressed trades over the west coast of South America, have a direct impact on the depth of the warm water in the Eastern Pacific [*Vecchi and Harrison*, 2000]. This plays an important role in initiation of the El Nino Southern Oscillation (ENSO) [*Latif* et al., 1988; *Lengaigne et al.*, 2004], which may result in decrease in western Pacific cyclonic activity [*Vecchi and Wittenberg*, 2010]. The WWBs are not realistically represented in most global climate models, which could have an implication in the ability of model to predict an ENSO [*Gebbie and Tziperman*, 2009].

On short timescales, less than a few days, the cause of the WWB and its interaction with convection is unknown [*Chen et al.*, 1996]. A study suggests that negatively buoyant downdraft air could be a mass source of the WWB [*Houze et al.*, 2000]. Therefore, it will be important to extend our study further and look for a possible relationship between WWB (zonal wind anomalies) and its interaction with high rainfall events in the Western Tropical Pacific. As we did in the thesis, we will first isolate high rain events. We will then classify these events as moving or stationary according to their horizontal displacement. The moving events will be further separated into eastward and westward propagating events. Once the rain events are separated into groups, we will construct

surface (or boundary layer) wind anomalies to determine the possibility of occurrence of WWB with each rain event group. The purpose of this analysis would be to determine the cause of the WWB and its link with convection, i.e. its link with the eastward or westward propagating events.

REFERENCES

Anthes, R. A., and Coauthors (2008): The COSMIC/FORMOSAT-3 Mission: early results. *Bull. Amer. Meteor. Soc.*, 89, 313–333.

Arakawa, A., W. H. Schubert (1974): Interaction of a cumulus cloud ensemble with the large-scale environment, Part I. *J. Atmos. Sci.*, 31, 674–701.

Arakawa, A. (2004): The cumulus parameterization problem: past, present, and future. *J. Climate*, 17, 2493–2525.

Armitage P, Berry G, Matthews JNS (2002): *Statistical Methods in Medical Research* (4th edition). Oxford: Blackwell Science.

Avery, M., et al. (2010): Convective distribution of tropospheric ozone and tracers in the Central American ITCZ region: Evidence from observations during TC4, *J. Geophys. Res.,* 115, (D00J21).

Barnes, G. M., and M. Garstang, (1982): Subcloud layer energetics of precipitating convection. *Mon. Wea. Rev.,* 103, 102-117.

Benedict, J., and D. A. Randall (2007): Observed characteristics of the MJO relative to maximum rainfall. *J. Atmos. Sci.*, 64, 2332-2354.

Bey, I., et al. (2001): Global modeling of tropospheric chemistry with assimilated meteorology: Model description and evaluation*, J. Geophys. Res.,* 106*,* 23,073–23,096.

Bister, M., and K. A. Emanuel (1997): The genesis of hurricane Guillermo: TEXMEX analyses and a modeling study. *Mon. Wea. Rev.*, 125, 2662-2682.

Chen, S. S., R. A. Houze Jr., and B. E. Mapes (1996): Multiscale variability of deep convection in relation to large-scale circulation in TOGA COARE, *J. Atmos. Sci.*, 53, 1380–1409.

Christian, H. J., et al. (2003): Global frequency and distribution of lightning as observed from space by the Optical Transient Detector, *J. Geophys. Res.,* 108(D1), 4005.

Cotton, W. R., M-S. Lin, R. L. McAnelly, and C. J. Tremback (1989): A composite model of mesoscale convective complexes. *Mon. Wea. Rev.*, 117, 765–783.

Dai, A., F. Giorgi, and K. E. Trenberth (1999): Observed and model-simulated diurnal cycles of precipitation over the contiguous United States. *J. Geophys. Res.,* 104, 6377-6402.

Dai, A., (2006): Precipitation characteristics in eighteen coupled climate models. *J. Climate,* 19, 4605–4630.

Delworth, T., et al., (2006): GFDL's CM2 global coupled climate models. Part I: Formulation and simulation characteristics. *J. Climate,* 19, 643-674.

DeMott, C., D. A. Randall, and M. Khairoutdinov (2007): Convective precipitation variability as a tool for general circulation model analysis. *J. Climate,* 20, 91-112.

Dessler, A. E., S. P. Palm, and J. D. Spinhirne (2006): Tropical cloud-top height distributions revealed by the Ice, Cloud, and Land Elevation Satellite (ICESat)/Geoscience Laser Altimeter System (GLAS), *J. Geophys. Res.,* 111, (D12215).

Durre, I., R. S. Vose, and D. B. Wuertz, (2006): Overview of the integrated global radiosonde archive. *J. Climate,* 19, 53-68.

Emanuel, K.A. (1994): *Atmospheric Convection*, Oxford University Press, New York, 580 pp.

Folkins, I., C. Braun, A. M. Thompson, and J. C. Witte (2002): Tropical ozone as an indicator of deep convection, *J. Geophys. Res.,* 107 (D13) 4184.

Folkins, I., and R. V. Martin (2005): The vertical structure of tropical convection and its impact on the budgets of water vapor and ozone, *J. Atmos. Sci.,* 62, 1560-1573.

Folkins, I., et al. (2006): Testing convective parameterizations with tropical measurements of HNO_3, CO, H_2O, and O_3: Implications for the water vapor budget, *J. Geophys. Res.,* 111*,* (D23304).

Folkins, I., et al., (2008): A low-level circulation in the tropics. *J. Atmos. Sci.,* 65, 1019-1034.

Folkins, I., (2009): A one-dimensional cloud model with trimodal convective outflow, *J. Climate*, 22, 6437 - 6455.

Folkins I., T. Mitovski, and J. R. Pierce (2013): A simple way to improve the diurnal cycle in convective rainfall over land in climate models. Submitted to *J. Geophys. Res*.

Fovell, R. G., G. Mullendore, and S. H. Kim, (2006): Discrete propagation in numerically simulated nocturnal squall lines. *Mon. Wea. Rev*., 134, 3735 – 3752.

Frank, W., M., (1978): The life cycles of GATE convective systems. *J. Atmos. Sci*., 35, 1256-1264.

Franklin, C. N., G. J. Holland, and P. T. May (2006): Mechanisms for the generation of mesoscale vorticity features in tropical cyclone rainbands. *Mon. Wea. Rev*., 134, 2649–2669.

Fritsch, J. M., R. J. Kane, C. R. Chelius (1986): The contribution of mesoscale convective weather systems to the warm-season precipitation in the United States. *J. Climate Appl. Meteor*., 25, 1333–1345.

Gebbie, G., and E. Tziperman (2009): Predictability of SST-modulated westerly wind burst. *J. Climate*, 22, 3894-3909.

Gjorgjievska, S. and D. J. Raymond (2013): Interaction between dynamics and thermodynamics during tropical cyclogenesis. *Atmos. Chem. Phys. Discuss.*, 13, 18905-18950.

Hack, J. J., (1994): Parameterization of moist convection in the National Center for Atmospheric Research community climate model (CCM2), J. Geophys. Res., 99, 5551-5568.

Haertel, P. T., and R. H. Johnson, (1998): Two-day disturbances in the equatorial western Pacific. *Quart. J. Roy. Meteor. Soc.*, 124, 615–636.

Haertel, P. T., and G. N. Kiladis (2004): Dynamics of 2-day equatorial waves. *J. Atmos. Sci.*, 61, 2707–2721.

Haertel, P. T., G. N. Kiladis, A. Denno, and T. M. Rickenbach (2008): Vertical-mode decompositions of 2-day waves and the Madden–Julian oscillation. *J. Atmos. Sci.*, 65, 813–833.

Harrison, D. E., and P. S. Schopf (1984): Kelvin-wave-induced anomalous advection and the onset of surface warming in El Niño event. *Mon. Wea. Rev.*, 112, 923–933.

Hertenstein, R. F. A., and W. H. Schubert (1991): Potential vorticity anomalies associated with squall lines. *Mon. Wea. Rev.*, 119, 1663–1672.

Hohenegger, C., and B. Stevens (2013): Preconditioning deep convection with cumulus congestus. *J. Atmos. Sci.*, 70, 448–464.

Holloway, C. E. and J. D. Neelin (2007): The convective cold top and quasi equilibrium. *J. Atmos. Sci.*, 64, 1467–1487.

Holloway, C. E. and J. D. Neelin (2010), Temporal relations of column water vapor and tropical precipitation. *J. Atmos. Sci.*, 67, 1091–1105.

Houry, S., E. Dombrowsky, P. D. Mey, J.-F. Minster (1987): Brunt-Väisälä frequency and Rossby radii in the South Atlantic. J. *Phys. Oceanogr.*, 17, 1619–1626.

Houze, R. A., Jr., (1977): Structure and dynamics of a tropical squall-line system. *Mon. Wea. Rev.*, 105, 1540-1567.

Houze, R. A. Jr., et al. (2000): Convection over the Pacific warm pool in relation to the atmospheric Kelvin-Rossby wave. *J. Atmos. Sci.*, 57, 3058-3089.

Houze, R. A., Jr., (2004): Mesoscale convective systems, *Rev. Geophys.*, 42, RG4003.

Huffman, G.J., et al., (2007): The TRMM multi-satellite precipitation analysis (TMPA): Quasi-global, multi-year, combined-sensor precipitation estimates at fine scales. *J. Hydrometeor.* 8(1), 38-55.

Huntrieser, H., et al. (2009): NO_x production by lightning in Hector: first airborne measurements during SCOUT-O_3/ACTIVE, *Atmos. Chem. Phys.,* 9, 8377-8412.

Jacob, D. J., et al. (1996): Origin of ozone and NO_x in the tropical troposphere: A photochemical analysis of aircraft observations over the south Atlantic basin, *J. Geophys. Res.,* 101, 24,235–24,250.

Johnson, R. H., (1976): The role of convective-scale precipitation downdrafts in cumulus and synoptic-scale interactions. *J. Atmos. Sci.*, 33, 1890 – 1910.

Johnson, R. H. et al., (1996): Tropical inversions near the 0 C level. *J. Atmos. Sci.*, 53, 1838 – 1855.

Johnson, R.H., T. M. Rickenbach, S. A. Rutledge, P. E. Ciesielski, and W. H. Schubert (1999): Trimodal characteristics of tropical convection. *J. Climate*, 12, 2397-2418.

Khairoutdinov, M. F., et al., (2009): Large-eddy simulation of maritime deep tropical convection, *J. Adv. Model. Earth Syst.*, 1, 1-13.

Kiladis, G. N., K. H. Straub, and P. T. Haertel (2005): Zonal and vertical structure of the Madden–Julian oscillation. *J. Atmos. Sci.*, 62, 2790–2809.

Kiladis, G. N., M. C. Wheeler, P. T. Haertel, K. H. Straub, and P. E. Roundy (2009): Convectively coupled equatorial waves. *Rev. Geophys.*, 47, RG2003.

Kley, D., et al. (1996): Observations of near-zero ozone concentrations over the convective Pacific: Effects on air chemistry, *Science,* 274, 230– 233.

Kley, D., J. M. Russell III, and C. Phillips (Eds.) (2000): SPARC Assessment of upper tropospheric and stratospheric water vapor, WMO/TD-143, World Clim. Res. Programme, Geneva.

Kummerow, C., W. Barnes, T. Kozu, J. Shiue, and J. Simpson, (1998): The Tropical Rainfall Measuring Mission (TRMM) sensor package. *J. Atmos. Oceanic Technol.,* 15(3), 809-817.

Latif, M., J. Biercamp, and H. von Storch (1988): The response of a coupled ocean-atmosphere general circulation model to wind bursts. *J. Atmos. Sci*., 45, 964-979.

Lawrence, M. G., P. J. Crutzen, and P. J. Rasch (1999): Analysis of the CEPEX ozone data using a 3D chemistry-meteorology model, *Q. J. R. Meteorol. Soc*., 125, 2987– 3009.

Lawrence, M. G., von Kuhlmann, R., Salzmann, M., and Rasch, P. J. (2003): The balance of effects of deep convective mixing on tropospheric ozone, *Geophys. Res. Lett.,* 30(18), 1940.

Lelieveld, J., and P. J. Crutzen (1994): Role of deep cloud convection in the ozone budget of the troposphere, *Science*, 264, 1759– 1761.

Lengaigne et al., (2004): Triggering of El Nino by westerly wind events in a coupled general circulation model. *Climate Dyn*., 23, 601-620.

Li, Y., and R. B. Smith (2010): The detection and significance of diurnal pressure and potential vorticity anomalies east of the Rockies. *J. Atmos. Sci.*, 67, 2734–2751.

Liu, J., J. A. Logan, D. B. A. Jones, N. J. Livesey, I. A. Megretsakaia, C. Cargouge, and P. Nedelec (2010): Analysis of CO in the tropical troposphere using Aura satellite data and the GEOS-Chem model: insights into transport characteristics of the GEOS meteorological products, *Atmos. Chem. Phys*., 10, 12,207-12,232.

Liu, Z., D. Ostrenga, W. Teng, and S. Kempler (2012): Tropical Rainfall Measuring Mission (TRMM) precipitation data and services for research and applications. *Bull. Amer. Meteor. Soc.,* 93, 1317-1325.

Lin, J.-L., et al., (2006): Tropical intraseasonal variability in 14 IPCC AR4 climate models. Part I: Convective signals. *J. Climate*, 19, 2665–2690.

Lott, N., R. Baldwin, and P. Jones (2001): The FCC integrated surface hourly database: A new resource of global climate date. NOAA National Climatic Data Center Tech. Rep. 2001-01, 42 pp.

Lohmann, U., and E. Roeckner, (1996): Design and performance of a new cloud microphysical scheme developed for the ECHAM general circulation model. *Climate Dyn., 12,* 557-572.

Lucas, C., E. J. Zipser, and M. A. Lemone (1994), Vertical velocity in oceanic convection off tropical Australia. *J. Atmos. Sci.*, 51, 3183–3193.

Maloney, E. D., and D. L. Hartmann, (1998): Frictional moisture convergence in a composite life cycle of the Madden-Julian oscillation. *J. Climate*, 11, 2387-2403.

Mapes, B. E., (1993): Gregarious tropical convection. *J. Atmos. Sci.*, 50, 2026 – 2037.

Mapes, B. E., and R.A. Houze, Jr., (1995): Diabatic divergence profiles in tropical mesoscale convective systems. *J. Atmos. Sci.,* 52, 1807-1828.

Mapes, B. E., and J. Lin, (2005): Doppler radar observations of mesoscale wind divergence in regions of tropical convection. *Mon. Wea. Rev.,*133, 1808-1824.

Mapes, B. E., S. Tulich, J. Lin, and P. Zuidema, (2006): The mesoscale convection life cycle: Building block or prototype for large-scale tropical waves? *Dyn. Atmos. Oceans,* 42, 3-29.

Mapes, B. E., et al., (2009): Virtual field campaigns on deep tropical convection in climate models. *J. Climate*, 22, 244–257.

Masunaga, H. (2012): A satellite study of the atmospheric forcing and response to moist convection over tropical and subtropical oceans. *J. Atmos. Sci.*, 69, 150–167.

Masunaga, H. (2013): A satellite study of tropical moist convection and environmental variability: A moisture and thermal budget analysis. *J. Atmos. Sci.*, 70, 2443–2466.

Matsuno, T., (1966): Quasi-geostrophic motions in the equatorial area. *J. Meteor. Soc. Japan*, 44, 25–42.

May, P. T., G. J. Holland, and W. L. Ecklund (1994): Wind profiler observations of tropical storm Flo at Saipan. *Wea. Forecasting*, 9, 410–426.

May, P. T., C. N. Long, A. Protat (2012): The diurnal cycle of the boundary layer, convection, clouds, and surface radiation in a coastal monsoon environment (Darwin, Australia). *J. Climate*, 25, 5309–5326.

McCaul, E. W., and C. Cohen (2002): The impact on simulated storm structure and intensity of variations in the mixed layer and moist layer depths. *Mon. Wea. Rev.*, 130, 1722–1748.

McFarlane, N. A., et al., (2005): The CCCma third generation atmospheric general circulation model. CCCma Internal Rep., 25 pp.

Mitovski, T., Folkins, I., von Salzen, K., and Sigmond, M. (2010): Temperature, relative humidity, and divergence response to high rainfall events in the Tropics: observations and models, *J. Climate,* 23, 3613 - 3625.

Mitovski, T., I. Folkins, R. V. Martin, and M. Cooper (2012): Testing convective transport on short time scales: Comparisons with mass divergence and ozone anomaly patterns about high rain events, *J. Geophys. Res.*, 117, D02109.

Mitovski, T., and I. Folkins (2014): Anomaly patterns about strong convective events in the tropics and midlatitudes: Observations from radiosondes and surface weather stations, *J. Geophys. Res. Atmos.*, 119.

Mohr, K. I., J. S. Famiglietti, E. J. Zipser (1999): The contribution to tropical rainfall with respect to convective system type, size, and intensity estimated from the 85-GHz ice-scattering signature. *J. Appl. Meteor.*, 38, 596–606.

Moorthi, S. and M. J. Suarez (1992): Relaxed Arakawa-Schubert, A Parameterization of moist convection for general-circulation models. *Mon. Wea. Rev.* 120, 978-1002.

Murakami, M., (1979): Large-scale aspects of deep convective activity over the GATE area. *Mon. Wea. Rev.*, 107, 994-1013.

Nassar, R., J. A. Logan, I. A. Megretskaia, L. T. Murray, L. Zhang, and D. B. A. Jones (2009): Analysis of tropical tropospheric ozone, carbon monoxide, and water vapor during the 2006 El Niño using TES observations and the GEOS-Chem model, *J. Geophys. Res.*, 114, D17304.

Nesbitt, S. W. and E. J. Zipser (2003): The diurnal cycle of rainfall and convective intensity according to three years of TRMM measurements. *J. Climate*, 16, 1456–1475.

Nordeng, T. E., (1994): Extended versions of the convective parameterization scheme at ECMWF and their impact on the mean and transient activity of the model in the tropics. Technical Memorandum 206, ECMWF, Reading, UK.

Pickering, K. E., Thompson, A. M., Tao, W.-K., and Kucsera, T. L. (1993): Upper tropospheric ozone production following mesoscale convection during STEP/EMEX, *J. Geophys. Res.,* 98, 8737–8749.

Pickering, K. E., et al. (2001): Trace gas transport and scavenging in PEM-Tropics B South Pacific Convergence Zone convection, *J. Geophys. Res.,* 106, 32,591–32,602.

Rajeevan M., and Nanjundiah, R. S. 2009: Coupled model simulations of twentieth century climate of the Indian summer monsoon. Current trends in science, *platinum jubilee special volume of the Indian Academy of Sciences*. Indian Academy of Science, Bangalore, pp 537–568.

Randall, D., M. Khairoutdinov, A. Arakawa, and W. Grabowski (2003): Breaking the cloud parameterization deadlock. *Bull. Amer. Meteor. Soc.*, 84, 1547–1564.

Rapp, A. D., C. Kummerow, and L. D. Fowler (2011): Interactions between warm rain clouds and atmospheric preconditioning for deep convection in the tropics. *J. Geophys. Res.*, 16, D23210.

Raymond, D. (2000): Thermodynamic control of tropical rainfall. *Quart. J. Roy. Meteor. Soc.*, 126, 889–898.

Reed, R. J., and E. E. Recker, (1971): Structure and properties of synoptic-scale wave disturbances in the equatorial western Pacific. *J. Atmos. Sci.,* 28, 1117-1133.

Robinson, F. J., S. C. Sherwood, and Y. Li (2008): Resonant response of deep convection to surface hot spots. *J. Atmos. Sci.*, 65, 276–286.

Roeckner, E., et al., (2003): The atmospheric general circulation model ECHAM5. Part 1: Model description, *Rep.* 349, Max-Planck-Inst. für Meteorol., Hamburg, Germany.

Schumacher, C., and R. A. Houze Jr., (2003): Stratiform rain in the tropics as seen by the TRMM Precipitation Radar. *J. Climate*, 16**,** 1739-1756.

Schumacher, C., P. E. Ciesielski, and M. H. Zhang, (2008): Tropical cloud heating profiles: Analysis from KWAJEX. *Mon. Wea. Rev.,* 136, 4289-4300.

Scinocca J.F., and N.A. McFarlane, (2004): The variability of modeled tropical precipitation. *J. Atmos. Sci.,* 61, 1993-2015.

Sherwood, S. C., (1999): Convective precursors and predictability in the tropical western Pacific. *Mon. Wea. Rev.,* 127, 2977-2991.

Sherwood, S. C., and R. Wahrlich, (1999): Observed evolution of tropical deep convective events and their environment. *Mon. Wea. Rev.,* 127, 1777-1795.

Sobel, A. H., S. E. Yuter, C. S. Bretherton, and G. N. Kiladis, (2004): Large-scale meteorology and deep convection during TRMM KWAJEX. *Mon. Wea. Rev.,* 132, 422–444.

145

Solomon, S., et al. (2005): On the distribution and variability of ozone in the tropical upper troposphere: Implications for tropical deep convection and chemical-dynamical coupling, *Geophys. Res. Lett.,* 32, (L23813).

Sun, Y., S. Solomon, A. Dai, and R. Portmann, (2005): How often does it rain? *J. Climate,* 19, 916–934.

Sun, B.*,* A. Reale*,* D. J. Seidel*,* and D. C. Hunt (2010)*,* Comparing radiosonde and COSMIC atmospheric profile data to quantify differences among radiosonde types and the effects of imperfect collocation on comparison statistics*, J. Geophys. Res.,* 115*,* D23104.

Takayabu, Y. N. (1994), Large-scale cloud disturbances associated with equatorial waves. Part II: Westward-propagating inertio-gravity waves. *J. Meteor. Soc. Japan*, 72, 451–465.

Takayabu, Y. N., K.-M. Lau, and C.-H. Sui, (1996): Observation of a quasi 2-day wave during TOGA COARE. *Mon. Wea. Rev.,* 124, 1892-1913.

Tepper, M., (1950): A proposed mechanism of squall lines: The pressure jump line, *J. Met.*, 12, 287-297.

Thompson, R. M., Jr., S. W. Payne, E. E. Recker, and R. J. Reed, (1979): Structure and properties of synoptic-scale wave disturbances in the intertropical convergence zone of the eastern Atlantic. *J. Atmos. Sci.,* 36, 53-72.

Thompson, A.M., et al. (2003): Southern Hemisphere Additional Ozonesondes (SHADOZ) 1998-2000 tropical ozone climatology 1. Comparison with Total Ozone Mapping Spectrometer (TOMS) and ground-based measurements, *J. Geophys. Res., Vol.* 108 (D2) 8238.

Tiedtke*,* M.*,* (1989): A comprehensive mass flux scheme for cumulus parameterization in large-scale models. *Mon. Wea. Rev.,* 117, 1779-1800.

Tompkins, A. M., (2001): Organization of tropical convection in low vertical wind shears: the role of cold pools. *J. Atmos. Sci.*, 58, 1650 – 1672.

Tompkins, A. M., (2002): A prognostic parameterization for the subgrid-scale variability of water vapor and clouds in large-scale models and its use to diagnose cloud cover. *J. Atmos. Sci.,* 59, 1917-1942.

Uppala et al., (2005): The ERA-40 re-analysis. *Quart. J. Roy. Meteor. Soc.,* 131, 2961-3012

Vaughan, G., et al. (2008): SCOUT- O3/ACTIVE High-altitude aircraft measurements around deep tropical convection, *B. Am. Meteorol. Soc.,* 89*,* 647–662.

Vecchi, G. A., and D. E. Harrison (2000): Tropical Pacific sea surface temperature anomalies, El Niño, and equatorial westerly wind events. *J. Climate*, 13, 1814–1830.

Vecchi, G. A. and Wittenberg, A. T. (2010): El Niño and our future climate: where do we stand? *WIREs Clim. Change*, 1: 260–270.

von Salzen, K., N. A. McFarlane, and M. Lazare, (2005): The role of shallow convection in the water and energy cycles of the atmosphere, *Climate Dyn*., 25, 671-688.

Warner, C., et al. (1980): Deep convection on day 261 of GATE. *Mon. Wea. Rev*., 108, 169-194.

Wilcox, E. M., and L. J. Donner, (2007): The frequency of extreme rain events in satellite rain-rate estimates and an atmospheric general circulation model. *J. Climate*, 20, 53–69.

Winker, D. M., M. A. Vaughan, A. Omar, Y. Hu, K. A. Powell, Z. Liu, W. H. Hunt, S. A. Young (2009): Overview of the CALIPSO mission and CALIOP data processing algorithms. *J. Atmos. Oceanic Technol.*, 26, 2310–2323.

Xie, F., Wu, D. L., Ao, C. O., Mannucci, A. J., and Kursinski, E. R. (2012): Advances and limitations of atmospheric boundary layer observations with GPS occultation over southeast Pacific Ocean. *Atmos. Chem. Phys*., 12, 903-918.

Yanai, M., S. Esbensen, and J.-H. Chu (1973): Determination of bulk properties of tropical cloud clusters from large-scale heat and moisture budgets. *J. Atmos. Sci.*, 30, 611–627.

Zelinka, M. D., and D. L. Hartmann (2009): Response of humidity and clouds to tropical deep convection. *J. Climate*, 22, 2389–2404.

Zhang, G.J. and N. A. McFarlane, (1995): Sensitivity of climate simulations to the parameterization of cumulus convection in the CCC-GCM. *Atmos.-Ocean,* 3, 407-446.

Zipser, E. J., (1969): The role of organized unsaturated convective downdrafts in the structure and rapid decay of an equatorial disturbance. *J. Appl. Meteor.*, 8, 799 – 814.

Zipser, E. J., (1977): Mesoscale and convective-scale downdrafts as distinct components of a squall-line structure. *Mon. Wea. Rev.*, 105, 1568 – 1589.

Zipser, E. J., and C. Gautier, (1978): Mesoscale events within a GATE tropical depression. *Mon. Wea. Rev.*, 106, 789-805.

Zuidema, P., (1998): The 600 – 800 mb minimum in tropical cloudiness observed during TOGA COARE. *J. Atmos. Sci.*, 55, 2220 – 2228.

APPENDIX A

A.1 COPYRIGHT INFORMATION

Chapter 2 of this thesis contains an article published in the Journal of Climate. The article:
Mitovski, Toni, Ian Folkins, Knut von Salzen, Michael Sigmond, 2010: Temperature, Relative Humidity, and Divergence Response to High Rainfall Events in the Tropics: Observations and Models. *J. Climate*, **23**, 3613–3625.
doi: http://dx.doi.org/10.1175/2010JCLI3436.1 , (c)American Meteorological Society. Used with permission.

Further information can be found at
http://www2.ametsoc.org/ams/index.cfm/publications/authors/journal-and-bams-authors/author-resources/copyright-information/copyright-policy/.

Chapters 3 of this thesis contain an article published in the Journal of Geophysical Research: Atmosphere. The author retains the copyright for this publication.
http://s100.copyright.com/CustomerAdmin/PLF.jsp?ref=ccc73fb8-264c-4bf3-8dc1-063ab610b9fd.
Further information can be found at http://publications.agu.org/author-resource-center/usage-permissions/#repository.

Chapters 4 of this thesis contain an article published in the Journal of Geophysical Research: Atmosphere. The author retains the copyright for this publication.
http://s100.copyright.com/CustomerAdmin/PLF.jsp?ref=309e74e0-1f6e-42cb-8e7f-b9bb65440f1a.
Further information can be found at http://publications.agu.org/author-resource-center/usage-permissions/#repository.